Damage Detection in Multi-Layered Plates using Ultrasonic Guided Waves

Dissertation
zur Erlangung des Grades
der Doktorin der Ingenieurwissenschaften
der Naturwissenschaftlich-Technischen Fakultät
der Universität des Saarlandes

vorgelegt von
Yevgeniya Lugovtsova
aus Ust-Kamenogorsk, Kasachstan

Saarbrücken
2022

Dekan der Naturwissenschaftlich-Technischen Fakultät: Univ.-Prof. Dr. rer. nat. Jörn Walter

Erstgutachter: Prof. Dr.-Ing. Christian Boller

Zweitgutachter: Prof. Dr. Michel Castaings, Bordeaux Institut National Polytechnique, France

Vorsitzender: Prof. Dr.-Ing. Stefan Seelecke

Promovierter wissenschaftlicher Mitarbeiter: Dr.-Ing. Prateek Sharma

Tag des Kolloquiums: 6. April 2022

Abstract

This thesis investigates ultrasonic guided waves (GW) in multi-layered plates with the focus on higher order modes. The aim is to develop techniques for hybrid structures such as of adhesive bonds and composite pressure vessels (COPV) which are widely used in automotive and aerospace industries and are still challenging to inspect non-destructively. To be able to analyse GW, numerical methods and precise material properties are required. For this purpose, an efficient semi-analytical approach, the Scaled Boundary Finite Element Method, is used. The material properties are inferred by a GW-based optimisation procedure and a sensitivity study is performed to demonstrate the influence of properties on GW. Then, an interesting feature, called mode repulsion, is investigated with respect to weak and strong adhesive bonds. The results show that the coupling between two layers influences the distance between coupled modes in a mode repulsion region, thus allowing for the characterisation of adhesive bonds. At next, wave-damage interaction is studied in the hybrid structure as of the COPV. Results show that the wave energy can be concentrated in a certain layer enabling damage localisation within different layers. Further investigations are carried out on the hybrid plate with an impact-induced damage. Two well-known wavenumber mapping techniques, which allow to quantify the damage in three dimensions, are implemented and their comparison is done for the first time.

Zusammenfassung

In dieser Arbeit werden geführte Ultraschallwellen (GUW) in mehrschichtigen Platten untersucht, wobei der Schwerpunkt auf Moden höherer Ordnung liegt. Ziel ist die Entwicklung von zerstörungsfreien Prüfmethoden für hybride Strukturen wie Klebeverbindungen und Komposit-Druckbehälter, die in Automobil-, Luft- und Raumfahrtindustrie weit verbreitet sind und deren Prüfung immer noch eine Herausforderung darstellt. Für die GUW-Analyse werden numerische Methoden und präzise Materialeigenschaften benötigt. Hier wird die Scaled Boundary Finite Element Methode verwendet und die Materialeigenschaften werden durch ein GUW-basiertes Optimierungsverfahren hergeleitet. Um den Einfluss der Eigenschaften auf GUW zu analysieren wird eine Sensitivitätsstudie durchgeführt. Anschließend wird vermiedene Kreuzung in Bezug auf schwache und starke Klebeverbindungen untersucht. Die Ergebnisse zeigen, dass die Kopplungsstärke den Abstand zwischen gekoppelten Moden in einer vermiedenen Kreuzung beeinflusst und somit eine Charakterisierung von Klebeverbindungen ermöglicht. Als Nächstes wird die Wechselwirkung zwischen GUW und Schaden in einer Hybridstruktur wie beim Komposit-Druckbehälter untersucht. Die Ergebnisse zeigen, dass die Wellenenergie in einer bestimmten Schicht konzentriert werden kann. Damit wird die Schadenslokalisierung in dieser Schicht ermöglicht. Weiter wird die Quantifizierung der Impakt-Schäden in der Hybridplatte angestrebt, die durch Erstellung einer Wellenzahlkarte erfolgt.

Acknowledgement

This work was carried out during my employment in the Division of Acoustic and Electromagnetic Methods at the Federal Institute for Materials Research and Testing (BAM) in Berlin in cooperation with the Chair of Non-Destructive Testing and Quality Assurance (LZfPQ) at the University of Saarland in Saarbrücken. I would like to thank numerous people who supported me during these years.

First, my gratitude goes to Dr. Jens Prager for his guidance and supervision of this thesis. Thank you for giving me freedom in my research and your critical comments. I also very appreciate not only professional but also personal advice you gave me.

I would like to thank Prof. Dr. Christian Boller for his supervision and for reviewing my thesis. Your trust in me and freedom you gave allowed me to grow and to become an independent researcher.

Furthermore, I want to thank Prof. Dr. Michel Castaings for agreeing to review my thesis, and for his excellent comments and remarks on it. I really enjoyed the fruitful discussion during the PhD thesis defense.

This work would not be possible without Thomas Heckel who recognised my potential and hired me back then in 2016. Your encouragement along the way helped me to succeed.

I am very grateful to my colleague and friend Jannis Bulling who was always there for me with his advice and technical support. Your healthy scepticism and fruitful discussions with you helped to improve the quality of my research.

Furthermore, I would like to thank Dr. Gerald Martin Otto Hönig who taught me a lot in the beginning of my PhD on scientific conduct and values. Your curiosity fit mine well and I really enjoyed our discussions on any scientific topic. Moreover, thanks to you, I started to look into the mode repulsion closely and as the years showed it brought many fruitful results.

Also, many thanks to Sarah Johannesmann, Dr. Leander Claes and Prof. Dr. Bernd Henning at the University of Paderborn for successful collaboration on the topic of mode repulsion. I always enjoyed working with you.

Thanks to Dr. Olivier Mesnil for hosting me during my research stay at CEA in Paris-Saclay and supporting me on the application of wavenumber mapping. I am glad that we kept working together even after my stay and became not only good colleagues but also friends.

I want to thank all my colleagues at BAM for their continuous administrative and technical support. In particular, I would like to thank Mathias Diekjakobs, Fabian Kromme and Paul Wasmer for their support with numerical methods; Dr. Georg Mair, Dr. Ben Becker, Dr. Sebastian John and Eric Duffner for sharing their knowledge and expertise on composite pressure vessels; Daniel Brackrock and Dirk Gohlke for their technical support with ultrasonic measurements; Prof. Dr. Volker Trappe, Dustin Nielow, Marcin Jenerowicz, Carineh Ghafafian and Julian Marzik for their support with manufacturing of composite samples; Christian Koch for his technical support and the drawing of a composite pressure

vessel. Finally, a special thanks to Tobias Homann for his technical support in the laser lab.

Also, many thanks to Dr. Olaf Kahle from the Fraunhofer IAP in Teltow who provided the technical support with the impact testing.

A big thanks to Dr. Vittorio Memmolo from Università degli Studi di Napoli FEDERICO II for proof-reading the manuscript prior to its submission and your valuable comments on it. Your research stay in BAM helped me to finish the manuscript and finally submit my thesis.

Furthermore, many thanks to the interns and students with whom I got to work during these years, particularly Ali Can Epözdemir, Pia Chybiak, Maik Lauschkin, Kai Oehring, Franosch Georg and Jeffrey Thomsen. It was great to work with you.

A big thank you to my close friends Tatiana Mishurova, Sergei Evsevleev and Viktor Lyamkin, you made the dark times lighter.

Also, I am grateful to Itziar Serrano Munoz, Konstantin Prosolov, Tobias Fritsch, David Schumacher, Robert Stegemann and Valentin Serey, just chatting with you was already enough to cheer me up.

Lastly, I would like to thank my family and close ones for their love and support.

Nomenclature

Abbreviations

AE	acoustic emission
CFRP	carbon fibre-reinforced plastics
COPV	composite over-wrapped pressure vessel
EMT	Measurement Engineering Group
ET	effective thickness
FBG	fibre Bragg grating
FDIW	frequency domain instantaneous wavenumber
FEM	Finite Element Method
FFT	fast Fourier transform
GFRP	glass fibre-reinforced plastics
GW	guided waves
IDT	interdigital transducer
IW	instantaneous wavenumber
LDV	laser-Doppler vibrometer
LW	local wavenumber
MWCNT	multi-walled carbon nano-tube
NASA	National Aeronautics and Space Administration
NDT	non-destructive testing
OFDR	optical frequency domain reflectometry
PC	personal computer
PZT	lead zirconate titanate
SAFE	Semi-Analytical Finite Element Method

SBFEM	Scaled Boundary Finite Element Method
SH	shear horizontal
SHM	structural health monitoring
TOF	time-of-flight
UD	unidirectional
UT	ultrasonic testing
WRMS	weighted root mean square
ZGV	zero group velocity

Greek letters

$\boldsymbol{\epsilon}$	strain vector
$\hat{\boldsymbol{\psi}}$	amplitudes of nodal displacements and forces
$\boldsymbol{\sigma}$	stress vector
$\boldsymbol{\Lambda}$	eigenvalue matrix
∂_x	first-order partial derivative with respect to x
∂_y	first-order partial derivative with respect to y
∂_{xx}	second-order partial derivative with respect to x
α	parameter used in the sensitivity study
$\Delta\alpha$	parameter variation
ϵ	strain
η	local coordinate
κ^r	weighting function
λ	wavelength
λ_i	eigenvalues
ν	Poisson's ratio
ω	angular frequency
ϕ	signal phase
$\boldsymbol{\Psi}$	eigenvector
ψ	vector of nodal displacements and forces

ρ	density
σ	normal stress
τ	shear stress
θ	rotation angle

Latin letters

$\hat{\mathbf{q}}_\mathbf{n}$	amplitudes of inner forces
$\hat{\mathbf{u}}_\mathbf{n}$	amplitudes of nodal displacement
$\mathbf{B_1}, \mathbf{B_2}$	components of shape functions and their derivatives
$\mathbf{b_1}, \mathbf{b_2}$	component matrices
$\mathbf{c_1}, \mathbf{c_2}$	integration constants
$\mathbf{D}$	elasticity matrix
$\mathbf{E_0}, \mathbf{E_1}, \mathbf{E_2}$	SBFEM coefficient matrices
$\mathbf{f_i}, \mathbf{f_e}$	external forces acting on the boundary at position $x_i = 0$ and x_e at a certain length to x_i
$\mathbf{M_0}$	mass matrix
$\mathbf{N}$	matrix of shape functions
$\mathbf{q}$	inner forces
$\mathbf{S}^\infty$	stiffness matrix for an unbounded domain
$\mathbf{S}^\mathbf{b}$	stiffness matrix for a bounded domain
$\mathbf{T}$	transformation matrix
$\mathbf{u_i}, \mathbf{u_e}$	displacements resulting from the forces $\mathbf{f_i}, \mathbf{f_e}$ acting on the boundary at position $x_i = 0$ and x_e at a certain length to x_i
$\mathbf{u_n}$	vector of nodal displacements
$\mathbf{u}$	displacement vector
$\mathbf{Z}$	Z-matrix
$\mathcal{J}$	Jacobian matrix
$\mathcal{S}$	modes sensitivity
A	signal amplitude
c_L	longitudinal wave velocity

c_T	shear wave velocity
c_{gr}	group velocity
c_{ph}	phase velocity
D_{ij}	elasticity constants
E	Young's modulus
f	frequency
g	analytical signal
H	Hilbert transform
h	half of the plate thickness
K	number of points in the wavefield
k	wavenumber
L	domain length
n	number of parameters in the material vector
p	factor in Lamb equations expressed through k, ω, c_L
Q	factor to calculate the elasticity constants
q	factor in Lamb equations expressed through k, ω, c_L
r	weighting factor
t	time signal
W	wavefield
x, y, z	Cartesian coordinates, also corresponding to the directions 1,2,3

Contents

CHAPTER 1

Introduction

Structural parts made of layered materials surround us: bridges and buildings made of glued laminated timber, wind turbine blades and aircraft fuselage made of composite laminates, windows of buildings and cars made of laminated glass, *etc.* Such materials are employed due to different reasons, may it be lower costs, lighter weight, or higher strength, stiffness or toughness when compared to common materials. Naturally, this improved performance results in a more complex material behaviour, which in turn requires more intricate methods of quality assurance during design, production, and lifetime of a structural component. Many destructive and non-destructive testing (NDT) methods already serve this purpose, yet there is still a place and need for further developments.

Both destructive and non-destructive methods are used during design, development, certification, and production phases of a component. Moreover, they may accompany the component during its lifetime, *e.g.*, to be able to predict and prevent the reinforcement corrosion of a concrete bridge, cores are drilled to measure the chlorine concentration and penetration depth using NDT [1]. Note that drilling, by itself, is a destructive process, however the overall effect on the bridge lifetime is negligible. If the regulations require quality control only of some produced parts picked randomly out of one bunch, either destructive testing or NDT can be performed. However, when all parts must be checked, NDT is the only choice. For instance, all repaired parts of a jet engine must undergo NDT, with the typical methods used being X-ray, electromagnetic and liquid penetrant testing [1]. Other common NDT methods include thermographic and ultrasonic testing which are used, *e.g.*, for on-site inspection of wind turbine blades [2] and in-service testing of rails [3, 4], respectively.

When it comes to structural parts, such as buried pipes or offshore wind turbines, which are hardly accessible or which failures are related to high costs, it is preferable to install a

[1] Source: a guided tour at the Engine Overhaul Workshop of Air France

monitoring system to remotely assess the condition of the part. This concept has emerged in the 1970s [5], but first appeared in the wording *structural health monitoring* (SHM) in the late 1980s [6]. According to Cawley [5], NDT and SHM fields aim at assessing the condition of a structure non-destructively and can overlap depending on the definitions employed. His definition of NDT comprises an inspection of a structure by a technician using a removable measurement system without an attempt to compare current results to those obtained previously. While SHM is thought of as a permanently attached system which enables frequent measurements (not necessarily continuous) and signal comparison to the measurements taken previously.

The field of SHM has grown over the years and much literature giving a good overview of the field has been published by now [6–9]. Depending on the requirements, SHM can be performed on the whole structure (global monitoring), some area of it (large area monitoring) or a hot-spot (local monitoring) [5]. Global monitoring requires less sensors and is mainly sensitive to severe damage, while both large area and local monitoring typically require a dense network of sensors and thus may allow for early detection and localisation of small damage.

There are passive and active monitoring approaches, for instance, global monitoring of a bridge can be performed using a passive excitation caused by a traffic load or an active excitation by shakers. The same principles apply to large area and local monitoring, which can be done using acoustic emission (AE) or ultrasonic guided waves (GW). Both methods are based on wave propagation, with the former being a passive method meaning that the waves are generated while damage initiation, and the latter being an active method which requires an active excitation of waves to sense damage. While AE necessitates continuous monitoring so that no damage-related events are missed, monitoring using GW can be performed at time intervals to reduce the amount of data but still being sufficient to find critical damage before the failure of the component.

Many GW modes exist in a structure which behaviour is defined by material properties (density and elastic constants), material thickness, boundary conditions and frequency [10–13]. The art is that to find a right mode at a right frequency depending on a task for given material properties, thickness, and boundary conditions.

Over the years, many investigations with guided waves were carried out [14–17]. Some of these investigations resulted in the broad deployment and acceptance of the GW technique for NDE of oil and gas pipelines [18–21]. Mainly the fundamental modes, *i.e.*, first symmetric and antisymmetric modes, are used in the lower frequency range, since those are well understood and can be excited, measured and analysed without difficulty. Techniques based on GWs are therefore still under investigation to explore more complex applications such as wave propagation in multi-layered structures, *e.g.*, made of metal and polymers, fibre-reinforced

polymer composites, or metals in combination with fibre-reinforced polymer composites [22–31].

Outline of thesis This thesis studies the propagation of guided waves in multi-layered plates with the focus not only on the fundamental but also on high order modes. The main goal is to achieve a better understanding of how these waves propagate in such plates, what characteristic features exist and how they can be used for solving different engineering problems. The numerical and experimental analysis is performed for isotropic materials alone and in combination with anisotropic materials. Features are identified and described with respect to the material characterisation, NDT and SHM.

Chapter 2 presents the theory of guided waves, gives a short overview on ways to calculate the dispersion curves and model GW propagation. In many cases, material properties are missing or not precisely known when it comes to the modelling of GW. Therefore, the state of the art on the characterisation of effective elastic properties by ultrasonic bulk waves and guided waves is presented. Then, the current state in the characterisation of adhesive bonds is presented along with the research on GW mode repulsion. This is followed by the state of the art on COPV monitoring and GW-based damage quantification. Finally, the scope of the thesis is presented.

Overall methodology is presented in Chapter 3. It includes the basics on the Scaled Boundary Finite Element Method used all along this work to calculate dispersion curves, to model wave propagation and as a forward model in the optimisation procedure for the characterisation of effective elastic constants. The chapter also describes the numerical and experimental set-ups, and samples used. At last, the theory behind the optimisation procedure, sensitivity calculation and signal processing techniques are presented.

Chapter 4 presents the main findings of this thesis. These include the sensitivity analysis of GW to a change in material properties and the applicability of GW to infer these properties. Furthermore, the effect of mode repulsion is analysed as well as its potential to characterise weak and strong adhesive bonds is shown for the first time. The chapter concludes with the numerical and experimental investigations on damage detection in multi-layered structures.

The last chapter summarises the results and gives an outlook.

CHAPTER 2

State of the Art and Scope

2.1 Guided wave principle

Ultrasonic guided waves (GW) is a term which groups the waves guided by a structural boundary, *i.e.*, surface (Rayleigh) and edge waves, or two boundaries, *i.e.*, interface waves and waves in plates, rods and cylinders. GW can propagate over long distances and interact with different damage types. This work concentrates on plate waves which are also called Lamb waves after Sir Horace Lamb, who described them in 1917 [32]. In his work, he introduced two equations which can be found in [13] in the following form:

$$\frac{tan(qh)}{tan(ph)} = -\frac{4k^2pq}{(q^2-k^2)^2} \quad \text{for symmetric modes,} \tag{2.1}$$

and

$$\frac{tan(qh)}{tan(ph)} = -\frac{(q^2-k^2)^2}{4k^2pq} \quad \text{for antisymmetric modes,} \tag{2.2}$$

with p and q:

$$p^2 = \frac{\omega^2}{c_L^2} - k^2, \quad q^2 = \frac{\omega^2}{c_T^2} - k^2, \tag{2.3}$$

where h is the half of the plate thickness, ω the angular frequency, k the wavenumber, c_L and c_T are the longitudinal and shear wave velocities.

From these equations, it becomes obvious that wave modes depend on the frequency, plate thickness and wave velocities. The velocities are in turn dependent on material properties, such as density, Young's modulus, and Poisson's ratio. Moreover, it is very interesting

that both longitudinal and shear wave velocities contribute to symmetric and antisymmetric modes, since both variables p and q are present in Eq. (2.1) and (2.2).

The roots of Eq. (2.1) and (2.2) define the wavenumber at which a particular wave mode at a particular frequency will propagate within the plate of a certain thickness. The resulting wavenumber-frequency diagram is also called a dispersion relation. However, in practical applications, it is more common to work with phase and group velocities (wave speed) instead of the wavenumber. Therefore, the wavenumbers are converted into phase velocities simply by $c_{ph} = \frac{\omega}{k}$, whereas the group velocities can found by $c_{gr} = \frac{d\omega}{dk}$.

Figure 2.1 presents dispersion curves for an aluminium plate up to the frequency-thickness product of 20 MHz mm. The curves were calculated using in-house code based on the Scaled Boundary Finite Element Method. The theory behind the method is described in Chapter 3. Looking at the figure, it becomes apparent that many modes exist in this range. The higher the frequency-thickness product gets, the more modes exist in the plate simultaneously. Second, the phase velocity of a particular mode at a certain frequency-thickness product is not equal to the group velocity of the same mode at the same frequency thickness product which is due to the dispersive nature of GW. These two major characteristics of GW - their multi-modality and dispersive character - can be explored in many ways. For instance, a mode in a highly dispersive region (*e.g.*, the S0 mode at around 1.8 MHz mm in Fig. 2.1b) can be used for finding corrosion damage, since a small change in the thickness will result in a clearly measurable change in the group velocity.

In Figure 2.1 symmetric and antisymmetric modes are marked as S0, S1, S2, *etc.*, and A0, A1, A2, *etc.*, respectively. A0 and S0 modes are called fundamental modes because they exist at every frequency. At higher frequencies their velocities approach the velocity of the Rayleigh (surface) wave. All other modes are referred as higher order modes and appear at different cut-off frequencies in the dispersion diagram. The velocities of higher order modes converge to the velocity of the transverse wave at higher frequencies. Note that the maximum value which phase velocity, and thus, the wavelength can have, is not restricted, and tends to infinity, whereas the maximum group velocity is limited by the longitudinal velocity in the material. Moreover, the group velocity at the cut-off frequencies is equal to zero.

Another interesting feature of guided waves is that every mode has its own mode shape which as well depends on the frequency. A mode shape represents a wave structure and is characterised by the displacement amplitude at every point along the plate's thickness. It is common to consider in-plane and out-of-plane components of a mode shape separately, with the former being parallel and the latter being perpendicular to the plate's surface.

Figures 2.2 and 2.3 present the mode shapes of the A0 and S0 modes at two frequency-thickness products, 1.8 MHz mm and 3.6 MHz mm, respectively. The A0 mode has a larger out-of-plane displacement, whereas the S0 mode has a larger in-plane displacement, *i.e.*, see

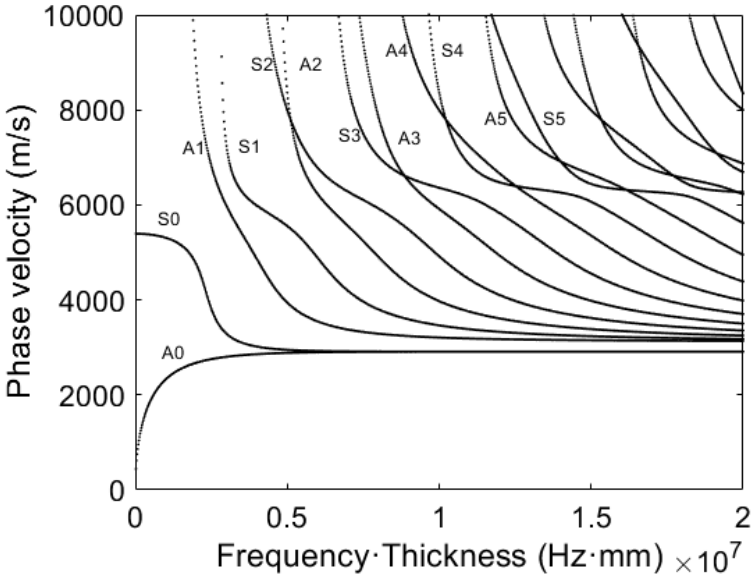

(a) phase velocity *vs.* frequency

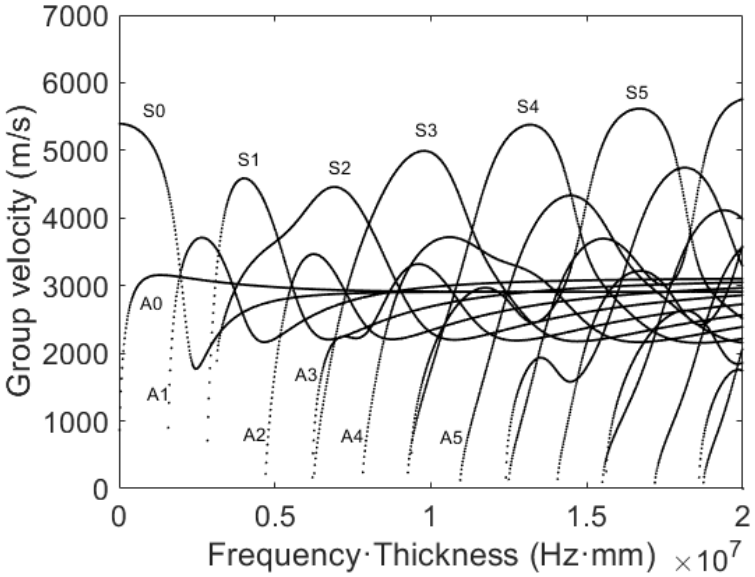

(b) group velocity *vs.* frequency

Figure 2.1: Dispersion curves for an aluminium plate.

Fig. 2.2b and Fig. 2.3b, respectively. Thus, symmetric modes are typically referred to as compressional and antisymmetric modes as flexural waves [13].

The out-of-plane displacement of the A0-mode is almost constant along the thickness of the plate at a low frequency-thickness value (Fig. 2.2a) and becomes more concentrated at the plate's centre at a high frequency-thickness value (Fig. 2.2b). The same applies to the in-plane displacement of the S0-mode (confer Fig. 2.2 and 2.3). It is very interesting that the out-of-plane displacement of the S0 modes increases at the plate's surface with a high frequency-thickness value.

The knowledge of a predominant displacement direction can be used, for example, to effectively excite one or another mode, *i.e.*, by using a piezoelectric element with a certain polarisation direction. Moreover, an improved sensitivity to certain defects located at a certain position across the thickness can be achieved by using a mode with the mode shape having dominant in-plane or out-of-plane displacement at this location [13].

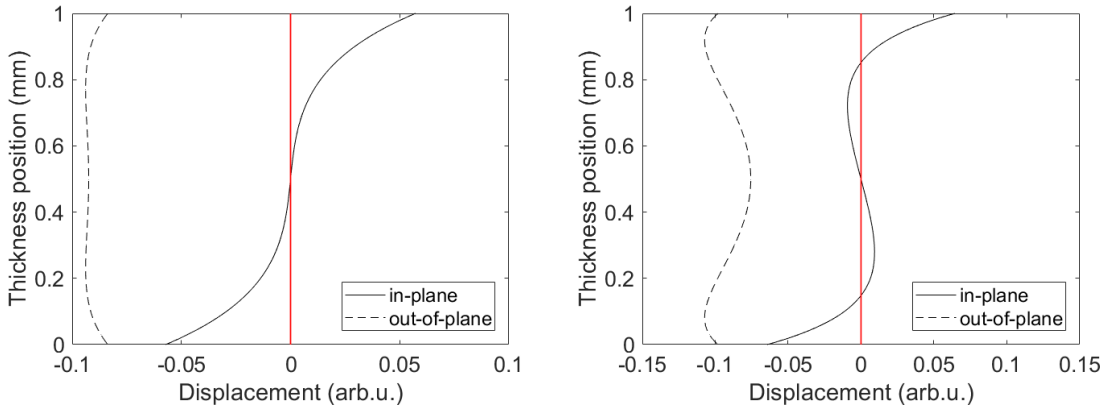

(a) 1.8 MHz mm (b) 3.6 MHz mm

Figure 2.2: Mode shapes of the A0 mode of an aluminium plate.

Furthermore, the interaction of GWs with obstacles results in transmission, reflection, and mode conversion of the waves. Let's consider a 5 mm steel plate with a 1.125 mm crack and the excitation using a 3-cycle Hann-windowed burst at the centre frequency of 200 kHz. The selective excitation of the A0 mode or the S0 mode is realised by applying normal forces at the opposite surfaces of the plate being in-phase or out-of-phase to each other, respectively. The selectively excited modes can be seen in Figures 2.4a and 2.5a, where the top and bottom figures show in-plane and out-of-plane displacement components, respectively. The A0 mode has dominant out-of-plane displacement along the whole thickness of the plate, whereas the in-plane displacement is high at the plate's surfaces and getting smaller to the plate's middle (see Fig. 2.4a), and *vice versa* for the S0 mode (see Fig. 2.5a). At the crack, the transmission and reflection of the A0 mode take place, as well as its conversion to the S0

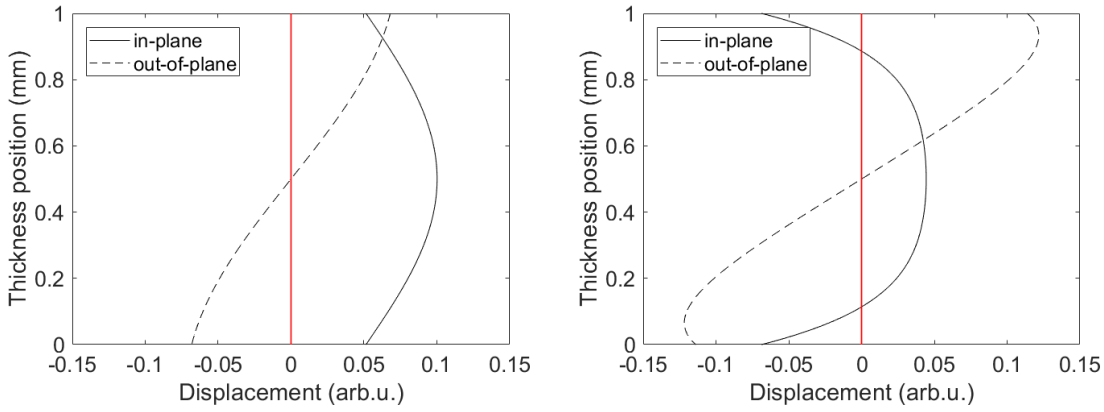

(a) 1.8 MHz mm (b) 3.6 MHz mm

Figure 2.3: Mode shapes of the S0 mode of an aluminium plate.

mode (see Fig. 2.4b). The same behaviour is also observed for the incident S0 mode which is transmitted through the undamaged portion of the plate, reflected at the crack and converted to the A0 mode. This behaviour is quite simple for the case of fundamental modes only but becomes complex when higher order modes are present as well as when the structures are anisotropic and consist of multiple layers [30, 31].

Due to dispersion and the multi-modal character of GWs, the development of damage detection techniques requires careful numerical modelling such that a realistic analysis of wave propagation and mode-damage interaction can be performed. The first step is to calculate dispersion curves, for which many approaches have been developed. One approach to derive the dispersion curves analytically is by finding the roots of the characteristic function [13, 33–35]. Another approach is based on semi-analytical methods which solve an eigenvalue problem [36–41]. One more possibility is to use a so-called spectral collocation method [37]. One of the first methods for the calculation of dispersion curves numerically is called the Thin-Layer Method [36]. Three methods that directly use finite elements for the approximation are the Semi-Analytical Finite Element (SAFE) [38, 39, 42, 43], the Waveguide Finite Element [40] and the Scaled Boundary Finite Element Method (SBFEM) [41]. These methods have early predecessors in the 1970s [44, 45].

Based on the dispersion curves, appropriate modes can be identified and considered for further analysis. At next, a numerical tool for modelling the propagation of the chosen GW modes is required. Numerous methods have been applied to wave propagation problems such as finite differences [46], finite volumes [47–49], finite element methods [28, 50], *etc.* An extensive review of simulation methods for the GW propagation analysis can be found in [51]. In general, each method has its advantages and disadvantages depending on the given problem, and there is no universal method suitable for solving every problem efficiently.

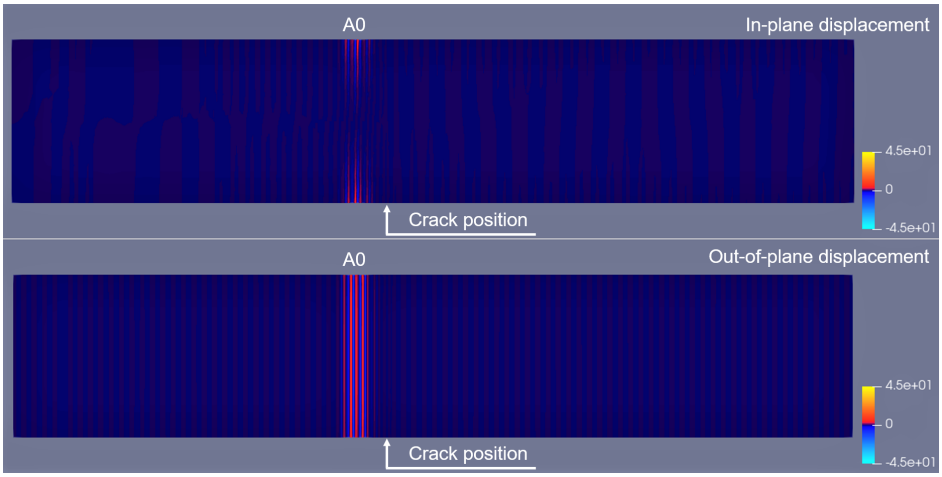

(a) 229.33 ms

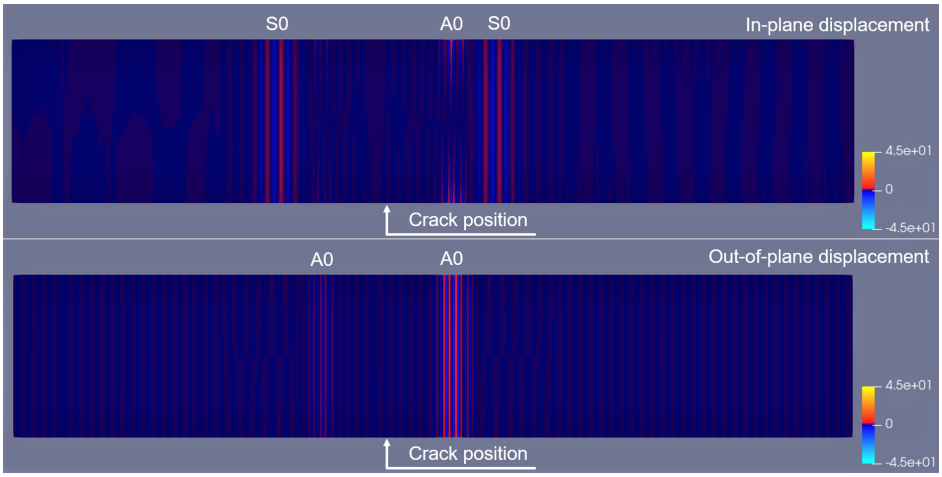

(b) 296.69 ms

Figure 2.4: (a) Propagation of the A0 mode in a 5 mm steel plate, (b) reflection of the A0 mode and its mode conversion to the S0 mode at a 1.125 mm crack open to the bottom surface of the plate.

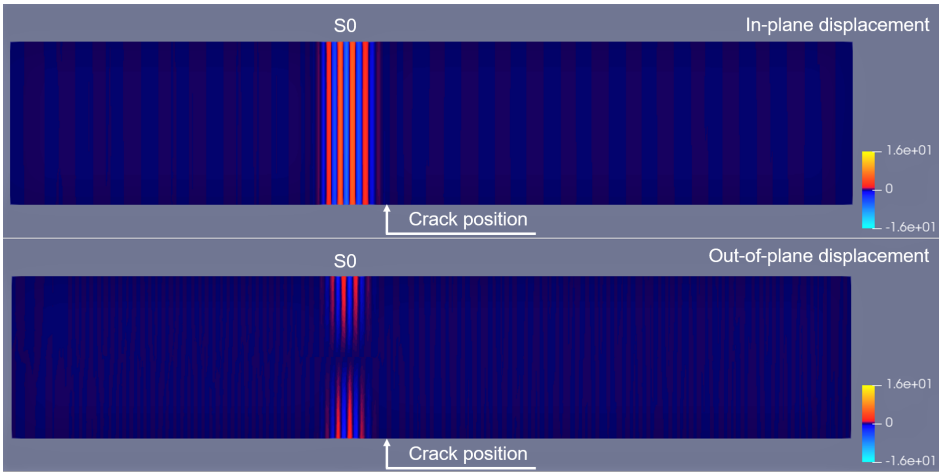

(a) 146.83 ms

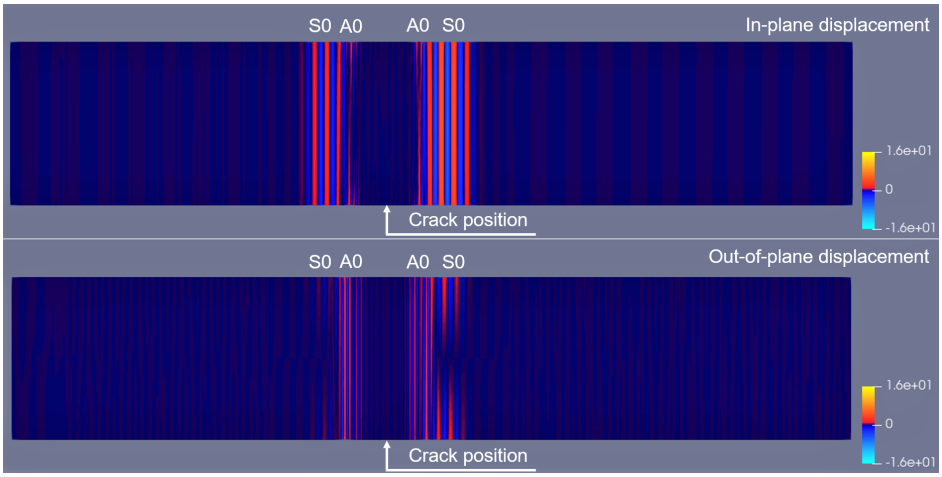

(b) 188.67 ms

Figure 2.5: (a) Propagation of the S0 mode in a 5 mm steel plate, (b) reflection of the S0 mode and its mode conversion to the S0 mode at a 1.125 mm crack open to the bottom surface of the plate.

In this work, the SBFEM is used in its two-dimensional representation for the analysis of the GW propagation. Compared to finite differences, finite volumes, and finite element methods, the SBFEM does not require full discretisation, thus reducing the computational effort significantly. It is suitable for calculation of dispersion curves, mode shapes and modelling of the GW propagation [41, 52–54]. The dispersion curves are computed with the SBFEM by discretising the cross-section (*e.g.*, the plate thickness) of an infinite domain using high-order elements. Multi-layered structures can be easily modelled using one element per layer having either isotropic or anisotropic material properties. This method is also highly efficient for modelling of the wave propagation in structures which have a constant cross-section. Because only the cross-section is discretised, the number of finite elements used in the SBFEM reduces drastically when compared to common finite element methods. Another feature of the SBFEM is that an infinite domain can be coupled with the domain of interest, thus avoiding unwanted reflections and by that simplifying the analysis of the wave propagation. The brief theory on the SBFEM is presented in Chapter 3.

2.2 Characterisation of effective elastic properties

A prior knowledge of effective elastic properties is crucial for modelling and analysis of wave propagation in various materials as well as for prediction of their mechanical behaviour. Depending on the material, different number of elastic moduli is required, starting from two for a case of general isotropy and going up to nine for orthotropic materials. It is especially challenging to obtain all elastic moduli for anisotropic materials such as polycrystalline metals or fibre-reinforced polymer composites, because established procedures are either destructive, require time consuming sample preparation and testing, or are not sensitive to all the moduli. There is therefore a need in a non-destructive testing method for the reconstruction of all elastic properties. Recent developments have shown that ultrasonic guided waves may tackle the problem due to their multimodal and dispersive behaviour [55, 56]. Different guided modes are sensitive to various elastic moduli, thus allowing more reliable reconstruction of all material properties [57–60].

Initially, measurements of elastic properties required machining of samples to obtain flat surfaces parallel to each other. The transmitter and receiver were placed on these surfaces to measure the velocities of bulk waves, from which elastic moduli were reconstructed [61]. With the growing use of fibre-reinforced polymer composites, the method for measuring elastic moduli non-destructively has been improved [62]. The machining of samples to the required shape was replaced by its rotation achieving the desired angle of incidence using immersion testing [62, 63]. Further developments also allowed to reconstruct viscoelastic properties of anisotropic materials using bulk waves [64, 65]. However, with this method it was not

possible to characterise thin samples. To overcome this shortcoming, Castaings *et al.* [66] proposed a new technique to infer elastic as well as viscoelastic properties of thin anisotropic plates by inverting the spectrum of the transmitted plane waves rather than the transmission coefficients only.

Another promising method for obtaining material properties in a non-destructive manner is based on GWs. The main advantage lies in their dispersive and multimodal nature providing sensitivity of various modes or frequency areas to different elastic moduli [57–60]. To gain more information for the reliable reconstruction of material properties the broadband excitation and acquisition is one of the key issues. These can be achieved using both a broadband PZT transducer or laser-based systems for excitation and sensing [55, 67–72]. The obtained experimental results are fitted to theoretical dispersion curves so that the best fit between two is achieved and thus the material properties are reconstructed. Here, two issues must be addressed. First, a fast method for calculation of dispersion curves, and second, a robust algorithm for the optimisation, must be chosen. The ways to calculate the dispersion curves for multi-layered plates were covered above. Regarding optimisation algorithms, many of them exist, such as gradient descent, simplex method, simulated annealing, genetic algorithms (GA), to name a few. The simplex, GA and machine learning approaches have been shown successful in the reconstruction of elastic constants [55, 56, 70, 72–79]. Note that machine learning approaches do not require dispersion curves at the reconstruction stage, but they do need a good database with dispersion curves of different materials for training and validation purposes. The advantage of the simplex and genetic algorithms over, *e.g.*, gradient descent, is that they are multidimensional methods searching for a truly global minimum value [6]. The simplex method has an advantage over the GA in its deterministic manner, however, its convergence strongly depends on the initial guess [80]. In this thesis, the simplex algorithm in combination of the SBFEM-based forward model is used in the optimisation procedure.

2.3 Characterisation of adhesive bonding strength

Currently, both industry and academia are keen to find a direct link between measured ultrasonic signals and the mechanical strength of the adhesive bonds, and to be able to distinguish weak interfaces (adhesive failure) from weak adhesive layers (cohesive failure), see these types of failure shown in Figure 2.6. In aerospace and automotive industries, where the demand on the adhesively bonded joints is increasing due to safety reasons, it is necessary to evaluate bond quality non-destructively.

Adhesive joints are preferred over mechanically fastened joints due to uniform distribution of stresses and thus higher fatigue resistance. Adhesive bonding is generally a process of

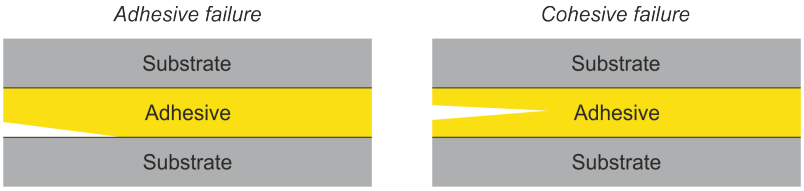

Figure 2.6: A schematic demonstrating a difference between adhesive and cohesive failure.

choice when it comes to assembling similar or distinct materials for lightweight applications in automotive and aerospace industries [81, 82]. Many NDT methods were developed over the years for assessing the adhesive bond quality: resonance testing (Fokker bond testing), AE, thermography, X-rays, shearography and ultrasonic testing [82]. However, mechanical destructive tests are still the only widely accepted way to characterise the mechanical performance of adhesive joints [83]. The main issue arises in inability to distinguish a weak bond from a strong one using non-destructively measured signals and thus to draw a conclusion about the mechanical strength of the joint. Nevertheless, researchers continue tackling the problem by using bulk ultrasonic waves [84, 85], Lamb waves [86–88] or shear-horizontal (SH) guided waves [89]. All these types of elastic waves have a potential in solving the problem because they mechanically interact with a bond while propagating in the structure.

Bulk ultrasonic waves have been used in reflection by Rokhlin *et al.* [90] and transmission by Budzik *et al.* [91] and shown to be more appropriate for the disbond detection, than for adhesion characterisation (interfacial stiffness). Testing using thickness resonances, developed by Fokker in the 1970s, is suitable for the defect detection such as delamination, voids, porosity, corrosion as well as the determination of adhesive layer thickness. Mezil *et al.* [88, 92] have followed the research on the thickness resonances by using the zero-group velocity (ZGV) Lamb wave resonance. They have demonstrated the sensitivity of ZGV Lamb modes to the interfacial stiffness under the condition that the bonding layer thickness is well known. SH guided waves have been used by Castaings [89] to characterise samples consisting of two aluminium plates adhesively bonded in a lap-joint. Different adhesion properties have been obtained by sandblasting or using oily agent on aluminium plates prior to bonding. The waves have been generated and measured at the part of the sample consisting of aluminium only. Different signals have been measured after passing the adhesive joint and used to develop numerical models accounting for strong and weak interfaces. In the follow-up research, Siryabe *et al.* [93] have shown that a-priory isotropic materials reveal anisotropy when the interfaces are degraded. However, to evaluate anisotropy level and to link it to the interface strength, the elastic moduli must be known, or *vice versa*. Another limitation of the proposed method is that interfacial properties cannot be resolved locally yet.

Different models exist to describe adhesive bonding in the context of ultrasonic waves - the perfect 3-layer model [85, 94], the 5-layer model [86, 95–98], the cohesive [87, 88, 99,

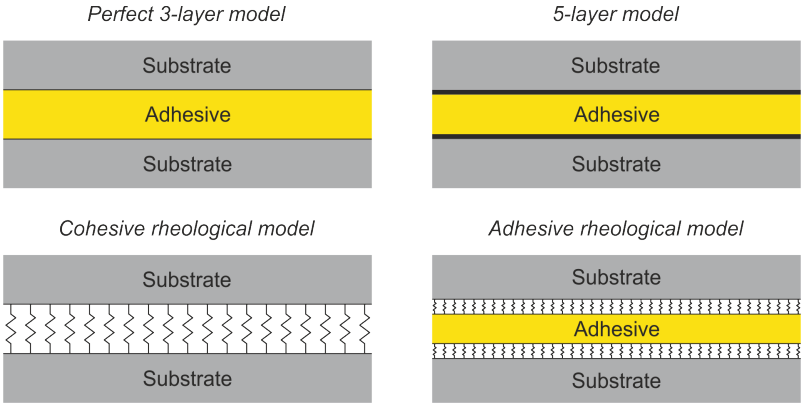

Figure 2.7: Models to describe the adhesive bonding behaviour for wave propagation problems.

100] and adhesive rheological models [89, 99]. A sketch presenting all models is shown in Figure 2.7 and a description is given in the following. The *perfect 3-layer model* considers the substrates and the adhesive as separate layers with continuity of stresses and displacements across the interface. This model does not account for weak interfaces and it can be extended to the *5-layer model* by adding two thin layers representing the interfaces. In the *cohesive rheological model* the adhesive layer and interfaces are mixed together and represented by springs. As a result, one cannot distinguish between adhesive, ones of interfaces, and cohesive properties, ones from adhesive layer itself. Whereas, the *adhesive rheological model* considers uniform distribution of springs across the interfaces allowing for separation of interfacial (adhesive) weakness from cohesive one, which for instance, may occur due to incomplete curing [91]. Both, the 5-layer and adhesive rheological models, are plausible if the properties of the adhesive layer must be separated from the actual adhesion between the adhesive layer and the substrates. Siryabe *et al.* [93] used the adhesive rheological model to account for apparent anisotropy, which has been shown to appear when interfaces are weak. The 5-layer model can be used as well, however under assumption that the thickness of interfaces is just a few micrometres. The latter model is used in this thesis to study the influence of weak and strong coupling on mode repulsion.

2.4 Guided wave mode repulsion

Mode repulsion of phase velocity curves has been observed for a metal plate as well as for a spherical shell when loaded by water [101]. It has been shown that the A0 mode of the plate is modified by the Scholte-Stoneley wave of the fluid resulting in two modes which repel each other at a certain frequency. Thus, the plate-borne Lamb mode (A0 mode) is coupled to the fluid-borne Scholte-Stoneley mode (A mode). Even though both modes are well separated in the phase velocity curve they exchange their character while passing through the repulsion

region. There are portions of the dispersion curve where one coupled mode possess the behaviour of the plate mode (A0 mode) which then changes the behaviour to the fluid mode (A mode) after passing the mode repulsion region, and *vice versa*. Such exchange of the behaviour of the waves has been known previously for the shift of atomic energy levels during formation of molecules [102].

Another study of mode repulsion has been done by Deschamps *et al.* [103], who considered limiting cases for two layers supporting only compressional (a fluid layer in *vacuo*) or shear (an artificial layer in *vacuo*) waves. Since the Lamb waves are represented by a combination of compressional and shear waves, it has been shown that adding a shear component to a fluid layer (purely compressional case) modified the dispersion curves so that mode repulsion regions appear. The resulting curves included Lamb modes of both purely compressional and purely shear cases with the repulsion regions at the positions where the Lamb modes of these two limiting cases intersected. This study has shown the influence of the coupling between compressional and shear vibrations of the plate on the Lamb wave modes. The less shear perturbation was present in the compressional case, the narrower was the distance between modes in repulsion regions so that the modes approximated the curves of the purely compressional case (fluid). Similar observations have been made by Maze *et al.* [104] for a fluid-loaded cylindrical shell.

Further interesting observations have been made by Simonetti [105] who investigated Lamb waves propagating in elastic plates coated with viscoelastic materials. It has been shown that in the regions where modes repulse the energy transfer from the elastic into viscoelastic layer is the highest, leading to high attenuation of Lamb wave modes at these frequencies due to high damping of the viscoelastic material. This allows to conclude that the mode repulsion region can be seen as a resonance phenomenon of both layers vibrating together.

Zaitsev *et al.* [106] and Kuznetsova *et al.* [107] investigated the coupling of different waves in piezoelectric plates. Authors refer to coupled acoustic waves as *hybrid waves* and to the effect as *waves' hybridisation*. Zaitsev *et al.* [106] have shown that for some crystallographic orientations hybridisation of waves occurs when one of the surfaces of the metallised piezoelectric plate is electrically shorted. Later Kuznetsova *et al.* [107] demonstrated the hybridisation of acoustic waves in a different piezoelectric material with one metallised surface being electrically shorted. If both surfaces have been electrically shorted no hybridisation of waves occurred. Moreover, a quantitative coefficient characterising the degree of hybridisation has been introduced. This result reinforced the study conducted by Zaitsev *et al.* [106] showing that there is a coupling effect between different elastic waves caused by electromechanical coupling. A similar effect has been observed earlier between the elastic and electromagnetic waves which can be coupled via magnetoelastic interactions

in ferromagnetic materials [108].

Therefore, mode repulsion represents the coupling between two waves which would not interact otherwise. This coupling effect may be caused either by a rearrangement of the internal material structure (*e.g.*, for piezoelectric or ferromagnetic materials) or by a modification of one wave propagating in a layer through another wave in another layer within multi-layered structures. The latter case is addressed in this thesis with the hypothesis that since mode repulsion appears in the dispersion curves of multi-layered structures then it should reflect the coupling between the individual layers and thus may allow for the non-destructive characterisation of adhesive joints.

2.5 Composite over-wrapped pressure vessels

Throughout the history of pressure vessel construction, five distinct types of vessel for gas storage applications have been developed [109]. Apart from the first type, which is made of metal, other types are composite vessels over-wrapped with fibre-reinforced polymer. These vessels can be subdivided into two main categories - with a load-sharing metallic liner and with a non-load-sharing plastic liner.

An example of a composite over-wrapped pressure vessel (COPV) with a load-sharing metallic liner is shown in Figure 2.8.

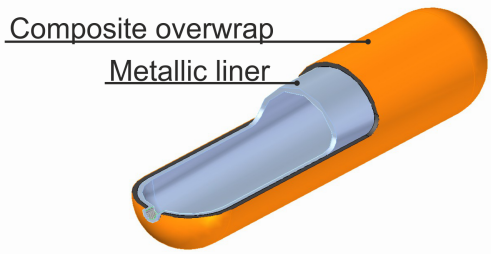

Figure 2.8: A composite over-wrapped pressure vessel with a load-sharing metallic liner. Adapted from own work published in [30].

According to NASA [110] four critical COPV failure modes exist:

1. *Burst from over-pressurisation* which occurs mainly during the design phase or in service due to malfunction of the external pressurisation equipment. This failure mode is well-understood and can be mitigated by appropriate design and testing.

2. *Fatigue failure of the metallic liner* is a failure mode occurring in service, which can be mitigated by NDT during manufacturing or pressurisation testing during qualification.

3. *Burst resulting from metallic liner or composite damage* may occur when a vessel was subjected to an impact. This failure mode is mitigated by appropriate protection from damage and damage-tolerance testing.

4. *Stress rupture or static fatigue of the composite over-wrap* due to composite degradation. This degradation results in a sudden structural failure of the composite over-wrap leading to serious injury and damage to the surroundings. This failure mode is not well-understood and currently cannot be predicted or assessed. Its mitigation is partially possible due to conservative design and thorough testing of COPV.

To date, a standard test procedure to assess the condition of COPV does not exist and needs to be developed. Due to this, a service lifetime of the vessels has been limited to 15 to 20 years depending on the application [111]. Despite this limitation and cost of COPV, the use is increasing due to their low weight. Therefore, to be able to ensure safe use of composite vessels and extend their lifetime, reliable testing, assessment, and monitoring procedures must be developed.

Conventional hydro-static pressure tests, used to assess the integrity of metal pressure vessels, do not provide reliable information about the current degradation of composite vessels [111, 112]. Therefore, various approaches have been proposed. Destructive tests of some of the vessels running in parallel with vessels being in service were suggested by Mair *et al.* [111]. An alternative approach is SHM, which would not only ensure a safer usage and extended lifetime but would also remove the necessity for periodic inspection or destructive tests.

One of the monitoring approaches is based on acoustic emission (AE) [113, 114]. Fischer analysed AE signals using neural networks and multivariate statistical analysis to predict burst pressures of COPV [113]. He showed that neural networks have a greater accuracy since they are not limited to a linear burst pressure equation. He concluded that analysis of amplitude distributions of the AE signals is not enough to adequately estimate burst pressure of the pre-damaged vessels, thus additional parameters, such as energy and duration are needed. Chou *et al.* [114] found that AE cannot distinguish fibre breakage from other damage events. Moreover, they showed that the total number of AE hits cannot be reliably used to estimate the remaining life of COPV. Alternatively, they proposed another indicator being a sudden rise in the number of AE hits, which however, occurs prior to stress rupture and thus would require an immediate removal of the COPV from service. All in all, AE monitoring showed promising results, but it is limited to the source of the AE signals which, once having appeared, could not be repeated.

Thus, continuous monitoring would be advantageous which can be done, *e.g.*, by using integrated optical fibres [115–119]. Mainly two approaches were investigated, one based

on local measurements using fibres with Bragg grating sensors (FBG) and the other on a distributed sensing by the Rayleigh-based optical frequency domain reflectometry (OFDR). In the first case, the FBGs have a defined Bragg wavelength that shifts when thermal or mechanical strain is applied, thus allowing for local strain and temperature sensing. In the latter case, the whole fibre can be seen as a long FBG with a random period at the positions of fibre imperfections [120]. The external change such as temperature or strain causes a spectral shift in the Rayleigh scattering, which, when calibrated, can be used for distributed sensing. Foedinger *et al.* [115] integrated the FGBs into a COPV and compared their response to the conventional strain gauges. Later, Degrieck *et al.* [116] showed a linear relationship between the Bragg wavelength and the pressure applied to COPV. Kang *et al.* [117] developed another technique of embedding FBGs into the filament of COPV to monitor the strains during a hydraulic test. The strains obtained by the FBGs at the hoop layers of a cylindrical part were similar to the strains measured by conventional strain gauges. Gasior *et al.* [118] used digital image correlation during the pressurisation of a COPV with the artificial defects to calibrate FBGs, which are to be used for SHM. As for distributed sensing based on the OFDR, Maurin *et al.* [121] first demonstrated the potential of the technique for SHM of COPV. Later, Saeter *et al.* [119] developed four methods for monitoring of impact damage using this technique. The most promising way of detecting the impact location was for the optical fibres wound continuously in the near hoop direction. Both damage location and its spread could be estimated to some extent. Thus, optical fibres can be used as strain sensors for impact damage detection, but a correlation between the strain changes and the residual life of COPV has yet to be found.

Xiao *et al.* [122] monitored the composite pressure vessels using multi-walled carbon nano-tube (MWCNT) sensors integrated into the filament. The MWCNT measures electrical resistance which changes due to the break of the conductive networks due to damage. However, it is not clear, what is the advantage of using MWCNT sensors to the conventional strain gauges.

Another promising approach is guided wave-based monitoring [27, 123–125], which has an advantage of being holistic with respect to detection and localisation of damage. Castaings and Hosten [27] analysed effects of moisture and micro-cracking in the composite over-wrap on the GW propagation in a COPV with a load-sharing metallic liner. They found out that the sensitivity to moisture content of the A0-like mode is higher in the longitudinal direction than in the circumferential direction of the vessel. Whereas for micro-cracking, it is the other way around. The measurements were done using air-coupled transducers which is suitable for periodic inspection rather than for online monitoring. However, their approach can be adapted to SHM by replacing the air-coupled transducers with permanently installed ones, as it was done by Bulletti *et al.* [123], who used interdigital transducers (IDT) permanently attached

to a COPV. Monitoring was done in the circumferential direction. They demonstrated the ability of the SHM system to detect and localise impacts having various energy. Moreover, they stressed out the necessity of selective excitation to achieve better sensitivity to a certain damage type. Yaacoubi *et al.* [124] performed 2D and 3D numerical analysis of guided wave propagation in a plate mimicking a structure of a COPV and a metal pressure vessel, respectively. Damage was modelled as a notch in the composite over-wrap and mode 2 was found to have the highest sensitivity to this type of damage.

In this thesis, damage related to the second and the third failure modes are investigated by means of guided waves. These failure modes are modelled as a crack in the metallic liner and delamination between CFRP plies, respectively.

2.6 Damage quantification using guided waves

Guided waves can be used not only for the detection and localisation of damage but also for its characterisation. On one hand, their multi-modal and dispersive nature allows different features to be explored, on the other hand it complicates the analysis [126–131]. Thus, various signal processing techniques have been developed for easier interpretation of signals and extraction of information about damage [132–140]. One of such techniques is wavenumber mapping which allows both quantification of size, depth and location of damage, *i.e.*, corrosion in metals [137] or impact-induced delamination in composite laminates [138, 140, 141].

Flynn *et al.* [137] and Rogge *et al.* [138] proposed two wavenumber mapping techniques simultaneously which allow for the evaluation of the size and depth of corrosion in metals and impact damage in composites, respectively. Both techniques are referred to as *local wavenumber* (LW) analysis and use similar pre-processing steps to filter unwanted modes leaving one mode of interest only. The difference between the techniques comes from the way how the filtered data is treated afterwards to retrieve the local wavenumbers. *Flynn et al.* [137] decreases the dimensionality of the data by three-dimensional enveloping and summing across time to retrieve spatially-distributed wavenumber estimates. The resulting LW is represented by the wavenumbers having the highest magnitudes at every spatial point. In contrast, Rogge *et al.* [138] multiply the data by a spatial window of a defined size and estimate wavenumbers locally within this window at the excitation frequency. The resulting wavenumber map consists of the dominant wavenumbers which are retrieved through the weighted sum of the windowed wavenumber spectra. Later, Mesnil *et al.* [140] developed another technique called *instantaneous wavenumber* (IW) mapping and compared it to the local wavenumber technique introduced by Rogge *et al.* [138]. The pre-processing of the wavefield was done in a similar way as in [137, 138], so that the mode of interest was isolated prior to the wavenumber mapping. The mapping itself is based on retrieving the

phase of the signals using the Hilbert transform. An unwrapping step in each direction is necessary to retrieve a continuous phase, which is then derived to calculate the wavenumber vector. The IW is the magnitude of the resulting wavenumber vector at a time instant. The authors also simplified the wavenumber mapping by introducing the concept of a single frequency wavefield analysis, which allows straightforward correlation of wavenumbers with the effective thicknesses and thus the damage depth. This technique is called Frequency Domain Instantaneous Wavenumber (FDIW). Parallelly, Juarez *et al.* [141] used a similar approach of one frequency to perform the local wavenumber mapping as of Rogge *et al.* [138] showing that it can be done in a more efficient way.

The IW and LW are implemented in this thesis and their performance is evaluated on a real impact-induced damage in a hybrid metal-composite plate for the first time.

2.7 Scope of the thesis

This thesis investigates the propagation of ultrasonic guided waves in multi-layered plates with the focus on higher order modes. The aim is to develop techniques for hybrid structures such as of adhesive bonds and COPV which are widely used in automotive and aerospace industries and are still challenging to inspect in a non-destructive manner.

In many cases, material properties are missing or not precisely known when it comes to the modelling of GW. Since the conventional testing is destructive and time-consuming, there is a need in a robust, reliable, and non-destructive method for the reconstruction of material properties. In this work, the GWs are used to infer the elastic properties of isotropic and anisotropic materials. Here, the procedure developed by [56, 67, 75, 76], is modified in terms of the experimental set-up and numerical model. The modified procedure is validated on an example of isotropic material first before its application to an anisotropic material. Moreover, the sensitivity study is performed to demonstrate the influence of different elastic moduli on GW modes [60]. Finally, the capabilities and limitations of the procedure used are presented. In this regard, the following questions will be addressed in section 4.1:

- *Do elastic properties influence GW modes in a unique way?*
- *Do the fundamental modes contain enough information to infer the properties of isotropic and anisotropic materials reliably?*
- *Are there characteristic features of GW modes which are affected by a change in elastic properties the most?*
- *Is the dispersion information from one wave propagation direction enough to reconstruct elastic constants of anisotropic materials?*

Knowing the material properties, the characteristic dispersion curves are calculated to perform further analysis and develop the concepts for damage detection, localisation, and evaluation for NDT and SHM of multi-layered structures. In this thesis, different aspects are investigated in this regard. At first, a multi-layered plate consisting of an isotropic metal layer bonded to an isotropic polymer layer is considered. An interesting feature, called mode repulsion, appears in dispersion curves while considering this multi-layered structure. For an uncoupled system represented by a single layer of an isotropic material, wave modes cross, meaning that they have the same phase velocity (wavenumber) at a given frequency but propagate with different group velocities without influencing one another [142]. In the case of a coupled system of two or more layers having different acoustic properties, the modes become coupled too. Two modes do not cross but converge instead. Their phase velocities (wavenumbers) are not equal at a specific frequency while the group velocities tend to the same value so that the modes propagate with the same velocity. Thus, a hypothesis is postulated: *Could mode repulsion be a measure of coupling between two (or more) layers?* To test the hypothesis, two systems - each having two isotropic layers bonded by a thin elastic layer - are analysed numerically and experimentally. For experimental investigations, which were conducted by Sarah Johannesmann from *Measurement Engineering Group* (EMT), University of Paderborn, Germany, layers are bonded using a coupling gel and glued together to represent weak and strong coupling, respectively. Additionally to the postulated hypothesis, the following questions will be investigated in section 4.2:

- *What features of mode repulsion can be used to characterise the coupling between layers?*
- *Are all mode repulsion regions influenced in the same way by a change in the coupling strength?*
- *What other influences besides the coupling state affect the modes in a repulsion region?*
- *Is it possible to distinguish between the longitudinal and transverse stiffnesses by means of mode repulsion?*

At next, a multi-layered plate consisting of an isotropic metal layer bonded to an anisotropic carbon fibre-reinforced polymer (CFRP) laminate is considered. This hybrid composite corresponds to the structure of a composite over-wrapped pressure vessels (COPV) with a load-sharing liner used for gas storage in automotive and aerospace industries. Different damage scenarios occur in the metallic part compared to CFRP part of the vessel. In this thesis, the interaction of GWs with a crack in the metallic part and delaminations in the CFRP part is studied numerically. These damages correspond to the second and third failure mode of COPV [110]. Two questions which motivated the investigation in section 4.3 are:

- *Is it possible to distinguish between damage in the metallic part from damage in the CFRP part?*
- *Are the fundamental modes in the low frequency range sufficient to distinguish between damage located in different parts of the structure?*

Further investigations are carried out experimentally on a similar hybrid composite plate studied previously. As a damage scenario, an impact-induced damage is considered, because it is one of the critical damage types of COPV which drastically reduces their lifetime. The goal is to localise and quantify the damage in three dimensions using wavenumber mapping [137–141, 143] and compare it to conventional ultrasonic testing (UT). Two wavenumber mapping approaches - local wavenumber [138] and instantaneous wavenumber [140] - are implemented in section 4.4 and their performance is compared on the real impact-induced damage for the first time.

CHAPTER 3

Methodology

3.1 The Scaled Boundary Finite Element Method

The SBFEM has been proposed by Wolf and Song in 1997 [144] and found many applications in elastostatics [145, 146] and elastodynamics [147–149] over the years. The basic idea of the SBFEM is to discretise the boundary of a computational domain only and to translate the resulting mesh along a *scaling direction* so that the complete geometry can be described. Thus, resulting in a reduction of a two-dimensional domain to a one-dimensional boundary, and a three-dimensional domain to a two-dimensional surface. Gravenkamp *et al.* were the first to recognise and demonstrate the effectiveness of the SBFEM for computation of the dispersion curves [41, 150–154] and modelling of the guided waves propagation and their interaction with damage [52, 53, 155].

There are several reasons why the SBFEM is well suited for guided waves problems. First, the propagation of GW is typically analysed in large structures, which, however, have a constant cross-section. Thus, only the cross-section needs to be discretised in the SBFEM and an analytical solution is used in the wave propagation direction. Second, an analytical solution can be used to describe a crack tip, thus avoiding the stress-singularity and mesh refinement [52, 156–159]. Third, in NDT and SHM applications, parametric studies have to be performed with slightly varying damage sizes or elastic constants. Therefore, the SBFEM allows not only to analyse mode-damage interaction but also to solve inverse problems in an efficient way (compared to standard finite element approaches), *e.g.*, for the reconstruction of elastic constants [160] or crack length from GW signals [161].

Only the key equations for plate with the constant thickness are summarised in the following. The detailed derivation of the SBFEM formulation can be found in [41, 155].

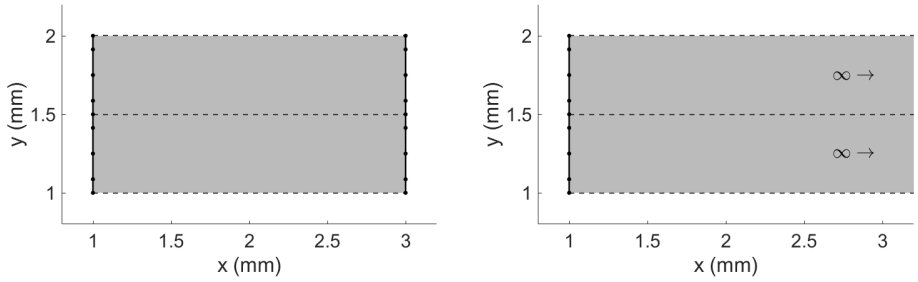

(a) (b)

Figure 3.1: Prismatic super elements: (a) bounded and (b) infinite.

The prismatic super element is suitable for modelling pieces with a constant cross-section. There are two cases either the piece is bounded, as in Figure 3.1a, or it is a semi-infinite piece, as in Figure 3.1b. All cross-sections are meshed with finite elements. For the bounded case, the mesh on the right-hand side is a translated version of the mesh on the left-hand side.

The displacement field $\mathbf{u}$ in the plate is described by a semi-analytical approach as follows

$$\mathbf{u} = \mathbf{N}(\eta)\mathbf{u_n}(x) \tag{3.1}$$

where $\mathbf{N}$ denotes the matrix of shape functions and $\mathbf{u_n}$ is the vector of nodal displacements. Note that each element is defined in its local coordinate η, which is equal to -1 and 1 at its extremities.

Using the semi-analytical stress-displacement relationship and the virtual work principle, the coefficient matrices $\mathbf{E_0}$, $\mathbf{E_1}$, $\mathbf{E_2}$ and the mass matrix $\mathbf{M_0}$ are obtained as [41]

$$\mathbf{E_0} = \int_{-\eta}^{\eta} \mathbf{B_1}^T \mathbf{D} \mathbf{B_1} |\mathcal{J}| d\eta \tag{3.2a}$$

$$\mathbf{E_1} = \int_{-\eta}^{\eta} \mathbf{B_2}^T \mathbf{D} \mathbf{B_1} |\mathcal{J}| d\eta \tag{3.2b}$$

$$\mathbf{E_2} = \int_{-\eta}^{\eta} \mathbf{B_2}^T \mathbf{D} \mathbf{B_2} |\mathcal{J}| d\eta \tag{3.2c}$$

$$\mathbf{M_0} = \rho \int_{-\eta}^{\eta} \mathbf{N}^T \mathbf{N} |\mathcal{J}| d\eta \tag{3.2d}$$

where $\mathbf{D}$ and ρ denote the elasticity matrix and the mass density, respectively, and $\mathcal{J}$ is the Jacobian matrix. The matrix is related to the transformation from the global to local coordinates. The matrices $\mathbf{B_1}$ and $\mathbf{B_2}$ are defined as

$$\mathbf{B_1} = \mathbf{b_1}\mathbf{N} \tag{3.3a}$$

$$\mathbf{B_2} = \frac{1}{\partial_\eta y}\mathbf{b_1}\partial_\eta \mathbf{N} \tag{3.3b}$$

with

$$\mathbf{b_1} = \begin{bmatrix} 0 & 0 & 1 \\ 0 & 1 & 0 \end{bmatrix}^T \tag{3.4a}$$

$$\mathbf{b_2} = \begin{bmatrix} 1 & 0 & 0 \\ 0 & 0 & 1 \end{bmatrix}^T \tag{3.4b}$$

Considering above definitions, an ordinary matrix differential equation for the displacement functions $\mathbf{u_n}(z)$ in the frequency domain can be derived [41]:

$$\mathbf{E_0}\partial_{xx}\mathbf{u_n}(x) + (\mathbf{E_1}^T - \mathbf{E_1})\partial_x\mathbf{u_n}(x) - \mathbf{E_2}\mathbf{u_n}(x) + \omega^2\mathbf{M_0}\mathbf{u_n}(x) = 0 \tag{3.5}$$

Eq. 3.5 can be rewritten as a homogeneous first order differential equation [41]

$$\partial_x\boldsymbol{\psi}(x) = -\mathbf{Z}\boldsymbol{\psi}(x) \tag{3.6}$$

where

$$\mathbf{Z} = \begin{bmatrix} \mathbf{E_0}^{-1}\mathbf{E_1}^T & -\mathbf{E_0}^{-1} \\ \omega^2\mathbf{M_0} - \mathbf{E_2} + \mathbf{E_0}^{-1}\mathbf{E_1}^T & -\mathbf{E_1}\mathbf{E_0}^{-1} \end{bmatrix} \tag{3.7}$$

and

$$\boldsymbol{\psi}(x) = \begin{Bmatrix} \mathbf{u_n}(x) \\ \mathbf{q_n}(x) \end{Bmatrix} \tag{3.8}$$

and with the inner nodal forces defined as

$$\mathbf{q_n}(x) = \mathbf{E_0}\partial_x \mathbf{u_n}(x) + \mathbf{E_1}^T \mathbf{u_n}(x) \tag{3.9}$$

The general solution of Eq. 3.6 can be postulated as [53]

$$\boldsymbol{\psi}(x) = \exp^{\boldsymbol{\Lambda} x}\, \boldsymbol{\Psi} \tag{3.10}$$

where $\boldsymbol{\Lambda}$ and $\boldsymbol{\Psi}$ are the solutions of the eigenvalue problem

$$-Z\boldsymbol{\Psi} = \boldsymbol{\Psi}\boldsymbol{\Lambda} \tag{3.11}$$

The diagonal entries of $\boldsymbol{\Lambda}$ contain the eigenvalues λ_i connected through $\lambda_i = ik_i$ to the wavenumbers k_i of modes existing in the structure.

The eigenvectors are represented by the columns of $\boldsymbol{\Psi}$ and thus contain the information about the mode shapes of displacements and forces. Note that integration constants are needed to calculate the amplitudes of the displacements and forces [53].

$$\hat{\boldsymbol{\psi}} = \begin{Bmatrix} \hat{\mathbf{u}}_\mathbf{n} \\ \hat{\mathbf{q}}_\mathbf{n} \end{Bmatrix} \tag{3.12}$$

The general solution of (3.6) consists of blocks which correspond to propagating or decaying modes in negative and positive x-direction [53]:

$$\boldsymbol{\psi}(x) = \begin{bmatrix} \boldsymbol{\Psi}_{11} & \boldsymbol{\Psi}_{12} \\ \boldsymbol{\Psi}_{21} & \boldsymbol{\Psi}_{22} \end{bmatrix} \begin{bmatrix} \exp^{\boldsymbol{\Lambda_p} x} & 0 \\ 0 & \exp^{\boldsymbol{\Lambda_n} x} \end{bmatrix} \begin{Bmatrix} \mathbf{c_1} \\ \mathbf{c_2} \end{Bmatrix} \tag{3.13}$$

where $\mathbf{c_1}$ and $\mathbf{c_2}$ are integration constants. Here, the wavenumbers having a negative (positive) imaginary part describe evanescent modes decaying in the negative (positive) direction. The propagation modes are the ones having real wavenumbers which must be identified using the group velocity c_{gr} of the modes by [150]:

$$c_{gr} = \frac{d\omega}{dk} = i\frac{\hat{\mathbf{u}}_\mathbf{n}^* \hat{\mathbf{q}}_\mathbf{n} - \hat{\mathbf{q}}_\mathbf{n}^* \hat{\mathbf{u}}_\mathbf{n}}{2\omega \hat{\mathbf{u}}_\mathbf{n}^* \mathbf{M_0} \hat{\mathbf{u}}_\mathbf{n}} \tag{3.14}$$

where the star denotes the conjugate transpose. Whereas the phase velocity c_{ph} is simply

defined as $c_{ph} = \frac{\omega}{k}$.

Further, the boundary conditions can be introduced at both ends of the waveguide. For a bounded domain (a domain of a finite length L as shown in Figure 3.1a), the general solution is evaluated at $x_i = 0$ and $x_e = L$, relating the displacements $\mathbf{u_i}$, $\mathbf{u_e}$ to external forces $\mathbf{f_i}$, $\mathbf{f_e}$ as follows

$$\begin{Bmatrix} \mathbf{f_i} \\ \mathbf{f_e} \end{Bmatrix} = \begin{bmatrix} -\boldsymbol{\Psi}_{21} & \boldsymbol{\Psi}_{22}\exp^{-\boldsymbol{\Lambda}_n L} \\ \boldsymbol{\Psi}_{21}\exp^{\boldsymbol{\Lambda}_p L} & \boldsymbol{\Psi}_{22} \end{bmatrix} \times \begin{bmatrix} \boldsymbol{\Psi}_{11} & \boldsymbol{\Psi}_{12}\exp^{-\boldsymbol{\Lambda}_n L} \\ \boldsymbol{\Psi}_{11}\exp^{\boldsymbol{\Lambda}_p L} & \boldsymbol{\Psi}_{12} \end{bmatrix}^{-1} \begin{Bmatrix} \mathbf{u_i} \\ \mathbf{u_e} \end{Bmatrix} \tag{3.15}$$

Hence, the stiffness matrix $\mathbf{S^b}$ for a bounded domain is given as [53]

$$\mathbf{S^b} = \begin{bmatrix} -\boldsymbol{\Psi}_{21} & \boldsymbol{\Psi}_{22}\exp^{-\boldsymbol{\Lambda}_n L} \\ \boldsymbol{\Psi}_{21}\exp^{\boldsymbol{\Lambda}_p L} & \boldsymbol{\Psi}_{22} \end{bmatrix} \times \begin{bmatrix} \boldsymbol{\Psi}_{11} & \boldsymbol{\Psi}_{12}\exp^{-\boldsymbol{\Lambda}_n L} \\ \boldsymbol{\Psi}_{11}\exp^{\boldsymbol{\Lambda}_p L} & \boldsymbol{\Psi}_{12} \end{bmatrix}^{-1} \tag{3.16}$$

For an unbounded domain as shown in Figure 3.1b, only the modes propagating or decaying in the positive x-direction contribute to the stiffness matrix at the boundary, requiring $\mathbf{c_2} = 0$ in Eq. (3.13) and thus [53]:

$$\mathbf{f_i} = -\boldsymbol{\Psi}_{21}\boldsymbol{\Psi}_{11}^{-1}\mathbf{u_i} \quad \& \quad \mathbf{S}^{\infty} = -\boldsymbol{\Psi}_{21}\boldsymbol{\Psi}_{11}^{-1} \tag{3.17}$$

Analogously, $\mathbf{c_1} = 0$ for a plate extending to $-\infty$ resulting in $\mathbf{S}^{-\infty} = \boldsymbol{\Psi}_{22}\boldsymbol{\Psi}_{12}^{-1}$ [53].

3.1.1 Plane strain and plane stress

For a linear elastic material, the stresses $\boldsymbol{\sigma}$ and strains $\boldsymbol{\epsilon}$ are related by the Hooke's law, which in Voigt notation reads

$$\begin{bmatrix} \sigma_x \\ \sigma_y \\ \sigma_z \\ \tau_{yz} \\ \tau_{xz} \\ \tau_{xy} \end{bmatrix} = \begin{bmatrix} D_{11} & D_{12} & D_{13} & 0 & 0 & 0 \\ & D_{22} & D_{23} & 0 & 0 & 0 \\ & & D_{33} & 0 & 0 & 0 \\ & sym. & & D_{44} & 0 & 0 \\ & & & & D_{55} & 0 \\ & & & & & D_{66} \end{bmatrix} \begin{bmatrix} \epsilon_x \\ \epsilon_y \\ \epsilon_z \\ 2\epsilon_{yz} \\ 2\epsilon_{xz} \\ 2\epsilon_{xy} \end{bmatrix} \tag{3.18}$$

where D_{ij} are elasticity constants of the elasticity matrix $\boldsymbol{D}$, σ and τ stand for normal and shear stresses, respectively. Note that the elasticity matrix of this form is suitable for isotropic,

transversely isotropic and orthotropic material symmetries [162], which are described in detail in the following subsection.

Often, it is desirable that the models are simplified such as a three-dimensional domain is reduced to its two-dimensional representation. In linear elastodynamics this can be done by using either the *plane strain* or *plane stress* assumption. Plane strain assumes that the displacement field is independent of one coordinate, z in this case, meaning that the domain of interest is infinite in this direction. Hence, the strains are restricted to the xy-plane and the Hooke's law is written as

$$\begin{bmatrix} \sigma_x \\ \sigma_y \\ \tau_{xy} \end{bmatrix} = \begin{bmatrix} D_{11} & D_{12} & 0 \\ D_{12} & D_{22} & 0 \\ 0 & 0 & D_{66} \end{bmatrix} \begin{bmatrix} \epsilon_x \\ \epsilon_y \\ 2\epsilon_{xy} \end{bmatrix} \tag{3.19}$$

Note that because $\epsilon_z = 2\epsilon_{yz} = 2\epsilon_{xz} = 0$, the associated columns 3, 4, and 5 in the elasticity matrix can be simply removed.

On the other hand, the plane stress assumption is applied when the stresses are restricted to one plane, *i.e.*, $\sigma_z = \tau_{yz} = \tau_{xz} = 0$. To find the stiffness matrix in the plane stress approximation, the operations are done over the compliance matrix, which is the inverse of the stiffness matrix. First, the columns associated with the zero entries in the stress vector and the rows associated with the strains ϵ_z, ϵ_{yz}, ϵ_{xz} in the compliance matrix are removed. Then the stiffness matrix for an isotropic material is found by inverting the compliance matrix and the Hooke's law reads

$$\begin{bmatrix} \sigma_x \\ \sigma_y \\ \tau_{xy} \end{bmatrix} = \frac{E}{1-\nu^2} \begin{bmatrix} 1 & \nu & 0 \\ \nu & 1 & 0 \\ 0 & 0 & 1-\nu \end{bmatrix} \begin{bmatrix} \epsilon_x \\ \epsilon_y \\ 2\epsilon_{xy} \end{bmatrix} \tag{3.20}$$

where E is the Young's modulus and ν is the Poisson's ratio. The elasticity matrices for other material symmetries are not presented here, because the plane stress assumption is not used in this thesis.

3.1.2 Material symmetries

Various types of symmetries exist to capture the behaviour of different materials. For instance, wood or cross-ply composite laminates are described by the *orthotropic* symmetry. This symmetry requires 9 independent elastic constants in the elasticity matrix to be known as can be seen in Eq. (3.18). The equations to calculate the elements of the elasticity matrix

from the engineering constants are not stated here, because the orthotropic symmetry is out of scope of this thesis.

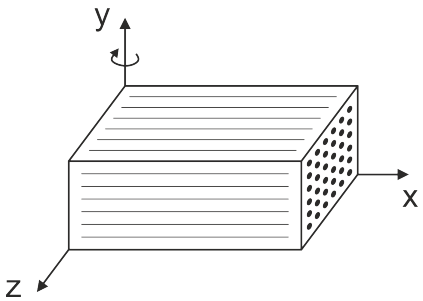

Figure 3.2: A composite ply with the x-axis along the fibre direction, the y-axis in thickness direction and the z-axis perpendicular to the fibre direction.

Another common type of material symmetry used for composite materials is the *transversely isotropic* symmetry which is defined by 5 independent elastic constants as: D_{11}, $D_{12} = D_{13}$, $D_{22} = D_{33}$, $D_{55} = D_{66}$, whereas $D_{22} = D_{23} + 2D_{44}$. This symmetry class includes unidirectional composite laminates and single unidirectional plies, and is typically used to model multi-layered composites [162]. Note that the direction '1' is along the fibres and correspond to the x-axis as it is shown in Figure 3.2, whereas the directions '2' and '3' correspond to the y-axis and z-axis, respectively. The elements of the elasticity matrix are defined by engineering constants as:

$$D_{11} = \frac{1 - \nu_{23}}{1 - \nu_{23} - 2\nu_{12}\nu_{21}} E_1 \tag{3.21a}$$

$$D_{12} = D_{13} = 2\nu_{12}(Q + G_{23}) \tag{3.21b}$$

$$D_{22} = D_{33} = Q + 2G_{23} \tag{3.21c}$$

$$D_{23} = Q \tag{3.21d}$$

$$D_{44} = G_{23} \tag{3.21e}$$

$$D_{55} = D_{66} = G_{12} \tag{3.21f}$$

with

$$Q = \frac{\nu_{12}\nu_{21} + \nu_{23}}{(1 - \nu_{23} - 2\nu_{12}\nu_{21})(1 + \nu_{23})} E_2, \quad \nu_{21} = \frac{\nu_{12}E_2}{E_1} \tag{3.22}$$

The simplest material symmetry is the *isotropic* symmetry having only 2 independent elastic constants, D_{12} and D_{44}. For this symmetry, the relations are: $D_{11} = D_{22} = D_{33} = D_{12} + 2D_{44}$, $D_{12} = D_{13} = D_{23}$, $D_{44} = D_{55} = D_{66}$, where D_{12} and D_{44} are defined as

$$D_{12} = 2\frac{G\nu}{1-2\nu} \tag{3.23a}$$

$$D_{44} = G = \frac{E}{2(1+\nu)} \tag{3.23b}$$

3.1.3 Change of coordinate system

To account for different plies from which composite laminates are made of a change of coordinate system is necessary. Assuming a composite ply with the fibre direction along the x-axis, the thickness direction along y-axis and the z-axis being perpendicular to both x- and y-axis as shown in Figure 3.2, for rotation by an angle θ counter clockwise (positive direction) about the y-axis, the transformation matrix $\mathbf{T}_y$ is

$$\mathbf{T}_y = \begin{bmatrix} cos(\theta)^2 & 0 & sin(\theta)^2 & 0 & 2cos(\theta)sin(\theta) & 0 \\ 0 & 1 & 0 & 0 & 0 & 0 \\ sin(\theta)^2 & 0 & cos(\theta)^2 & 0 & -2cos(\theta)sin(\theta) & 0 \\ 0 & 0 & 0 & cos(\theta) & 0 & -sin(\theta) \\ -cos(\theta)sin(\theta) & 0 & cos(\theta)sin(\theta) & 0 & cos(\theta)^2 - sin(\theta)^2 & 0 \\ 0 & 0 & 0 & sin(\theta) & 0 & cos(\theta) \end{bmatrix} \tag{3.24}$$

For the rotation about the z-axis, the transformation $\mathbf{T}_z$ is as follows

$$\mathbf{T}_z = \begin{bmatrix} cos(\theta)^2 & sin(\theta)^2 & 0 & 0 & 0 & 2cos(\theta)sin(\theta) \\ sin(\theta)^2 & cos(\theta)^2 & 0 & 0 & 0 & -2cos(\theta)sin(\theta) \\ 0 & 0 & 1 & 0 & 0 & 0 \\ 0 & 0 & 0 & cos(\theta) & -sin(\theta) & 0 \\ 0 & 0 & 0 & sin(\theta) & cos(\theta) & 0 \\ -cos(\theta)sin(\theta) & cos(\theta)sin(\theta) & 0 & 0 & 0 & cos(\theta)^2 - sin(\theta)^2 \end{bmatrix} \tag{3.25}$$

The rotation about the x-axis is not presented here, because it does not change the elasticity matrix in the case of transverse isotropy.

The rotated elasticity matrix $\mathbf{D}_\theta$ can be then obtained as

$$\mathbf{D}_\theta = \mathbf{T}\,\mathbf{D}\,\mathbf{T}' \tag{3.26}$$

In the SBFEM, the rotated elasticity matrix is calculated first and then reduced to a 2D case

using the plane strain assumption described above. This means that in the 2D approximation not every elastic constant contributes to the elasticity matrix. For instance, considering θ equals to 0° (no rotation) the elastic constants D_{11}, D_{22}, D_{12} and D_{55} define the elasticity matrix and thus the guided modes in the 0° direction (fibre direction). Whereas when θ equals to 90° for the rotation about the y-axis, D_{22}, D_{23} and D_{44} influence the modes in the 90° direction (perpendicular to the fibre direction), as can be seen in Figure 3.3.

Figure 3.3: The components of an elasticity matrix defining a composite ply in 0° (no rotation) and 90° rotation about the y-axis under the plain strain assumption.

3.2 Numerical set-up

Dispersion curves Dispersion curves used throughout this work are calculated by solving the eigenvalue problem in Eq. (3.11) for an unbounded domain (Fig.3.1b) in the SBFEM. For every case considered, material properties such as density and elastic constants, the thicknesses of the plates and the number of layers, are changed accordingly.

Wavenumber mapping To demonstrate and validate the wavenumber mapping, the GW propagation was modelled in 3D a 2 mm aluminium plate using the SHM module of the CIVA software. This numerical example is used in subsection 4.4.1 to demonstrate wavenumber mapping techniques. The SHM module of the software is based on a spectral finite element method which allows for efficient 3D simulations of the GW propagation [163, 164]. The maximum order of elements available in the software is the fifth order. The mesh size and time steps are set automatically based on the frequency and mode chosen for modelling. More details can be found in [165].

The numerical model including a damage of the dimension 40 x 40 mm^2 at the depth of 1 mm is shown in Figure 3.4. The material properties listed in Table 3.1 were used. The damage was modelled by disconnecting the nodes of the finite elements. The plate was

excited by a 3 Hann-windowed burst at the centre excitation frequency of 150 kHz. The transducer was not modelled physically but a force applied as an axisymmetric ring-shaped excitation with the outer and inner diameter of 20 mm and 19 mm respectively, was used (see the blue ring in Figure 3.4 marking the excitation area of the effective width of 1 mm).

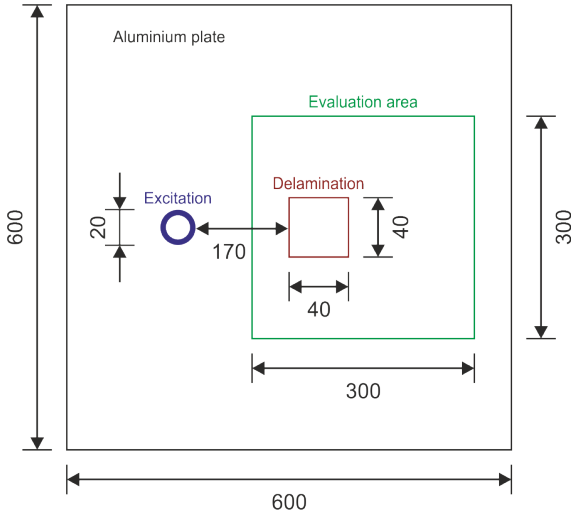

Figure 3.4: The numerical model used to demonstrate the wavenumber mapping techniques (not to scale) [166]. All dimensions are in millimetre.

Table 3.1: Material properties of aluminium.

ρ (kg/m^3)	E (GPa)	ν
2770	70	0.33

Wave propagation in a composite laminate Further, the SBFEM was used to model the wave propagation in a 2D plate made of an aluminium layer bonded to a CFRP laminate. Such structure corresponds to the one of a COPV with a load-sharing liner. The cylindrical structure of the vessel was approximated to a plate based on the criterion introduced by Wilcox [167]. This criterion states that if the ratio of the COPV's radius to its thickness is larger than 10:1 the curvature has a negligible influence on the GW propagation. Thus, the composite cylinder is approximated as a composite plate in this work. The plate consists of the aluminium plate with the thickness of 2 mm and the CFRP plate of layup $[0/90]_2$ with the total thickness of 4 mm. The rotation for 90° is done using Eq. (3.25). The CFRP plies are modelled individually being transversely isotropic with a 1 mm thickness of each. Note that the use of such a thick composite ply is motivated by the application of composite pressure vessels which have a very high fibre mass density, see section 3.3 for more details. Further, a firm connection between the layers is considered as it is the case in the application of pressure vessels. The material properties for aluminium and CFRP are listed in Table 3.1 and 3.2,

respectively. The main damage types considered are longitudinal cracks in the metal liner and delamination in the CFRP overwrap, *e.g.*, which can be caused by an impact damage.

The schematic of the numerical model is shown in Figure 3.5, which consists of: an excitation domain, an evaluation domain, a damage domain and two unbounded domains at both ends of the plate. The excitation was performed in both horizontal and vertical directions. The load distribution over the cross-section of the plate was in accordance to the mode shape of a mode chosen for investigations described in section 4.3. Note that such an excitation is impossible to realise in a real application, nevertheless, it has been used to study the behaviour of a single mode. The excitation in time was a Hanning-windowed tone burst with the centre frequency of the mode chosen for modelling. 4096 evaluation points were used over a 500 mm distance resulting in a 0.12 mm step. A 1 mm long crack of zero width was modelled in the aluminium part of the hybrid plate. Zero width is achieved simply by a disconnection of two SBFEM domains. A 10 mm long delamination in the CFRP laminate was modelled by disconnecting two SBFEM boundaries, thus representing a delamination of zero width between two CFRP plies. The delamination was modelled at four different positions as it can be seen in Figure 3.5 in separate simulation runs. The positions are counted from bottom to the top starting from the delamination between the aluminium plate and the CFRP laminate.

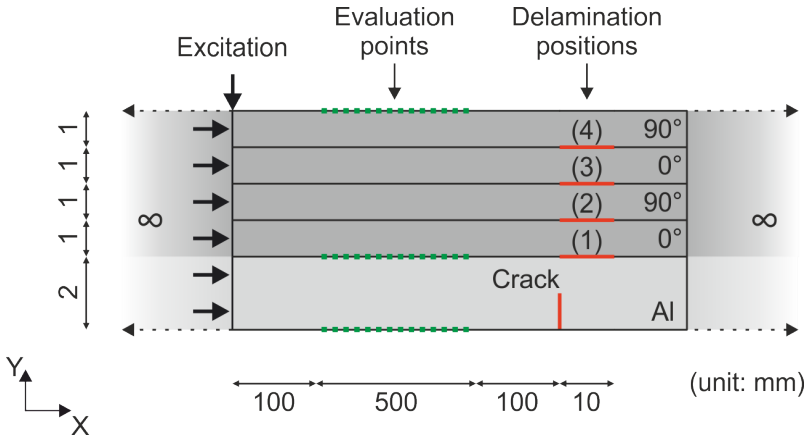

Figure 3.5: A schematic of the numerical model used in the SBFEM to model the GW propagation and their interaction with damage in the aluminium-CFRP plate. Adapted from own work published in [31].

Table 3.2: Material properties of the CFRP ply used, where 1 is in the fibre direction.

ρ (kg/m^3)	E_1 (GPa)	E_2, E_3 (GPa)	G_{12}, G_{13} (GPa)	ν_{12}, ν_{13}	ν_{23}
1490	121	8.6	4.7	0.27	0.4

3.3 Samples

Optimisation of elastic constants Two isotropic metals are used in the experiments - a 4.98 mm steel plate (grade 1.4301) and a 2 mm aluminium plate (grade 3.3535). Further, two anisotropic plates, an unidirectional (UD) and a cross-ply laminate, made of carbon fibre-reinforced laminate with the lay-ups of $[0]_3$ and $[0/90]_3$ are considered, respectively. SAERTEX®non-crimps fabrics with the total mass per unit area of 603 g/m^2 were used to produce the anisotropic laminates. This unidirectional fabric consists of ZOLTEK PANEX 35 50K carbon fibres which are held together with glass fibres and polyester sewing threads. Resin MGS™RIMR 135 and curing agent MGS™RIMH 137 from EPIKOTE™were used. Three and six layers of the fabric were used to produce the UD and cross-ply laminates, respectively. The test specimen was produced using vacuum assisted resin transfer moulding process. The thicknesses of the specimen was measured after the curing at different positions and average values of 2.1 mm (UD) and 4.2 mm (cross-ply) were taken. Considering the number of layers used in the lay-up, the resulting thickness of a single ply is equal to 0.7 mm. Material properties were calculated using as initial guesses the values for high tenacity carbon fibres and epoxy matrix given in *AlfaLam Software* from Darmstadt Technical University [168]. Material properties for a single ply are given in Table 3.3, where '1' is in the fibre direction, also called the 0° direction in the following. Density, ρ was measured separately and is equal to 1446 kg/m^3.

Table 3.3: Elastic constants of the CFRP ply calculated using the engineering constants from Table 3.2 considering $\rho = 1446\,\mathrm{kg/m^3}$.

D_{11} GPa	D_{12} GPa	D_{23} GPa	D_{44} GPa	D_{55} GPa
123.1	3.9	4.2	3.1	4.7

Mode repulsion Two isotropic materials, aluminium and polycarbonate, are used to analyse mode repulsion of guided waves. A single 1.5 mm aluminium plate was glued together with a 3 mm polycarbonate plate using a thin layer of epoxy resin. The resulting multi-layered plate represents the coupled system having strong interfacial coupling which is then used for the investigation of mode repulsion. Weak coupling is realised using coupling gel between a 1.45 mm aluminium plate and a 3 mm polycarbonate plate. The material properties are listed in Table 3.4.

Wavenumber mapping The sample is a $480 \times 480 \times 6\,\mathrm{mm^3}$ aluminium-CFRP composite plate build using the same prepreg and the resin transfer moulding process described above.

Table 3.4: Properties of the materials used in the investigations of mode repulsion.

Material	ρ kg/m^3	D_{11} MPa	D_{12}=D_{21} MPa	D_{22} MPa	D_{44} MPa
Aluminium	2562	102230	50354	102230	25940
Polycarbonate	1160	5860	3810	5850	993

The aluminium plate has the thickness of 2 mm and the CFRP plate of layup $[0/90]_3$ is 4 mm in thickness. A sketch of the sample is presented in Figure 3.6.

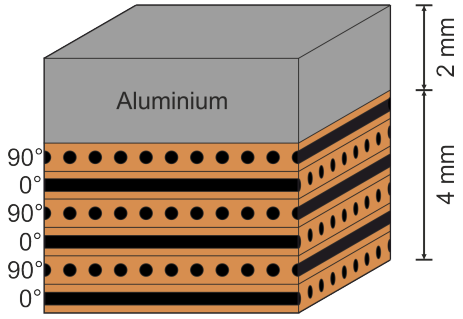

Figure 3.6: A sketch of the aluminium-CFRP composite plate used in the experimental investigations [166].

To damage the plate, a drop weight impact tester (*IM10, IMATEK*) was used. The plate was impacted from the CFRP side at three different locations with the impact energies of 5 J, 10 J and 30 J. The highest impact energy of 30 J used at the middle of the sample led to a plate deformation of a few millimetre visible at the aluminium side, but without perforation of the plate. Two smaller impacts were performed left and right from the centre of the plate laying on the diagonal 70 mm away.

3.4 Experimental set-up

In the following subsections experimental set-ups are described. Three set-ups were used in this work. The first one consists of a PZT for GW excitation and a 3D LDV for sensing. The measurements from this set-up serve as an input for the optimisation of elastic constants (line measurement) and wavenumber mapping (wavefield measurement). The second set-up was developed and is available in the Electrical Measurement Group (EMT) at Paderborn University. It is based on laser excitation of GW and their sensing with a PZT. This set-up is used for the analysis of mode repulsion. The third set-up is dedicated to high frequency ultrasonic testing in immersion which serves as a reference method for the characterisation of impact-induced damage in the aluminium-CFRP composite plate.

3.4.1 Guided waves measurement

The experimental set-up for the acquisition of GWs is shown in Figure 3.7. This set-up was used for measuring of the experimental dispersion curves (one line measurement) which serve as input in the optimisation procedure for obtaining elastic constants (see results in section 4.1) as well as for wavefield measurements used as input for wavenumber mapping (see results in section 4.4). Excitation is performed using a broadband PZT transducer (*Panametrics V101-RB/V102-RB Contact transducer, OLYMPUS Deutschland GmbH, Hamburg, Germany*) glued to the sample's surface with the goal to excite as many wave modes as possible. The resonance frequencies of the transducers are 0.5 MHz and 1 MHz, respectively. Frequency characteristics of the PZT used are provided by the producer and listed in Table 3.5. The minimum and maximum frequencies are measured at the full width at half maximum. The signal is generated using a function generator (*TG5011, AIM-TTI Instruments, RS Components GmbH, Mörfelden-Walldorf, Germany*), then amplified by a high-voltage amplifier (*HVA-400-A, Ciprian, Grenoble, France*) up to 400 V_{pp}, before driving the transducer. Two types of signals are used - a rectangular pulse and a sine burst. The rectangular pulse allows to excite the PZT at its resonance frequency, whereas the sine burst of a certain number of cycles at other non-resonance frequencies. Note that the more cycles are in the burst, the narrower is the frequency range. The signals are captured over an equally-spaced grid by a 3D laser-Doppler vibrometer (3D LDV) [*PSV-500-3D-HV, Polytec GmbH, Waldbronn, Germany*]. The white spray was used on the sample's surface to improve the amplitude of reflected light during the alignment of the vibrometer.

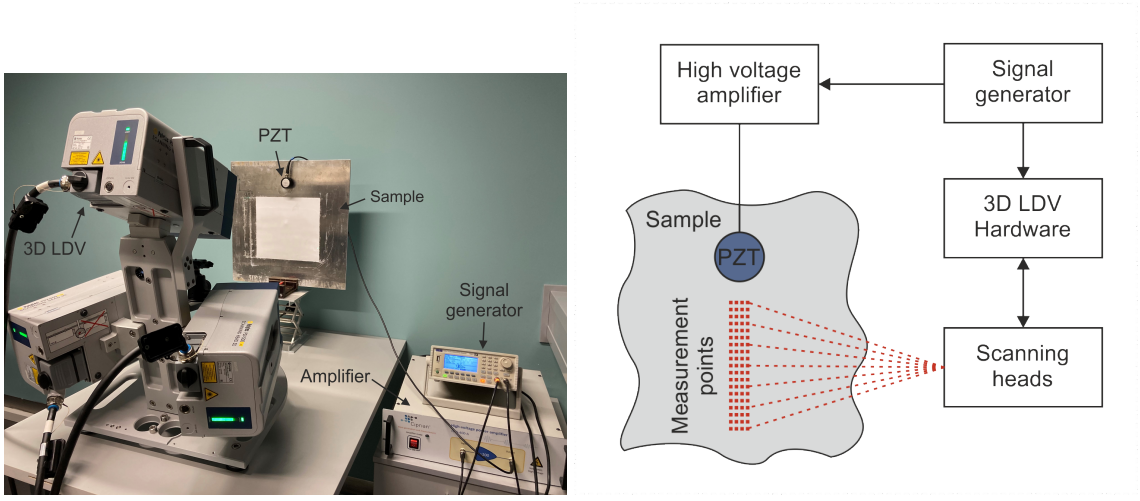

(a) (b)

Figure 3.7: The experimental set-up with a PZT and a 3D laser-Doppler vibrometer used for the GW acquisition (a) a photograph [166] and (b) a sketch.

For the analysis of guided wave mode repulsion (described in section 4.2), the set-up

Table 3.5: Frequency characteristics of the piezoelectric transducers used. The minimum and maximum frequencies are stated at the full width at half maximum.

Transducer	Resonance frequency MHz	Minimum frequency MHz	Maximum frequency MHz
V101-RB	0.5	0.28	0.78
V102-RB	1	0.52	1.43

depicted in Figure 3.8a developed in the Electrical Measurement Group (EMT) at Paderborn University is used. Ultrasonic broadband waves are generated thermo-acoustically by focusing short high energy laser pulses line-shaped on the specimen's surface [169]. The propagating waves are recorded by a purpose-built broadband PZT transducer working in the frequency range from 1 kHz to 10 MHz [67]. By moving the linear actuator, the specimen is excited at multiple distances to the receiver which measures the generated waves.

The measurement result is a temporal and spatial dependent signal matrix which is then converted into a frequency-wavenumber matrix using a two-dimensional fast Fourier transform (2D FFT) [170]. Figure 3.8b shows the resulting dispersion map of an aluminium plate, in which the propagating modes become visible as ridges. This image is called a dispersion map because of its similarity to dispersion curves. The higher the matrix values, the higher is the modes' displacement at the plate's surface [56, 67, 74, 75].

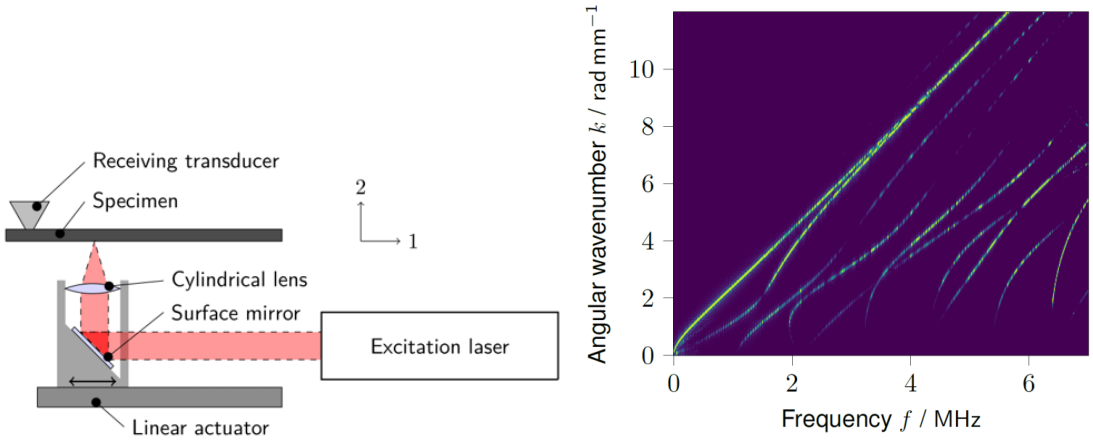

(a) (b)

Figure 3.8: (a) A sketch of the laser-induced broadband measurement system developed at EMT for the generation and detection of Lamb waves [67]. (b) A dispersion map for a 1.5 mm aluminium plate retrieved using the 2D FFT from the signals measured using the system.

3.4.2 Ultrasonic immersion testing

As a reference method for the characterisation of the impact damage in the aluminium-CFRP plate, ultrasonic bulk wave testing in immersion was used. The reference measurement

is needed to benchmark the wavenumber mapping results presented in section 4.4. The experimental set-up is shown in Figure 3.9. The scan was performed in the pulse-echo mode from the side of impacts (the CFRP side) with a focused 10 MHz PZT transducer (*IAP10.20100E, Krautkrämer*). The transducer's diameter is 20 mm, its focus is at 100 mm and its focal point is of approx. 0.75 mm. The transducer was positioned so that the focus was at the specimen's surface. The sampling frequency used was 100 MHz. The excitation signal was a needle pulse. The scan was performed over an area of 240 x 240 mm^2 centred on sample's middle using a 1.2 mm step. The amplification was set to 9 dB.

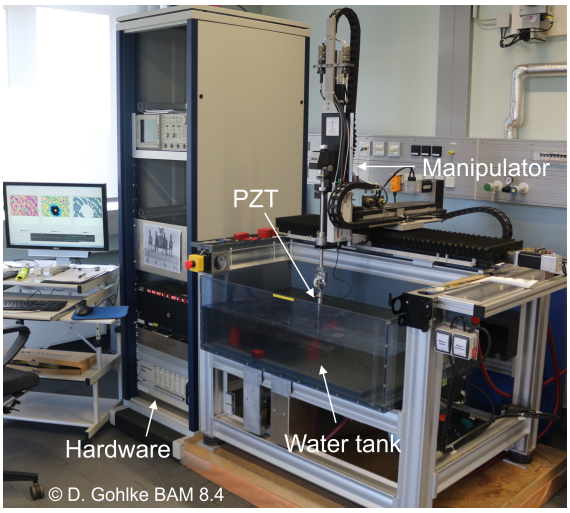

Figure 3.9: A photograph of the experimental set-up for ultrasonic immersion testing.

3.5 Characterisation of elastic constants

Figure 3.10 demonstrates the overall methodology used for the characterisation of elastic constants with the main constituents being the experimental set-up, forward model, cost function and optimisation algorithm. The main idea in the characterisation of elastic constants is to achieve the best fit between experimental and theoretical results by introducing a cost function, which is to be optimised iteratively. When the cost function is at its minimum, the optimal elastic properties are retrieved.

First, a fast method for calculation of dispersion curves and second, a robust optimisation algorithm have to be chosen. In this work, the procedure developed by [56, 67, 75, 76] is adapted by replacing the SAFE-based solver with the SBFEM-based solver. This leads to a faster optimisation due to higher order elements implemented in the SBFEM. Next, the experimental set-up is modified. Instead of the laser excitation and sensing using a broadband PZT, the set-up described in subsection 3.4.1 is used. Compared to a PZT transducer which is mainly sensitive to out-of-plane displacement used for GW acquisition in [56], the 3D LDV

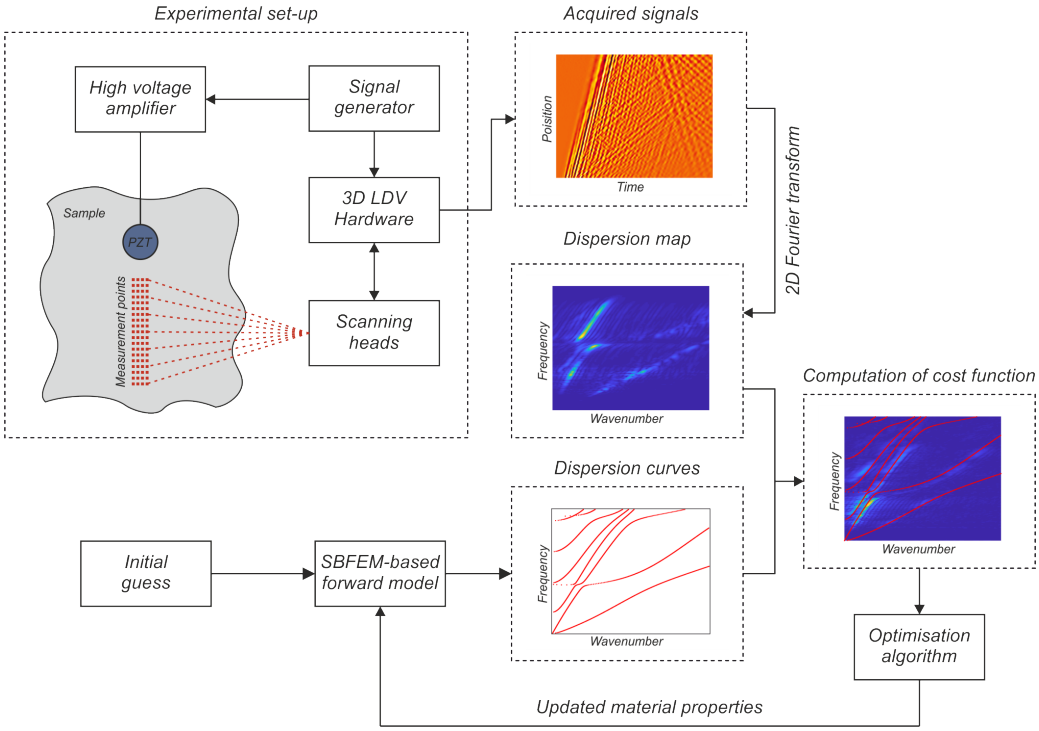

Figure 3.10: The flow chart of the procedure used for the GW-based characterisation of material properties.

allows to sense both in-plane and out-of-plane components of the propagating waves and thus gain more information for later characterisation procedure. Note that many averages are required to obtain a good signal-to-noise ratio while using the 3D LDV. For instance, 100 to 2000 averages per measurement point can be required depending on the material. Generally, more averages are needed for composite materials due to smaller displacements and high damping. However, a higher repetition frequency can be used because waves attenuate much faster, *e.g.*, for metals, the maximum repetition frequency which could be used was 100 Hz, whereas for composites it was 1 kHz. All in all, typical measurement times for one line of 150 points span between 30 minutes to 1.5 hours. Finally, acquired signals are transformed into a dispersion map using the 2D FFT [170]. Dispersion maps for in-plane and out-of-plane components for a steel plate can be seen in Figure 4.4.

Starting with an initial guess of elastic constants, the SBFEM-based forward model is used to calculate the dispersion curves which are then compared to the measured dispersion map. However, the direct comparison of the dispersion curves and the dispersion map is not possible because of different dimensionality of the theoretical and measured data (a set of discrete functions *vs.* the discrete matrix) [56]. Instead, Webersen *et al.* [56] proposed an elegant solution for obtaining the cost function without tedious image processing, which is usually required to extract the dispersion curves [171–173]. Every point obtained from the theoretical dispersion curve is directly evaluated on the experimental dispersion map to

extract the amplitude values. These points which are defined by frequency-wavenumber pairs correspond to wave modes. Then the amplitude values are averaged and inverted, so that an optimisation algorithm can converge to the minimum of the cost function. At the minimum value of the cost function, the best fit between measured and theoretical results is achieved and thus desired material parameters are reconstructed.

The Nelder-Mead simplex algorithm is used to find the minimum of the cost function. Ideally, at the minimum of the function, the theoretical predictions agree with the experimental results and, therefore, the optimal material parameters are retrieved. The algorithm is based on the work of Lagarias *et al.* [174] and provided by a *fminsearch* function in MATLAB.

Figure 3.11 shows the flow chart of the algorithm, which has the following steps: *(i)* construct the initial simplex; *(ii)* order the points in the simplex from the best (lowest function value) to the worst (highest function value); *(iii)* modify the simplex repeatedly using reflection, expansion, contraction, shrinkage transformations till the termination criterion is met.

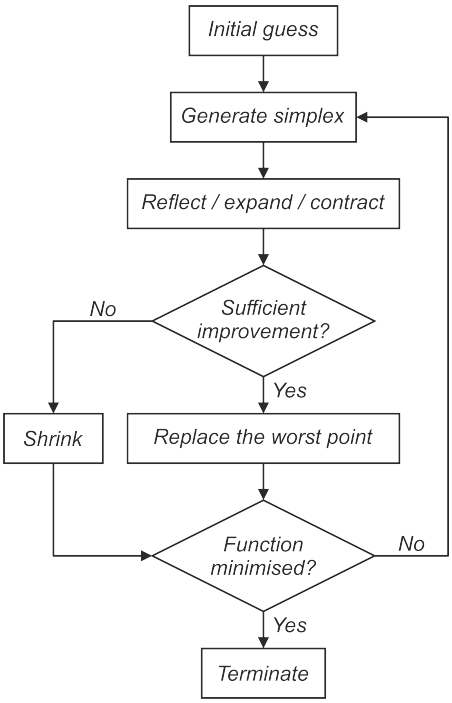

Figure 3.11: The flow chart of the Nelder-Mead simplex algorithm.

As an input for the algorithm, an initial guess of material properties is needed. In this work, there are 2 and 5 parameters in the material vector for the case of general and transverse isotropy, respectively. The density and the thickness of the material stay constant during the optimisation procedure and are measured in advance.

The initial simplex is constructed based on the initial guess and has $n + 1$ points, where n is the number of parameters in the material vector. Every point in the initial simplex

is represented by the vector of initial parameters, based on which additional vectors are calculated. These vectors are calculated by adding 5 % of each component to the respective component of the initial vector. Then the associated functions are evaluated and the points in the simplex are ordered from the lowest (best) to the highest (worst) function value. In every iteration step, simplex is first modified by using a reflection transformation, in which a new point and its corresponding function are calculated. If this point delivers a better function value than the worst point in the simplex, then the new point is accepted into the simplex and the iteration is terminated. Otherwise, the algorithm proceeds with an expansion transformation. An expansion point and its function value are calculated and then compared to the reflection point. The point which delivers the best function value is accepted into the simplex and the iteration is terminated. A contraction transformation is performed only in the case, when the reflected point is strictly better (has lower function value) than the second worst point. If the contraction point delivers better function value, it is accepted into the simplex and the iteration is terminated like in the previous cases. Otherwise, a shrinkage transformation is performed, where all points except the best one are replaced. The iterations proceed until both convergence and termination criteria are met. In this work, both criteria were set to $1e-4$. The output of the algorithm is a vector containing optimised material parameters.

3.6 Sensitivity calculation

In previous studies in the context of GW and the SBFEM [41, 150, 175], the modes are computed by prescribing the angular frequency ω_ℓ and solving the quadratic eigenvalue problem for the wavenumber k. For the sensitivity study the parametrisation via the wavenumber is used and the frequency of each mode f_ℓ is computed by $f_\ell = \omega_\ell^2/2\pi$ [60].

The sensitivity of the frequency S_{f_ℓ} as a function of the wavenumber at a given parameter α is evaluated by a finite difference as [60]

$$\mathcal{S}_{f_\ell}(k;\alpha) = \frac{\alpha}{100}\frac{df_\ell}{d\alpha}(k) \approx \frac{\alpha}{100}\frac{\Delta f_\ell}{\Delta\alpha}(k) = \frac{\alpha}{100}\frac{f_\ell(k;\alpha+0.5\Delta\alpha) - f_\ell(k;\alpha-0.5\Delta\alpha)}{\Delta\alpha} \tag{3.27}$$

with $\Delta\alpha$ being a parameter variation. For example, in an isotropic plate, the parameter α can be the Young's modulus E, Poisson's ratio ν or density ρ. Note that too small parameter variations can lead to significant round-off errors for finite differences. After investigating the differences between steps of the type $2^{-m}\alpha$ the optimal parameter variation $\Delta\alpha$ was found to be $2^{-7}\alpha$ [60].

3.7 Signal processing

Apart from the 2D FFT [170], also a 3D FFT [132] is used in this thesis to identify guided wave modes and filter unwanted modes prior to wavenumber mapping. The filtering procedure and the wavenumber mapping technique are described in subsection 3.7.2. Additionally, energy maps [176–178] described in the following are calculated and compared to wavenumber maps.

3.7.1 Energy maps

An energy map of propagating waves allow to visualise the distribution of energy in the measured signal and may highlight damage regions if there is a re-distribution of energy due to the mode conversion and reflection at damage [176]. A weighted root mean square (WRMS) approach of Segers *et al.* [177] is implemented in this work which allows to compensate for the attenuation of waves. To calculate the energy map, time signals at each spatial point of the wavefield are taken [177]:

$$\mathrm{WRMS}(x,y) = \sqrt{\frac{1}{K}\sum_{\kappa=1}^{K} W(x,y,t_\kappa)^2 \cdot \kappa^r} \tag{3.28}$$

where W is the wavefield and r is a positive weighting factor which is automatically calculated by [177]. The weighting function κ^r in the WRMS is used to compensate the attenuation. The signal is cut to the part with a relevant amplitude because the weighting function increases rapidly for a longer signal. Note that other approaches for the attenuation compensation such as a geometric weighting can be applied [178] which requires the exact transducer position. This approach was not used in this work because the transducer is not present in the area scanned.

3.7.2 Wavenumber mapping

The idea of the wavenumber mapping comes from the fact that wave modes change their wavelength (wavenumber) with the thickness. Consider a guided wave travelling in a waveguide made out of two materials, Material 1 and Material 2, with different acoustic properties as shown in Figure 3.12. This wave has a certain wavelength, λ_{total} in the areas of the waveguide where no damage is present. However, when travelling over the damaged area, *e.g.*, a delamination between Material 1 and Material 2, the guided wave will split into two wave modes - one travelling in Material 1 with λ_1 and the other in Material 2 with λ_2. Thus, the wavenumbers measured locally at one or the other side over the damaged region will be different from the ones of the pristine waveguide.

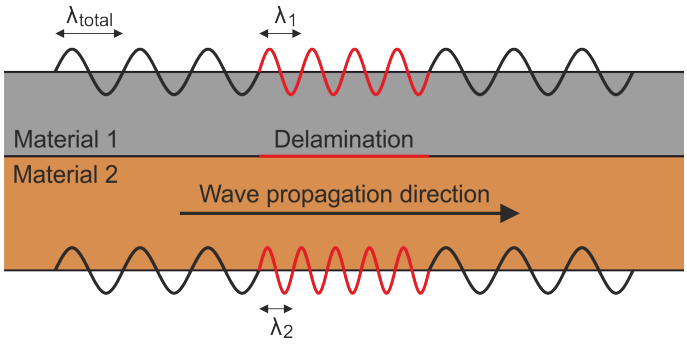

Figure 3.12: A sketch demonstrating the idea behind the wavenumber mapping.

To estimate the defect depth through the wavenumber mapping, it is necessary to find a relation between the wavenumber and defect depth. For this purpose, the effective thickness (ET) is defined, which is equal to the through-thickness distance between the measured surface and the defect closest to it. Note that for pristine regions, the ET is locally equal to the thickness of the plate, while for delaminated or corroded areas, it highlights the depth of the delamination or the residual thickness of the plate, respectively.

One issue when estimating the ET from the wavenumbers lies in the dispersive nature of guided waves meaning that the wavenumbers vary continuously with the frequency. Many wavenumbers which are present in the measured wavefield complicate the analysis. To avoid this, it is advantageous to work with one mode at one frequency at which the mode is most sensitive to the thickness changes. Therefore, an additional signal processing [132] is used prior to wavenumber mapping which is summarised in the following and in Figure 3.13.

The 3D FFT [132] is applied to the measured wavefield to separate the wavenumbers of the propagating modes for each frequency. The difference to the 2D FFT mentioned previously is that the 2D FFT is applied to a 1D domain (waves propagate along one spatial dimension, *e.g.*, in x), whereas the 3D FFT is applied to a 2D domain (waves propagate in two spatial dimensions, *e.g.*, in x and y, as can be seen in Figure 3.13). After applying the 3D FFT to the measured wavefield, the modes are separated according to their respective wavenumber for every propagation direction and frequency. Then the frequency of interest is selected and only the most sensitive mode is left by filtering other modes in the wavenumber domain. The filter is applied as a radial filter mask as it is shown in Figure 3.13, where the yellow area is equal to 1 and the dark blue area to 0. Note that the edges are smoothed using a median filter to decrease artefacts. In the last step, the resulting frequency slice which contains only one mode is transformed using the inverse 2D FFT to retrieve a single frequency wavefield.

There are different ways to estimate the wavenumbers locally [137, 138, 140]. Two approaches are used in this work - the instantaneous wavenumber approach of [140] and the local wavenumber approach of [138] - which are described in the following.

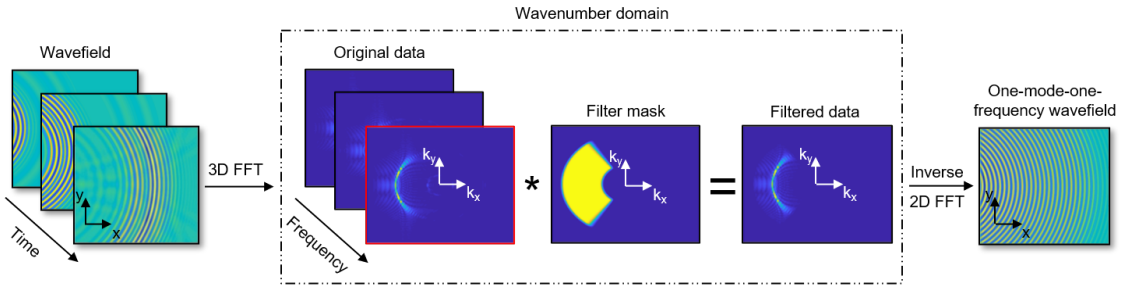

Figure 3.13: A diagram showing the workflow for the pre-processing of wavefield data prior to the wavenumber mapping [166].

Instantaneous wavenumber Mesnil *et al.* [140] differentiate between the instantaneous wavenumber (IW) and the frequency domain instantaneous wavenumber (FDIW). While the IW estimates the wavenumber from a wavefield at a single time instant, the FDIW measures it from a single frequency wavefield. The main difference lies in the reduction of data using a similar pre-processing procedure as shown in Figure 3.13 and described above. The core mathematical operations to calculate the wavenumbers out of displacement (or particle velocity) are the same for both the IW and the FDIW techniques [179, 180]. The short description of relevant steps is presented below, for more details the reader is referred to [179, 180]. For the sake of brevity, the name instantaneous wavenumber (IW) will be used instead of FDIW from hereafter and compared to the local wavenumber (LW) mapping, which is a different approach for the wavenumber estimation.

To calculate the IW the analytical signal $g(x, y, t)$ of the wavefield $W(x, y, t)$ has to be calculated first. This is done by applying the Hilbert transform H to the wavefield data [180]:

$$g(x, y, t) = W(x, y, t) + \mathrm{i}H(W(x, y, t)) = A(x, y, t)e^{\mathrm{i}\phi(x,y,t)} \tag{3.29}$$

The output of the transform are the amplitude $A(x, y, t)$ and the phase $\phi(x, y, t)$ of the wavefield. Then the first order derivatives of the phase have to be taken along both spatial dimensions separately resulting in two wavenumber vectors [180]:

$$\begin{aligned} k_x(x, y, t) &= \partial_x \phi(x, y, t) \\ k_y(x, y, t) &= \partial_y \phi(x, y, t) \end{aligned} \tag{3.30}$$

The IW is eventually given by the magnitude of these vectors [180]:

$$IW(x, y, t) = \sqrt{k_x(x, y, t)^2 + k_y(x, y, t)^2} \tag{3.31}$$

Local wavenumber The procedure for the LW mapping used in this work is based on the mapping procedure first described by Rogge *et al.* [138] and later used by Mesnil *et al.* [140] and Juarez *et al.* [141]. The basic idea of the approach is to multiply the wavefield data with a windowed function to be able to estimate the dominant wavenumber in a smaller region of the wavefield. The estimated wavenumber is assigned to the middle of the small region and the window is moved to the next, and so on till the whole area of the wavefield is fully covered. This procedure is analogous to a short time Fourier transform. The evaluation region and the assignment point for the window are shown in light and dark red colour in Figure 3.14, respectively. The spatially distributed displacements (particle velocities) are transformed within the window using the 2D FFT into the wavenumber domain. The wavenumber with the highest amplitude is then chosen and assigned to the midpoint. An important factor in the resolution of the technique is the spatial window size: a too large window results in the poor spatial resolution, whereas a too small window leads to low wavenumber resolution [138, 141]. It was found that the window size of twice the wavelength of the dominant mode provides an adequate wavenumber resolution [138, 141]. This window size is used in this work.

The last processing step applied to both IW and LW maps is filtering by a median filter to reduce the influence of the measurement noise. Then the filtered wavenumber maps are converted into ET maps using the respective dispersion relation.

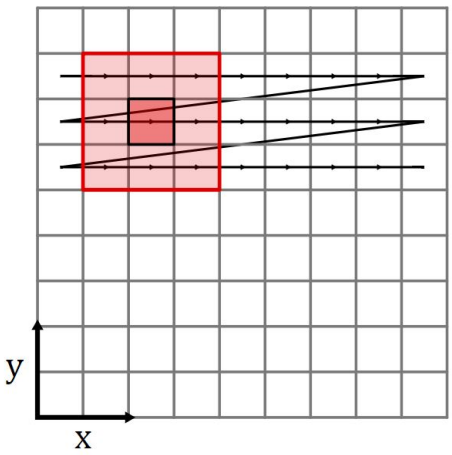

Figure 3.14: A sketch of a window used for the local wavenumber estimation. The evaluation region and the assignment point are shown in light and dark red colour, respectively [166].

CHAPTER 4

Results

4.1 Characterisation of elastic constants

Two material symmetries - isotropic and transversely isotropic - were chosen to analyse the influence of the material properties on GW modes and to demonstrate the GW-based characterisation of material properties.

4.1.1 Isotropic material

At first, the dispersion curves of two common metals are compared. For these two sets of material properties available in literature for aluminium and steel are taken. The material properties, named as Set 1 and Set 2, are listed in Table 4.1. Figures 4.1a and 4.1b present the dispersion curves of the 2 mm aluminium and steel plates. From Figure 4.1a it is observable that the first three modes (counted with respect to the frequency axis) have exactly the same behaviour for both materials. The small differences between the modes start from the fourth mode and increase with both the mode's order and frequency. As for the dispersion curves calculated using material properties of Set 2 (Figure 4.1b), the variation in dispersion curves between two metals is bigger and can already be observed for first three modes in the frequency range from 1 MHz.

Table 4.1: Isotropic materials properties used to calculate dispersion curves in Figure 4.1.

	Set 1		**Set 2**	
Property	Aluminium	Steel	Aluminium	Steel
E (GPa)	70	200	72	211
ν	0.33	0.3	0.42	0.24
ρ (kg/m^3)	2700	7850	2650	7830

This difference can be explained as follows. If Young's moduli of aluminium and steel are scaled by the respective densities, the resulting moduli for Set 1 are then equal to 25.9 MPa and 25.5 MPa, and for Set 2 are equal to 27.2 MPa and 27 MPa, respectively. These small differences in the moduli have little influence on the modes. Therefore, the main difference between two sets of materials comes from the difference in their Poisson's ratios, which is 10 % for Set 1 and 75 % for Set 2. It can be concluded that the influence of the Poisson's ratio on guided modes becomes more pronounced with higher frequencies (see Figure 4.1). In the following, the sensitivity analysis is performed to analyse this influence in detail.

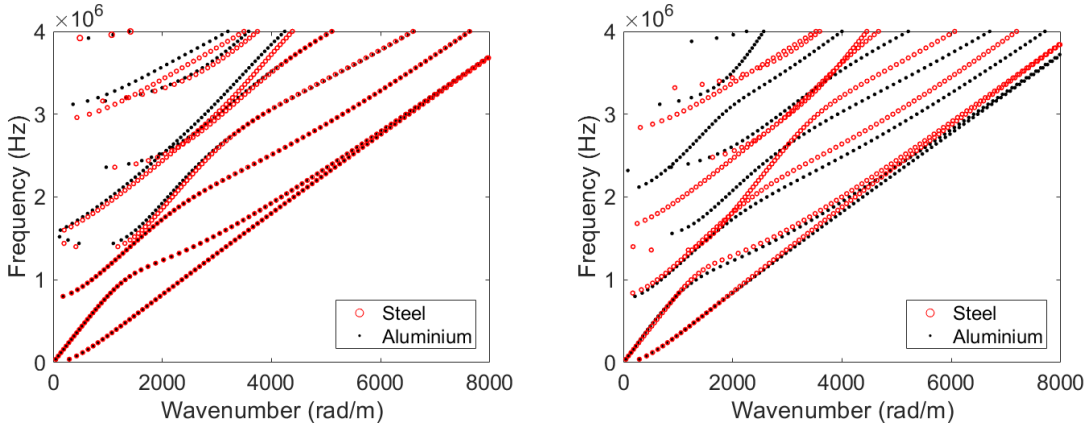

(a) Set 1 (b) Set 2

Figure 4.1: Comparison of dispersion curves of steel and aluminium plates with the same thickness calculated using (a) Set 1 and (b) Set 2 material properties from Table 4.1.

Sensitivity analysis For the sensitivity analysis, a 2 mm aluminium plate with the material properties from Set 1 (Table 4.1) is considered. All three material parameters, the Young's modulus, Poisson's ratio ν and density ρ are examined. The sensitivity analysis is performed as described in section 3.6.

Figure 4.2a shows the effect of the Young's modulus variation on the dispersion curves. In this diagram, the typical dispersion curves are extended by a colour value that corresponds to the modes sensitivity in Hz to a 1 % change in the modulus. In Figure 4.2a all sensitivity values are positive meaning that all curves move up with an increase in the Young's modulus. The diagram for the density (Figure 4.2b) is identical to the one for the Young's modulus apart from a changed sign. Both material parameters lead to a linearly changing sensitivity $\mathcal{S}_{f_t}$ with increasing frequency.

More interesting is the effect of the Poisson's ratio on the dispersion curves which leads to local non-linear changes in sensitivity as can be seen in Figure 4.2c. In this figure both negative and positive sensitivity values can be observed. Consequently, some parts of the mode curves move downwards, whereas others move upwards. The S1 mode and the S2 mode

are the modes with the lowest cut-off frequencies which show a high value of sensitivity $\mathcal{S}_{f_\ell}$.

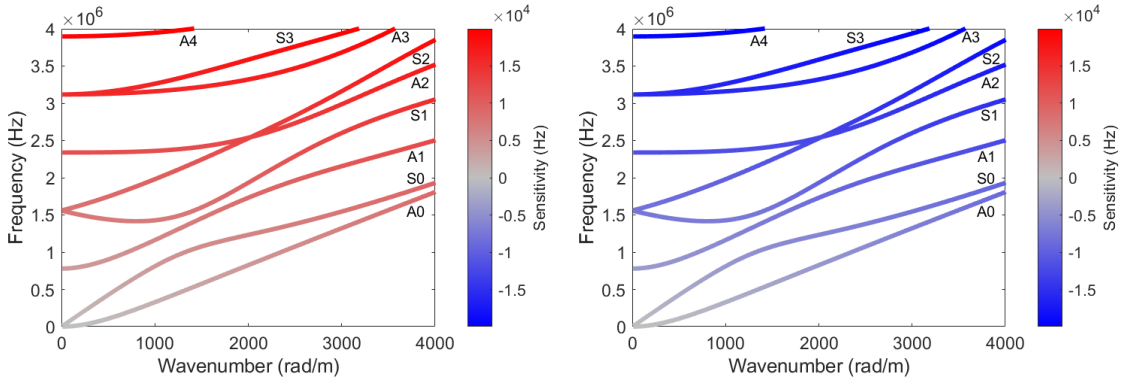

(a) $\mathcal{S}_{f_\ell}(k;E)$ (b) $\mathcal{S}_{f_\ell}(k;\rho)$

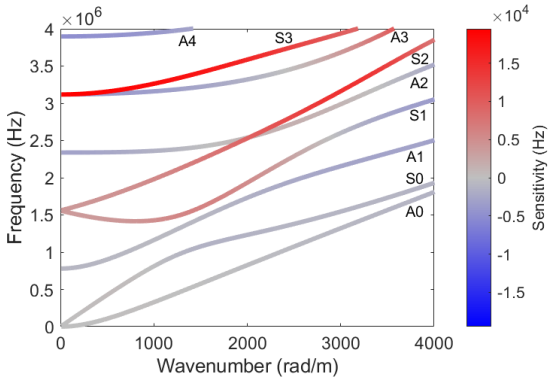

(c) $\mathcal{S}_{f_\ell}(k;\nu)$

Figure 4.2: Comparison of mode sensitivity $\mathcal{S}_{f_\ell}$ to a 1 % change of aluminium material properties.

Optimisation based on synthetic data To evaluate the performance of the optimisation algorithm described in section 3.5, the synthetic data were generated using the SBFEM. This allows to have reference material properties for the validation of the optimisation procedure. The same 2 mm aluminium plate with the material properties from Set 1 listed in Table 4.1 is used for modelling in the SBFEM. The resulting dispersion map is shown in Figure 4.3a. Eight modes are successfully excited with the chosen numerical set-up providing a lot of information for the optimisation procedure.

To test the reliability of the optimisation procedure in the dependence of number of modes available, the initial dispersion map is cut in the frequency and wavenumber domains to reduce the number of modes used in the optimisation procedure. Three cases are considered: the whole dispersion map with 8 modes and two reduced dispersion maps with 5 and 2 modes corresponding to Case 1, 2 and 3, respectively. The overview of the cases along with maximum number of modes, frequency and wavenumber used is presented in Table 4.2.

The initial guess for the Young's modulus and Poisson's ratio is 60 GPa and 0.4, respectively. These values are taken so that the calculated dispersion curves (white dots) do not overlay with the simulated dispersion map as it can be seen in Figure 4.3b. The initial guess is the same for all three cases considered. The resulting optimised values for the Case 1 are 69.984 GPa and 0.3296 which is in the close agreement with the reference values of 70 GPa and 0.33 for the Young's modulus and Poisson's ratio, respectively. The dispersion map superimposed with the dispersion curves (white dots) calculated using the optimised elastic constants is presented in Figure 4.3c. Other two cases with the reduced number of modes, which are not shown here for brevity, deliver similar values and converge to the reference values. The results are summarised in Table 4.3.

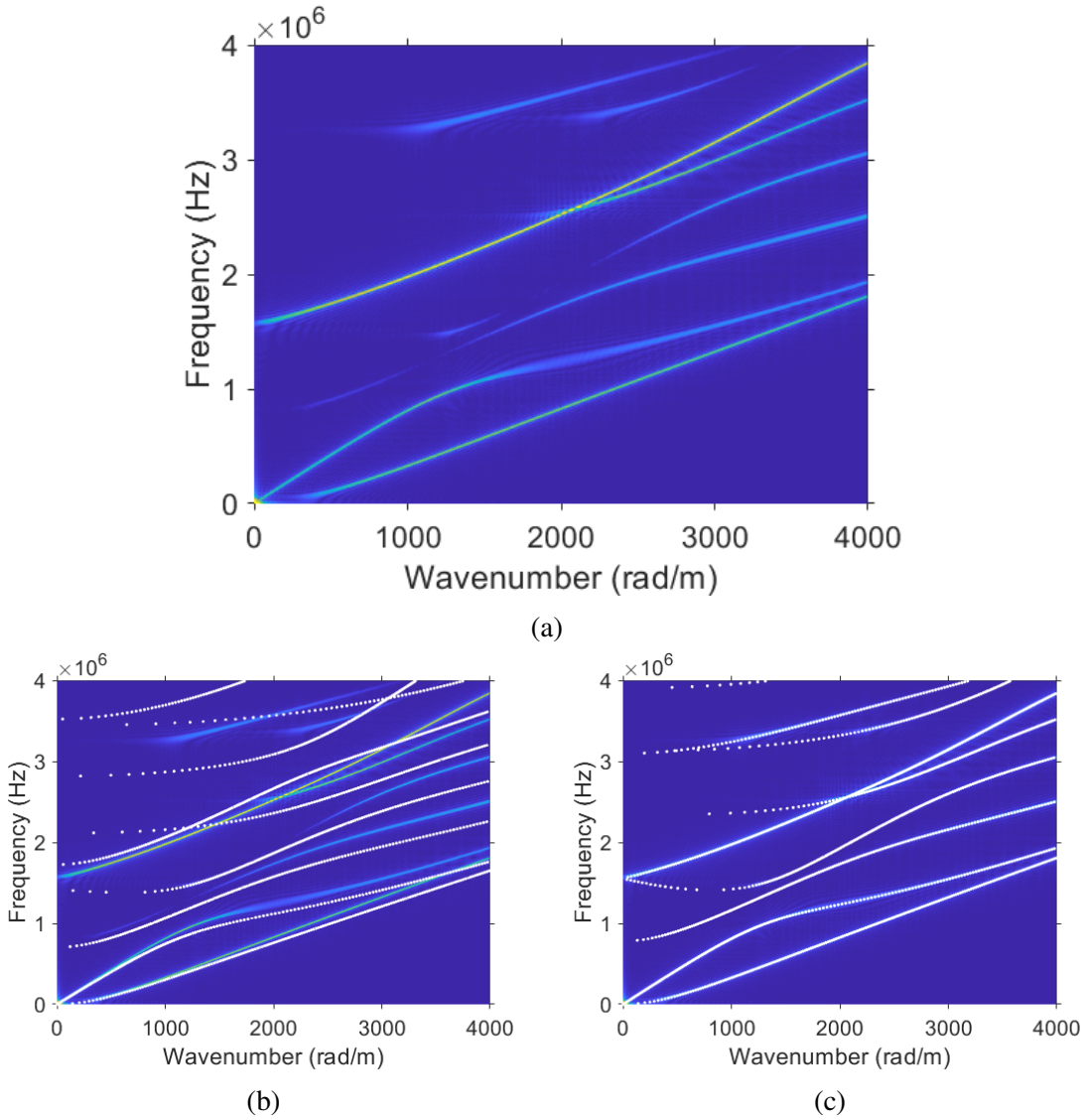

Figure 4.3: Dispersion maps for the aluminium plate generated using synthetic data (a) initial map, initial map superimposed with dispersion curves (white dots) calculated using (b) initial and (c) optimised elastic constants (Case 1 in Table 4.2 and Table 4.3), respectively.

Table 4.2: Cases used to test the performance of the optimisation algorithm to infer material properties of aluminium.

Case number	Number of modes	f_{max} MHz	k_{max} rad m^{-1}
1	8	4	4000
2	5	2	2000
3	2	0.8	2000

Table 4.3: Initial, optimised and reference material properties of aluminium. Density $\rho = 2700\,\mathrm{kg/m^3}$ is used in all cases considered.

Property	Material properties				
	Initial	Case 1	Case 2	Case 3	Reference
E (GPa)	60	69.984	69.977	69.974	70
ν	0.4	0.3296	0.3296	0.3269	0.33

Optimisation based on experimental data In the experimental work a steel plate of 4.98 mm thickness was used. More modes can be excited in a thicker plate for the same bandwidth available of up to $f = 1.43$ MHz (see Table 3.5). Figure 4.4 shows the measured dispersion maps of the steel plate for in-plane and out-of-plane components. In the case of the out-of-plane component (Figure 4.4b), more dispersion information is obtained when compared to the in-plane component (Figure 4.4a). A reason for the various intensities is that displacement amplitudes of modes at the plate's surface vary from mode to mode and change with the frequency. There are some modes which have predominant displacement in one direction and little displacement in the other, *e.g.*, the mode with the out-of-plane component only in the frequency range between 1.1 MHz – 1.4 MHz with wavenumbers between 100 rad m^{-1} – 700 rad m^{-1} (compare Figure 4.4b to Figure 4.4a). Moreover, the 3D LDV used to acquire the data is less sensitive to the in-plane than to the out-of-plane component.

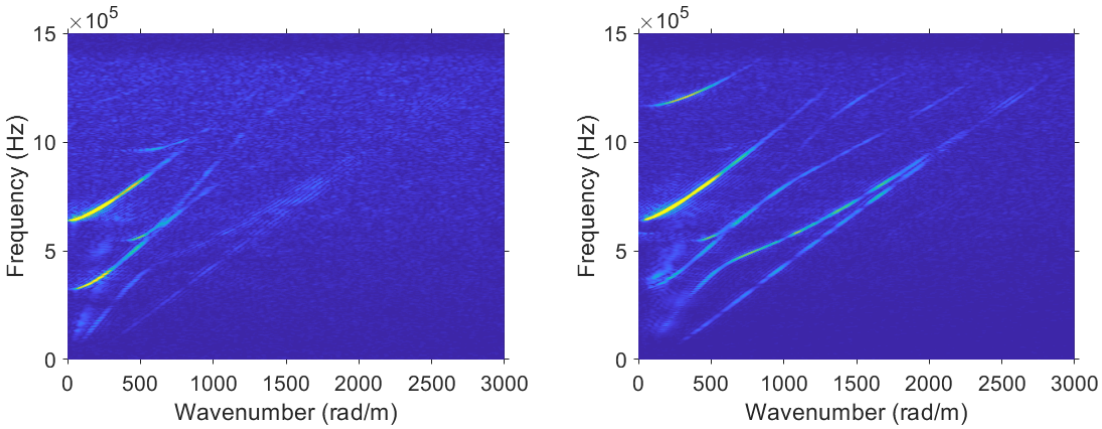

(a) in-plane component (b) out-of-plane component

Figure 4.4: Experimental dispersion maps for 4.98 mm steel plate.

For the optimisation of elastic constants, it is better to have as much dispersion information as possible. Therefore, both in-plane and out-of-plane components are first normalised separately and then summed to obtain one dispersion map shown in Figure 4.5. This allows to enhance the amplitude of some modes which have a predominant in-plane displacement, *i.e.*, the S1 mode around its cut-off frequency of 330 kHz. Furthermore, two different post-processing techniques are applied to this map to test if this may enhance the optimisation procedure.

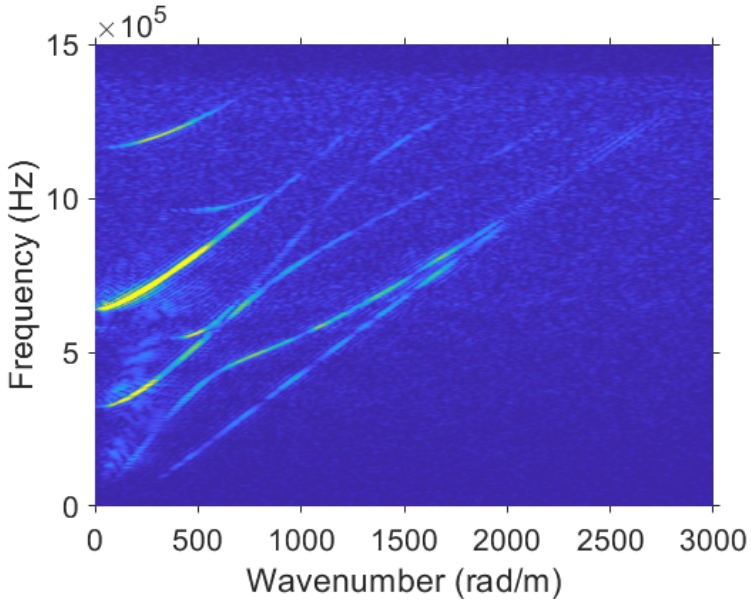

Figure 4.5: Combined experimental dispersion map for the 4.98 mm steel plate calculated using both components.

The first technique is a gamma correction which is simply defined by $U_{out} = U_{in}^{\gamma}$, where U_{in} and U_{out} are amplitude input and output of the dispersion map, respectively, and γ is a correction factor between 0-1. The result of the correction with $\gamma = 0.3$ is shown in Figure 4.6a. Due to the correction factor weaker modes become more pronounced. Bringing the modes to a similar amplitude level has an advantage that all modes have a comparable influence on the cost function optimised by the algorithm. One drawback of the gamma correction is that the noise level increases.

The second technique is thought to minimise the side lobes around the modes by applying a window function to the measured data prior to the Fourier transform, *i.e.*, the Hanning window. Note that the side lobes in the wavenumber domain come through the point-wise measurement which can be seen as a rectangular window function. Figure 4.6b presents the dispersion map after applying the Hanning window. This post-processing reduces the side lobes, however, at a cost of the broadening of the main lobe.

Based on these two post-processing techniques four cases are considered for the optimisation: data as it is, with both post-processing techniques applied simultaneously, and

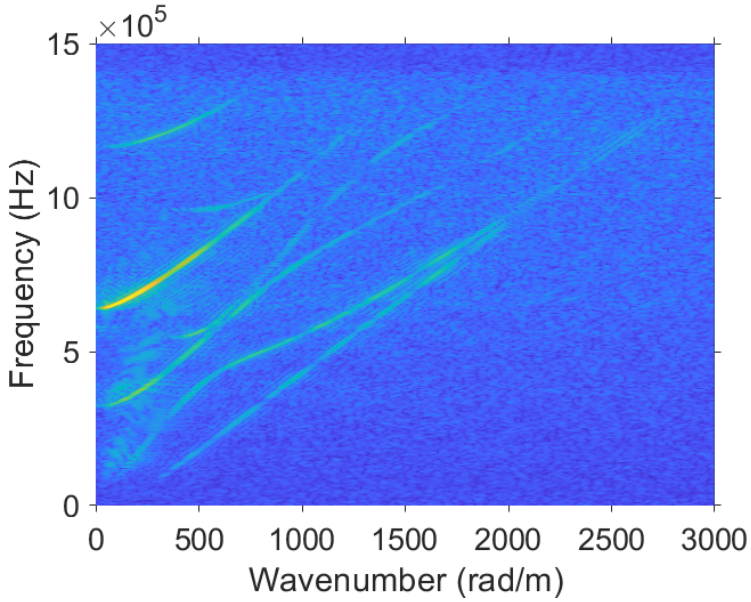

(a) without Hanning window

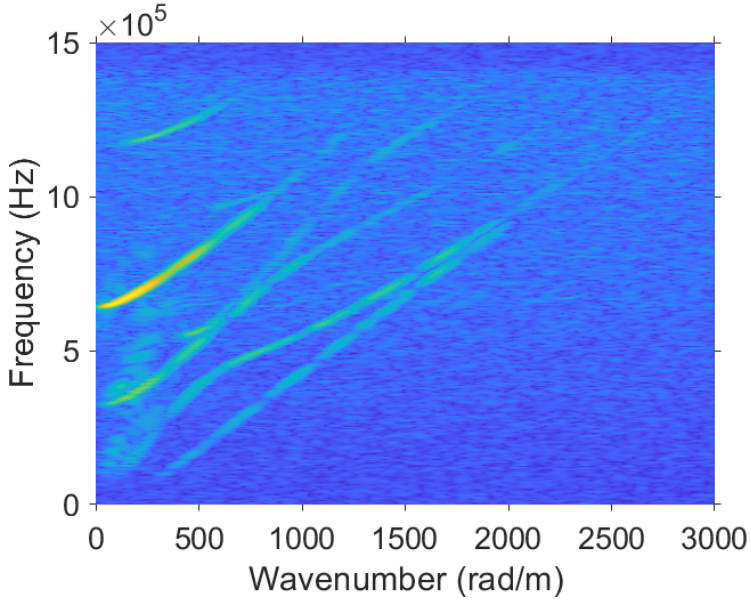

(b) with Hanning window

Figure 4.6: Experimental dispersion maps for the 4.98 mm steel plate with gamma correction.

with one or another technique used separately. Table 4.4 provides initial guess, literature values and summarises the optimisation results. For all cases considered, the optimisation algorithm converges to very similar values of E and ν ranging between 198.5 – 199.5 GPa and 0.289 – 0.291, respectively. The optimised values of E are in a very good agreement with the literature values, whereas ν differs for about 4 %. Note that steel from [181] has a different density than steel used in the experiments and thus the Young's modulus was scaled to the density of 7795 kg/m^3 to have comparable values.

Even though post-processing techniques do not influence the optimised values, it affects the computational costs. The gamma correction led to the faster convergence with 97 s and 115 s, where the longer computation time is in the case of the Hanning window used. The computational time without gamma correction were 168 s and 178 s for the data set without any post-processing and with the Hanning window applied, respectively. Thus, the gamma-corrected data set without Hanning window is used further to test the convergence of the optimisation algorithm.

Table 4.4: Initial and optimised elastic constants of steel with $\rho = 7795\,\mathrm{kg/m^3}$.

Elastic constant	**Initial guess**	**Optimised values**				**Literature values** [181]
		no correction, window	correction, window	no correction, no window	correction, no window	
E (GPa)	196	199.17	198.53	199.45	199.21	199
ν	0.28	0.289	0.291	0.289	0.289	0.278

According to [80], the accuracy of the optimisation results strongly depends on the initial guess. Therefore, the convergence of the algorithm to physically plausible values is tested using 50 randomly generated pairs of E and ν. The initial values for E and ν are in the range 117.6 – 274.4 GPa and 0.168 – 0.392, respectively, which are ±40 % of the initial values stated in Table 4.4.

Figure 4.7 presents the convergence results. For the optimised Young's modulus, 12 out of 50 values do not converge to physically plausible modulus (see pink dots with cost function equal to about 10 in Fig. 4.7a). These values lay in the lower ($<$ 150 GPa) and upper ($>$ 250 GPa) extremes of the initial Young's moduli. Most of the values converge to $E \approx 199$ GPa with the cost function value of 7 (see cyan dots in Fig. 4.7a). Based on the lower and upper bounds, it can be concluded that the Young's modulus can be still reconstructed even if the initial guess is within ±20 % from the actual value. Note that five values of the optimised E are overestimated as 208 GPa (see light blue dots Figure 4.7a for cost function values of around 8). These higher value of the cost function is due to the poor results with respect to the optimised Poisson's ratios, which range between 0.38 – 0.39 (confer light blue dots in Figure 4.7a and Figure 4.7b).

The optimised Poisson's ratios converge mostly to the values around 0.289 (see cyan dots

in Fig. 4.7b). In this figure some of the pink dots (the cost function value of 10) which can be found among expected values of ν are connected to the lower and upper extremes of E mentioned above. Except these, all other values converge to the Poisson's ratio of 0.289 allowing for a bigger variation of at least ±25 % between the initial guess and the effective ν. This behaviour may be attributed to the strong contribution of the mode 5 present in the measured dispersion curves in Figure 4.6a. This mode is quite sensitive to the change in the Poisson's ratio as can be seen on the example of the aluminium plate in Figure 4.2c.

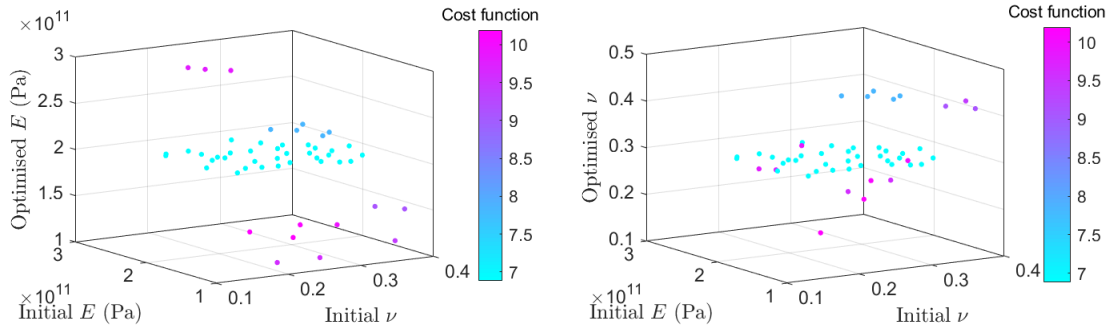

(a) E (b) ν

Figure 4.7: Convergence results of the optimisation algorithm based on 50 randomly generated pairs of E and ν.

4.1.2 Transversely isotropic material

In this subsection, the UD and cross-ply laminates with the lay-ups of $[0]_3$ and $[0/90]_3$ are considered, respectively. Following the definitions presented in subsection 3.1.2, a transversely isotropic material is defined by 5 independent elastic constants: D_{11}, $D_{12} = D_{13}$, $D_{22} = D_{33}$, $D_{55} = D_{66}$, whereas $D_{22} = D_{23} + 2D_{44}$ and the direction '1' is along the fibres. Note that the sensitivity of guided waves to D_{22} is not analysed in this work, because this constant is defined through D_{23} and D_{44}. The material properties used to create the synthetic data set and for the sensitivity analysis are called initial material properties in Table 3.3. To obtain the material properties for 90° ply, the elasticity matrix of 0° ply is rotated using Eq. (3.24). Note that for the experimental investigations, the laminates were made of the same prepreg as described in section 3.3.

Sensitivity analysis At first, the sensitivity analysis is performed on the UD laminate as described in section 3.6. The sensitivity to a 1 % change in the density and 5 elastic constants is analysed with respect to two wave propagation directions, along the fibres (0°) and perpendicular to the fibres (90°). The results are presented in Figure 4.8 and 4.9, respectively. The modes are less sensitive to the change in the constants than in the case of

the isotropic material. For instance, the maximum sensitivity of the modes to the change in the density for the UD laminate is in the order of 2000 Hz (Figure 4.8a), whereas the maximum sensitivity for the isotropic material is 15 000 Hz (Figure 4.2b). This is also valid for other elastic constants, which however cannot be directly compared to the Young's modulus and Poisson's ratio.

For the 0° direction, the sensitivity values of all constants are positive except for D_{12}, for which both positive and negative values exist. It is very interesting that the behaviour of the modes is totally different in a sense that only certain parts of the same mode can be sensitive to the change and that the sensitivity not necessarily increase with the frequency. For example, the mode 3 is sensitive to the variation of D_{55} at its cut-off frequency $f = 440\,\text{kHz}$ and a decrease in the sensitivity with the frequency is observed (Figure 4.8f).

Another interesting observation is connected with the mode repulsion (an explanation of the mode repulsion and its detailed analysis are presented in section 4.2). Only one mode repulsion region exists in the investigated frequency range which can be seen in Figure 4.8 around $f = 600\,\text{kHz}$ and $k = 400\,\text{rad}\,\text{m}^{-1}$. The modes in this region are very sensitive to the variation in all elastic constants (and density) with the exception of D_{55}. Moreover, the modes in the repulsion region demonstrate a non-uniform behaviour when it comes to D_{12}, the mode 2 has the negative sensitivity, whereas the mode 4 has the positive sensitivity (see Figure 4.8c). Furthermore, it can be seen in Figure 4.8f that the modes 1, 3, and 5 (the antisymmetric modes) are sensitive to D_{55} which is defined by the shear modulus G_{12}.

Regarding the 90° wave propagation direction presented in Figure 4.9, the elastic constants D_{11}, D_{12}, D_{55} do not have any influence on the modes. The elastic constant D_{44} has a linear behaviour as it is the case for the density - the sensitivity increases with the frequency - with the only difference in the positive sensitivity for the former and negative for the latter, see Figures 4.9e and 4.9a, respectively. As for the elastic constant D_{23}, the modes 4 and 5 have high sensitivities.

All in all, it can be concluded that the modes in the 0° wave propagation direction only are not enough to obtain the full elasticity matrix, since the elastic constants D_{23} (Fig. 4.8d) and D_{44} (Fig. 4.8e) affect the same mode parts. Note that these constants define D_{22} which contributes to the stiffness matrix for the 0° wave propagation direction. Thus, the additional information from the 90° wave propagation direction may be required because the modes in this direction are influenced by these two constants in a unique way. This hypothesis is tested on synthetic data later in this subsection.

Further, the sensitivity of modes to a 1 % change in the elastic constants is analysed for the cross-ply laminate. This laminate has the $[0/90]_3$ lay-up with each ply being made of the same prepreg as the UD laminate. Note that for such lay-up, the dispersion curves for the 0° and 90° wave propagation directions are equal. Figure 4.10 presents the sensitivity

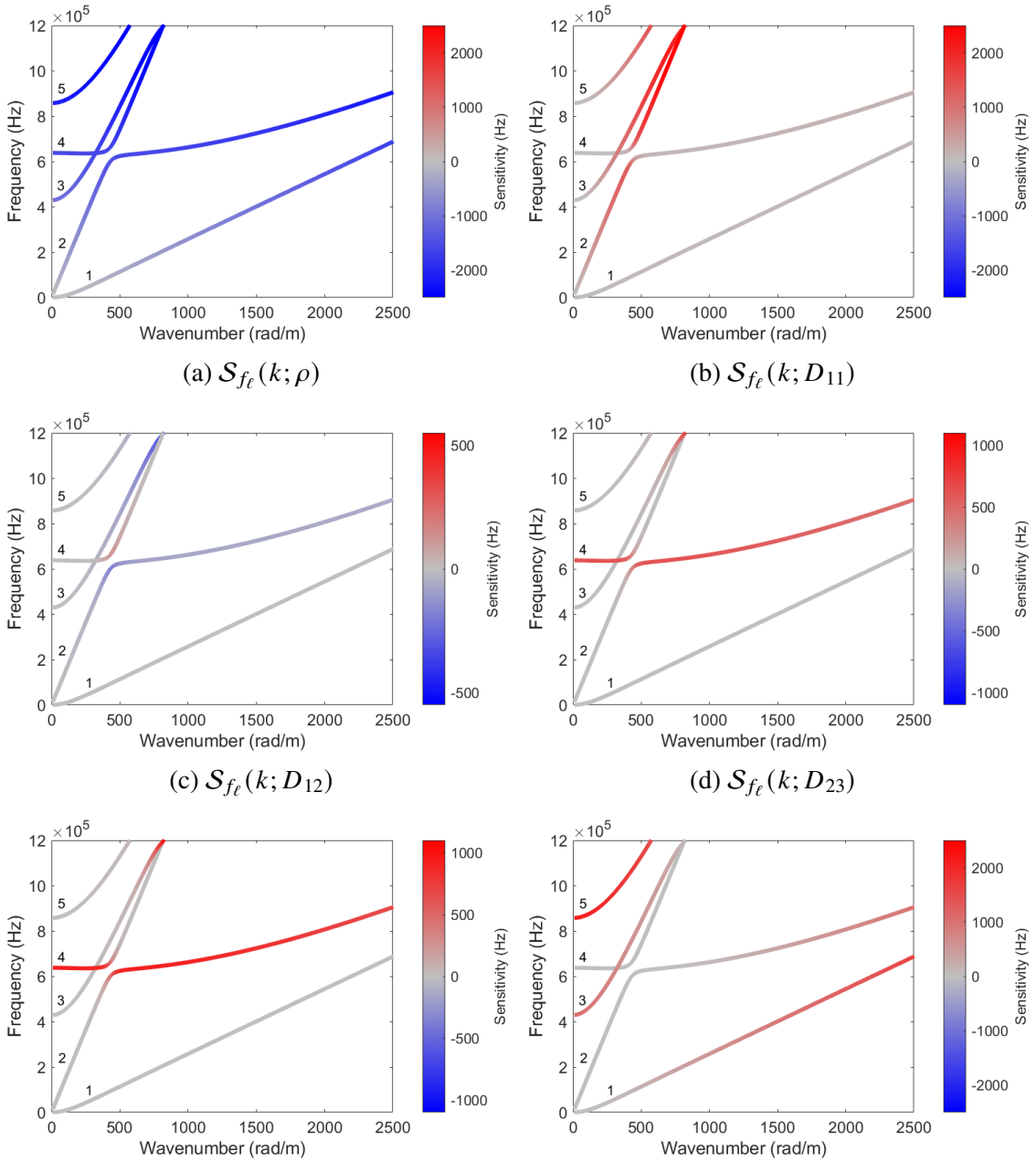

(a) $\mathcal{S}_{f_\ell}(k;\rho)$ (b) $\mathcal{S}_{f_\ell}(k;D_{11})$

(c) $\mathcal{S}_{f_\ell}(k;D_{12})$ (d) $\mathcal{S}_{f_\ell}(k;D_{23})$

(e) $\mathcal{S}_{f_\ell}(k;D_{44})$ (f) $\mathcal{S}_{f_\ell}(k;D_{55})$

Figure 4.8: Comparison of mode sensitivity $\mathcal{S}_{f_\ell}$ to a 1 % change in the density and elastic constants of the UD laminate for the 0° wave propagation direction.

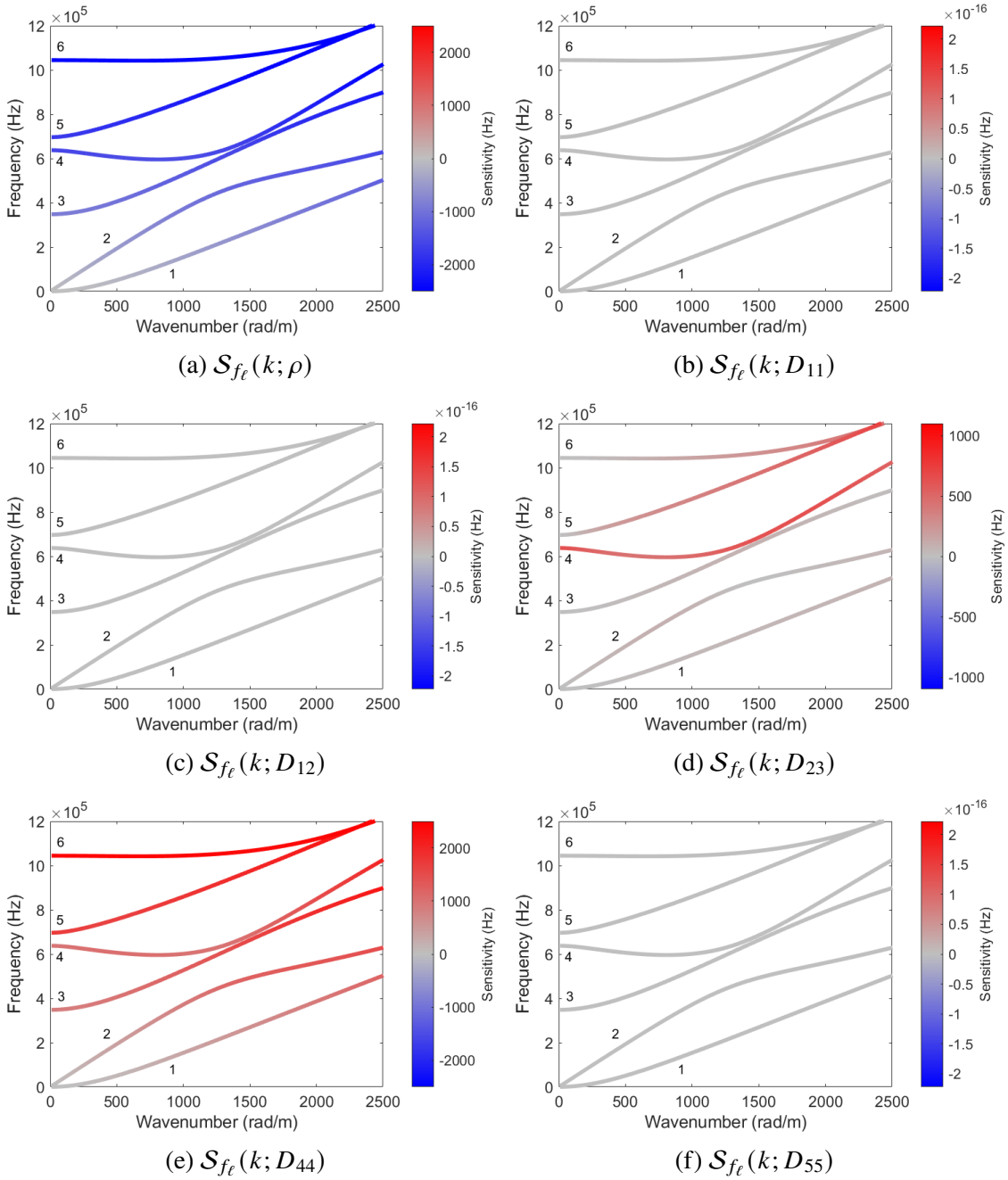

(a) $\mathcal{S}_{f_\ell}(k;\rho)$ (b) $\mathcal{S}_{f_\ell}(k;D_{11})$

(c) $\mathcal{S}_{f_\ell}(k;D_{12})$ (d) $\mathcal{S}_{f_\ell}(k;D_{23})$

(e) $\mathcal{S}_{f_\ell}(k;D_{44})$ (f) $\mathcal{S}_{f_\ell}(k;D_{55})$

Figure 4.9: Comparison of mode sensitivity $\mathcal{S}_{f_\ell}$ to a 1 % change in the density and elastic constants of the UD laminate for the 90° wave propagation direction.

results. The dispersion curves showing the sensitivity to the change in density are omitted because the behaviour is the same as for the UD laminate. In Fig. 4.10 the change in every constant leads to an unique behaviour of the modes. The sensitivities are in a similar range of about $f = 500\,\text{Hz}$ with the exception for D_{12} which has least influence on the modes with the lowest sensitivity of $f = \pm 50\,\text{Hz}$ but interestingly has both positive and negative sensitivities. The elastic constants D_{11} and D_{44} are dominating the behaviour of the modes as can be seen in Figure 4.10a for up to $k = 700\,\text{rad}\,\text{m}^{-1}$ and Figure 4.10d for the whole wavenumber range, respectively. It can be concluded that it should be possible to reconstruct full elasticity matrix of a composite material by optimising the elastic constants of one transversely isotropic ply based on the dispersion curves of the cross-ply laminate.

Optimisation based on synthetic data A 2.1 mm UD laminate with the material properties stated in Table 3.3 was modelled in the SBFEM to obtain the dispersion maps. Two simulations were done for the 0° (Fig. 4.11a) and 90° (Fig. 4.11b) wave propagation directions. The synthetic data is used as the reference to test the performance of the optimisation procedure.

It was shown in the previous subsection which dealt with the isotropic material that if not all modes are excited with similar amplitudes, the dispersion map can be enhanced using the gamma correction. This led to the faster convergence during the optimisation. Therefore, the simulated dispersion maps for the UD laminate are enhanced using $\gamma = 0.3$. Note that there is a high amplitude offset around 0, which is a modelling artefact. This artefact is removed by setting the first 10 frequencies to zero so that it does not influence the optimisation procedure. The resulting dispersion maps superimposed with the dispersion curves calculated using initial elastic constants from Table 4.5 are shown in Figure 4.11c (0°) and 4.11d (90°). The reference elastic constants were reduced by 10 % to obtain the initial guess for the optimisation. Note that the mismatch between dispersion maps and dispersion curves increases with frequency.

From the sensitivity analysis done previously, it became apparent that two wave propagation directions, 0° and 90°, may be needed to obtain all 5 elastic constants. Thus, two optimisations are run - one with the 0° direction only and the other with both directions used simultaneously. The results are shown in Figure 4.12 and the optimised material properties are listed in Table 4.5.

The dispersion curves calculated using optimised material properties match perfectly the simulated dispersion map for the 0° propagation direction irrespective of how many direction are used in the optimisation as can be seen in Fig. 4.12a (one direction) and Fig. 4.12c (two directions). However, there is a difference for the 90° direction - dispersion curves are slightly higher in frequency if only one direction is used (confer Fig. 4.12b and Fig. 4.12d).

Comparing the optimised values in Table 4.5, it becomes apparent that D_{11}, D_{44} and D_{55}

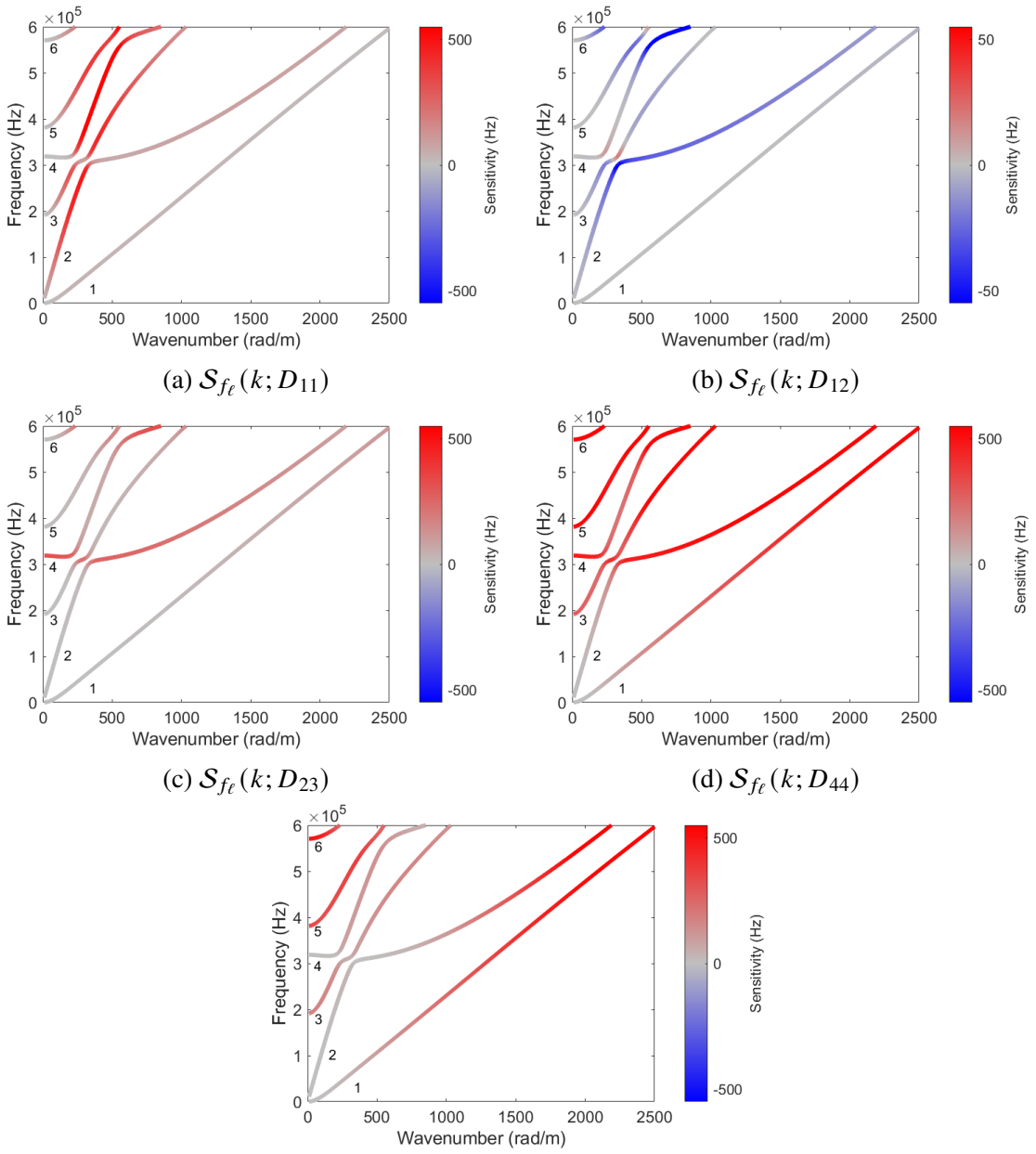

(a) $\mathcal{S}_{f_\ell}(k; D_{11})$ (b) $\mathcal{S}_{f_\ell}(k; D_{12})$

(c) $\mathcal{S}_{f_\ell}(k; D_{23})$ (d) $\mathcal{S}_{f_\ell}(k; D_{44})$

(e) $\mathcal{S}_{f_\ell}(k; D_{55})$

Figure 4.10: Comparison of mode sensitivity $\mathcal{S}_{f_\ell}$ to a 1 % change in the elastic constants of the cross-ply laminate for the 0° and 90° wave propagation directions.

Table 4.5: Initial, optimised and reference material properties of one CFRP ply with ρ = 1446 kg/m^3. The values in brackets stand for the accuracy of the optimisation result calculated in relation to the reference values.

Material	D_{11} GPa	D_{12} GPa	D_{23} GPa	D_{44} GPa	D_{55} GPa
Reference	123.1	3.9	4.2	3.1	4.7
Initial	110.79	3.51	3.78	2.79	4.23
Optimised, 0°	123.5 (99.7 %)	3.76 (96.4 %)	3.96 (94.3 %)	3.2 (96.9 %)	4.69 (99.8 %)
Optimised, 0°+90°	122.25 (99.3 %)	3.4 (87.2 %)	4.16 (99.1 %)	3.1 (100 %)	4.69 (99.8 %)

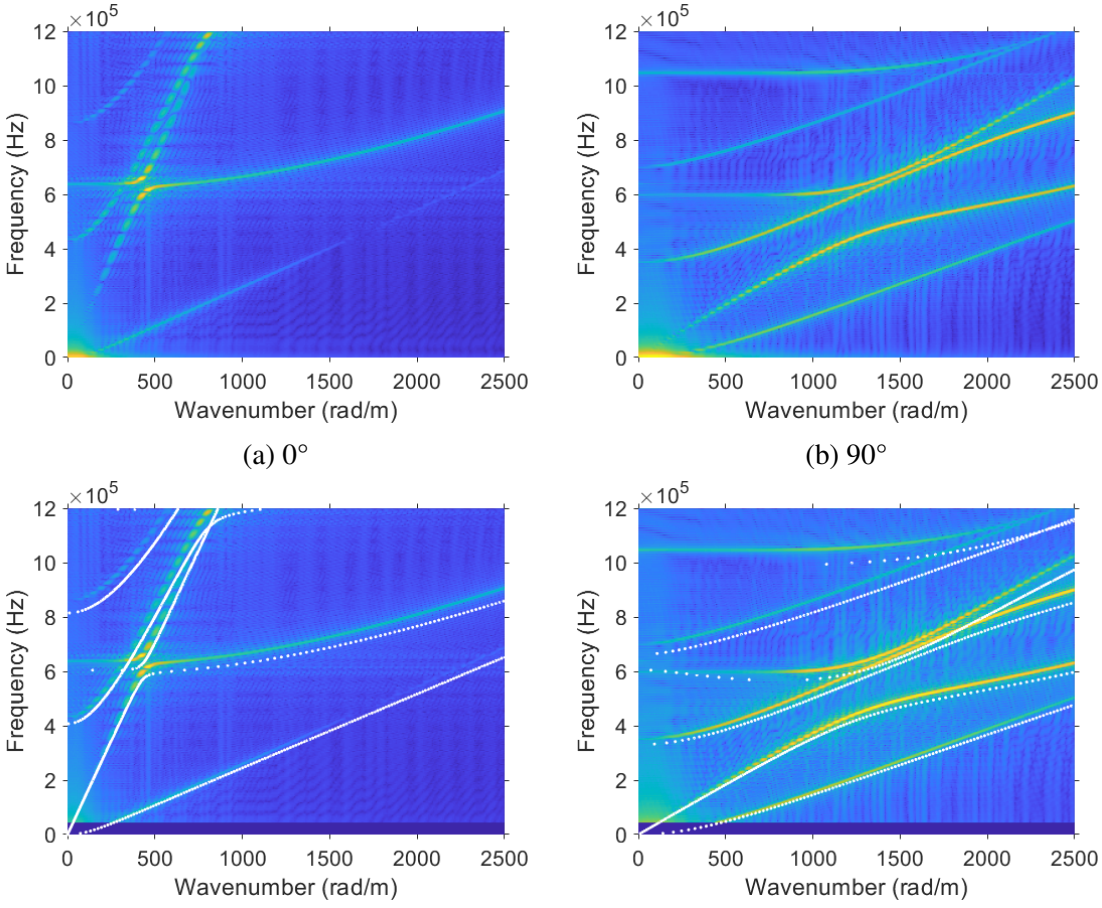

(a) 0°

(b) 90°

(c) 0° initial

(d) 90° initial

Figure 4.11: (a) and (b) simulated dispersion maps of the UD laminate (c) and (d) which are superimposed with the dispersion curves (white dots) calculated using initial elastic constants.

match the reference values closely. Note that D_{11} and D_{44} are slightly overestimated, if only one direction is used. The elastic constant D_{12} is reconstructed better with the difference of 4 % to the reference value, whereas the difference goes up to 13 %, if one and two directions are used, respectively. One could think that adding a second direction should not make a difference, since the modes in the 90° direction are not sensitive to D_{12} at all (see Figure 4.9c). However, this is not true because the optimisation of D_{12} is indirectly influenced by D_{23} and D_{44} which contribute strongly in the 90° direction as can be seen from their sensitivities in Fig. 4.9d and Fig. 4.9e, respectively. Thus, resulting in the shift of the second mode for D_{23} (Fig. 4.8d) and D_{44} (Fig. 4.8e) opposite to the shift of D_{12} (Fig. 4.8c). This shift dominates the optimisation in favour of D_{23} and D_{44} because there are many modes of high amplitudes present in the simulated dispersion map (see Fig. 4.11b). Finally, the elastic constant D_{23} is better reconstructed if two directions are used with the difference to the reference value of only 1 %, whereas the optimised value in the case of one direction is 6 % off the reference. This can be also attributed to the explanation given above. To avoid such influence of dominating modes and still be able to reconstruct the properties reliably, two optimisation runs can be done. One using the 0° direction for the reconstruction of D_{11}, D_{12} and D_{55} with D_{23} and D_{44} being fixed. After the former are optimised, the 90° direction can be used to characterise the remaining constants.

In terms of computational cost, the optimisation took 5 min and 10 min for one direction and two directions, respectively. It is longer than for the isotropic material mainly due to the higher number of layers used for the UD laminate which increases the computational time for one dispersion curve in the SBFEM. One and three layers were used to model the isotropic material and the UD laminate, respectively.

Optimisation based on experimental data Figure 4.13a and Figure 4.13b show the measured dispersion maps for the 2.1 mm UD laminate for 0° and 90° wave propagation directions, respectively. Both in-plane and out-of-plane components are used. In this figures, it can be seen that different modes are excited in the frequency range from 50 kHz to 1 MHz, see yellow and light blue ridges. The measured dispersion maps are superimposed with the dispersion curves (white dots) calculated using the initial material parameters which show a bigger discrepancy between experimental and numerical results than in the case of the isotropic material. This is because not all the elastic moduli required to obtain the full stiffness matrix are given by the manufacturer and need to be guessed. For both 0° and 90° wave propagation directions two modes are easily identifiable in the measured dispersion map in the lower frequency range up to 400 kHz and can be assigned to two modes in the dispersion curves. However, for the 0° wave propagation direction in the upper frequency range two modes lay in a close proximity to each other, see white dots in the frequency range 600 kHz – 1 MHz

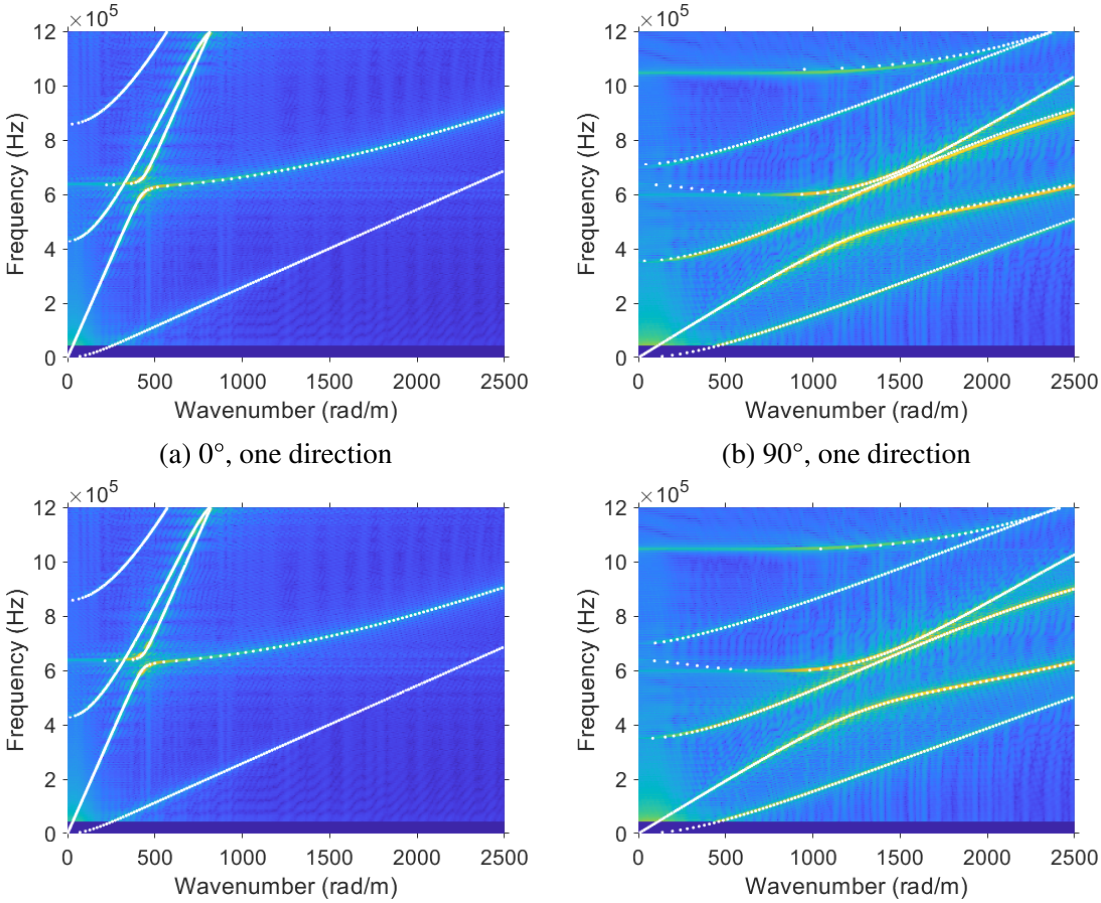

(a) 0°, one direction

(b) 90°, one direction

(c) 0°, two directions

(d) 90°, two directions

Figure 4.12: Simulated dispersion maps of the UD laminate superimposed with the dispersion curves (white dots) calculated using optimised elastic constants: (a) and (b) only one wave propagation direction is used in the optimisation; (b) and (c) two wave propagation directions are used simultaneously.

in Figure 4.13a, thus making correlation of the measured guided modes and theoretical dispersion curves harder in this range. Regarding the 90° wave propagation direction, only two modes are visible in the measured dispersion map shown in Figure 4.13b.

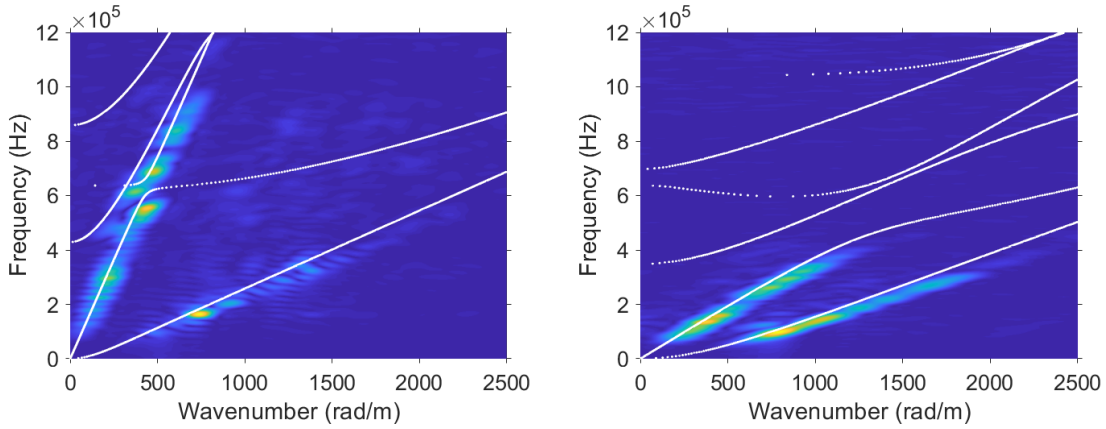

(a) 0° initial

(b) 90° initial

(c) 0° optimised

(d) 90° optimised

Figure 4.13: Measured dispersion maps of the UD laminate superimposed with the dispersion curves (white dots).

Based on the sensitivity study and the above results a use of both directions not necessarily improves the optimisation of elastic constants, because some of the modes may dominate the cost function. Nevertheless, since only a limited number of modes is excited with the current experimental set-up (see section 3.4) both directions, 0° and 90°, are used in the optimisation procedure. Figure 4.13c and Figure 4.13d show the dispersion maps superimposed with the dispersion curves after the optimisation procedure which was run for two wave propagation directions simultaneously. The best agreement between the experimental data and estimated guided modes is achieved in the frequency range up to 400 kHz for the 0° and 90° directions as it can be seen in Figures 4.13c and 4.13d, respectively. Moreover, the theoretical modes in the mode repulsion region match the measured modes well (see modes around $f = 600\,\text{kHz}$ and $k = 400\,\text{rad}\,\text{m}^{-1}$ in Figure 4.13c). This region was shown previously in Figure 4.8 to be

particularly sensitive to the variation in all elastic constants except D_{55}. As already mentioned, it is hard to judge about the agreement between experimental and theoretical results based on the modes in the frequency range starting from 650 kHz, because the measured modes are not clearly distinguishable (Figure 4.13c). The initial and optimised elastic moduli are listed in Table 4.6. The biggest variation is found for D_{44} for which the optimised value decreased by 26 % compared with the initial value. However, this is not surprising since the properties of composite materials strongly depend on the manufacturing procedure and thus may vary a lot. The elastic moduli D_{12} has the least variation of 7 % compared with the initial value which is possible due to lowest sensitivity of the modes to this constant (see Figures 4.8c and 4.9c).

Table 4.6: Initial and optimised material properties of one CFRP ply within different laminates with $\rho = 1446\,\mathrm{kg/m^3}$. The values in brackets show the deviation between initial and optimised values.

Material	D_{11} GPa	D_{12} GPa	D_{23} GPa	D_{44} GPa	D_{55} GPa
Initial	123.1	3.9	4.2	3.1	4.7
Optimised (UD)	98 (-20 %)	4.2 (+7 %)	4.8 (+13 %)	2.3 (-26 %)	3.8 (-19 %)
Optimised (Cross-ply)	102.2 (-17 %)	3.6 (-8 %)	5.6 (+25 %)	2.7 (-13 %)	3.4 (-28 %)

At next, the measurements were done on the cross-ply laminate and the results for the 0° and 90° wave propagation directions are presented in Figure 4.14c and 4.14d, respectively. For this cross-ply laminate, the dispersion curves are the same because the effective stiffness matrix does not change. However, the amplitudes of the excited modes are not the same, for instance, the mode 3 is better excited in the 0° direction, whereas the mode 4 in the 90° direction. This can be explained by the mode shapes which have different amplitudes depending on the stacking sequence, $[0/90]_3$ *vs.* $[90/0]_3$. Thus, it is beneficial to combine the information from both dispersion maps which is then to be used in the optimisation procedure.

Since both laminates are made of the same prepreg, it is expected that the optimised material properties of the UD laminate, when used for the calculation of the dispersion curves with the lay-up of the cross-ply laminate, should result in a perfect match to the measured dispersion maps of latter. Thus, the optimised elastic constants from the UD laminate is used to calculate the dispersion curves shown in Figure 4.14a and 4.14b. Both are matching well up to the frequency of 250 kHz and deviate from this frequency on. These deviations may be attributed to the variation of properties due to manufacturing as well as due to the optimisation procedure run on the limited number of experimental modes. Therefore, the optimisation is run again with the material properties optimised on the UD laminate used as the initial guess. After the optimisation, the measured modes match the theoretical dispersion curves very well (see Figures 4.14c and 4.14d). The optimised elastic constants

are listed in Table 4.6.

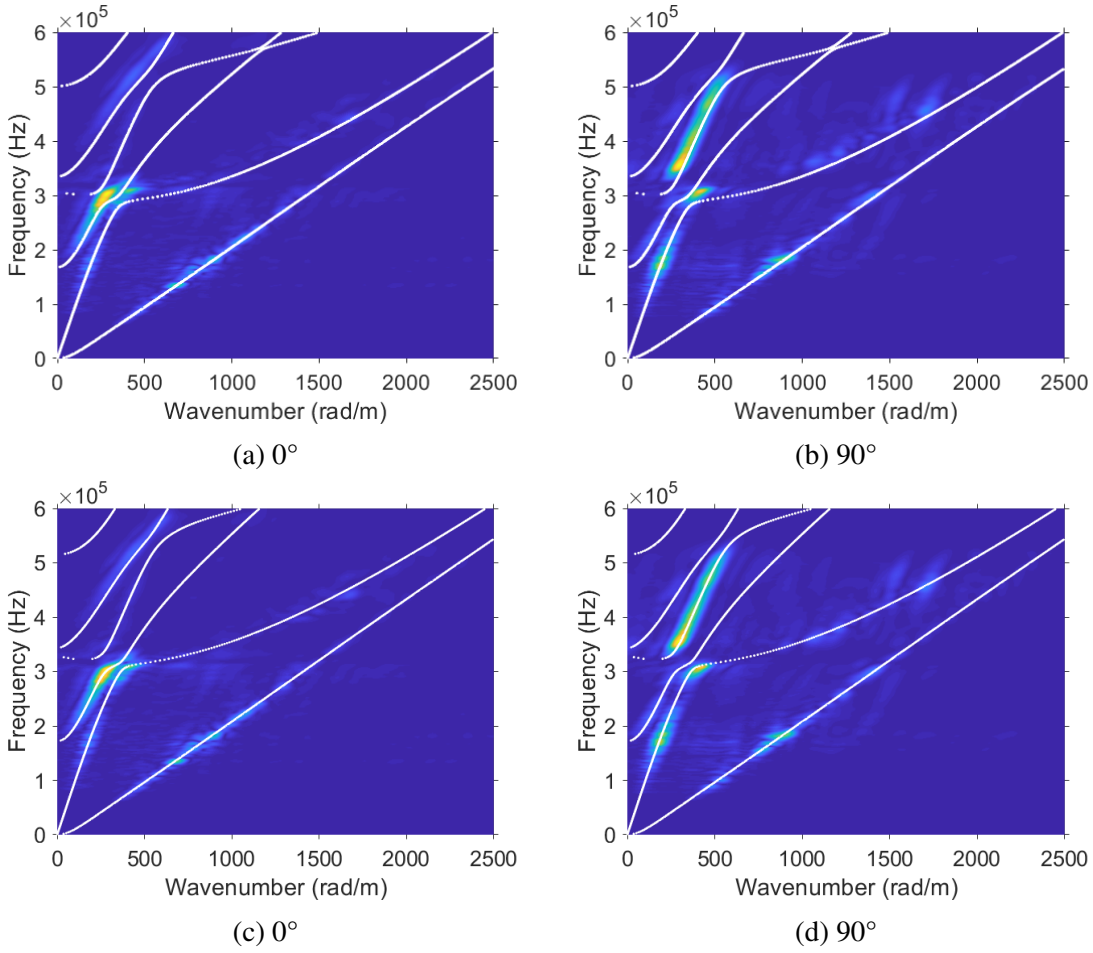

(a) 0° (b) 90°

(c) 0° (d) 90°

Figure 4.14: Measured dispersion maps of the cross-ply laminate superimposed with the dispersion curves (white dots) calculated using (a) and (b) material properties optimised on the UD laminate as an initial guess; (c) and (d) resulting material properties after the optimisation.

4.1.3 Summary and key messages

It has been shown that guided wave modes are sensitive to a change in elastic constants of isotropic and transversely isotropic materials. The sensitivity analysis carried out in this section allowed to analyse the relation between elastic constants and GW modes in detail. It has been found that the constants affect different modes or mode parts in a certain frequency-wavenumber region in a unique way.

In case of the isotropic material, a positive change in the Young's modulus resulted in a positive and linear shift of the modes with frequency. Whereas a positive change in the Poisson's ratio led to a non-uniform behaviour meaning that both positive and negative

movements of the modes are present. For both parameters, an increase in the sensitivity with the frequency has been observed.

For the transversely isotropic material, two wave propagation directions were analysed. For the wave propagation along the fibres (0°), all elastic constants influence GW modes showing both positive and negative sensitivities with a positive change of the constants. The elastic constants D_{23} and D_{44} affect the same modes, thus, these constants cannot be reconstructed reliably only from the 0° direction. Nevertheless, these constants can be reconstructed by adding one more direction, in this case, the wave propagation perpendicular to fibres (90°). Therefore, at least two wave propagation directions are required to be able to reconstruct all five elastic constants by means of GWs in the frequency range examined.

Regarding the 90° direction, only two elastic constants influence the modes. This is an expected behaviour, since only constants D_{23} and D_{44} contribute to the stiffness matrix in this direction as it was explained in subsection 3.1.3 and demonstrated in Figure 3.3. Note that in this figure, D_{22} is also contributing to the stiffness matrix, however, it is a dependent constant which is calculated using D_{23} and D_{44}, and therefore it was not optimised.

Another interesting observation is that the cut-off frequencies and mode repulsion regions are very sensitive to a change in some elastic constants. Especially, the mode repulsion regions observed for the UD and cross-ply laminates are influenced by all elastic constants except for D_{55}. All in all, it can be concluded from the sensitivity study that two lower order modes are not enough for the reliable reconstruction of elastic constants of transversely isotropic materials. Moreover, two wave propagation directions are needed, if the UD laminate is used in the optimisation.

Furthermore, the optimisation procedure from [56, 67] was modified in terms of the experimental set-up and forward model. Its performance was tested on the simulation data first before applying it on the experimental data. Considering the isotropic material, it was possible to excite eight modes in the simulation. Thus, the dependence between the accuracy of the reconstructed elastic constants and the number of modes used in the optimisation procedure could be analysed by reducing the number of modes consequently. In all cases, the optimisation algorithm converged to the reference values with the accuracy of 99.9 %. Even though, it has been shown that the lower order modes are least sensitive to elastic constants, especially to the Poisson's ratio, the optimisation on these modes worked reliably. This may be attributed to the definition of the sensitivity which estimates the mode's movement at one frequency and neither considers the relation of frequencies to each other nor the characteristic shape of the modes.

At next, the optimisation was run on the experimental data. In this case, seven modes were excited with one mode being especially strong. To compensate the difference in amplitudes which have the direct influence on the cost function and may affect the result, the

gamma correction was applied. Both original and gamma-corrected dispersion maps led to very similar values, however, in the latter case the algorithm converged faster. Thus, it is advantageous to use the gamma correction if modes are excited with different intensities to achieve faster convergence.

It is known that the accuracy of the optimisation results strongly depends on the initial guess [80], therefore, the algorithm was tested on randomly generated values distributed within ±40 % of the initial guess. The results showed that the Young's modulus and Poisson's ratio can be accurately recovered when the initial guess is within ±20 % and ±25 % of the actual values, respectively. Further, the transversely isotropic material was considered. The optimisation based on the simulated data showed that the dispersion map for the wave propagation along the fibres (0°) was enough to recover D_{11} and D_{55}, and D_{12} and D_{44} with the accuracy of at least 99.7 % and 96.4 %, respectively. The elastic constant D_{23} has the lowest accuracy of 94.2 % because the change of this constant influences the same modes as D_{44} but it is less sensitive. The former could be reconstructed with 99 % accuracy when two directions were used in the optimisation. However, this reduced the optimisation accuracy of D_{12} to 87.2 % which is attributed to the higher sensitivity of the modes in the 90° direction over D_{12} and D_{44} and thus their dominance in the optimisation procedure.

Regarding the experimental validation, the optimisation was carried out for two laminates - UD and cross-ply - made of the same prepreg. Since not all modes could be excited in the UD laminate in the frequency range investigated, it was harder to evaluate the performance of the optimisation algorithm on this example. Nevertheless, the dispersion curves after optimisation match the experimental results well. As for the cross-ply laminate, also two wave propagation directions were used but not because the dispersion curves differ between two (as it is the case for the UD laminate) but because different modes can be excited depending on the direction considered. Moreover, since many modes are excited and after the optimisation the dispersion curves fit the experimental data well which allows for a greater confidence in the optimised values.

Altogether, the measurement procedure and optimisation approach presented here allow to recover the elastic constants in a non-destructive way without a need for a special sample preparation. The optimisation of the elastic constants is especially relevant for composite materials which properties strongly vary from sample to sample. Moreover, based on this approach, the material ageing can be studied too. Further, the results presented here will allow to improve the numerical models which are necessary, *e.g.*, for the model-assisted quality assessment of SHM systems [182, 183].

Key messages The studies performed in this section were motivated by the questions stated in section 2.7, to which the following answers can be given.

- *Do elastic properties influence GW modes in a unique way?* The sensitivity results showed that the elastic properties of isotropic as well as anisotropic materials have a unique influence on GW modes. This allows to use GW for the characterisation of the elastic properties.

- *Do the fundamental modes contain enough information to infer the properties of isotropic and anisotropic materials reliably?* It has been shown that the fundamental modes are enough to characterise the isotropic material properties reliably. However, this is not the case for transversely isotropic materials. Therefore, higher order modes are required to be able to infer the elastic constants of such materials reliably.

- *Are there characteristic features of GW modes which are affected by a change in elastic properties the most?* The sensitivity study demonstrated that cut-off frequencies of some modes are especially sensitive to a change in the Poisson's ratio of isotropic materials and elastic constants D_{23}, D_{44} and D_{55} of transversely isotropic materials. Also, the mode repulsion regions appearing in the dispersion curves of UD and cross-ply laminates are very sensitive to a change in all elastic constants except for D_{55}. This is very advantageous, because the modes in the mode repulsion regions have high amplitudes and have shown to get excited easily.

- *Is the dispersion information from one wave propagation direction enough to reconstruct elastic constants of anisotropic materials?* Five to six modes exist in the investigated frequency range in the UD and cross-ply laminates, respectively. It was found that this number of modes should be sufficient to infer the elastic properties of transversely isotropic materials. In two cases considered, the UD and the cross-ply laminate, both wave propagation directions, 0° and 90° should be used, however due to different reasons. For the UD laminate, the reason is that dispersion curves differ, whereas for the cross-ply laminate, both directions have the same dispersion curves, but different modes are excited depending on the direction considered.

The material properties optimised in this section are used in the following sections to calculate the dispersion curves which are then compared to experimental results. In the next section, the repulsion of GW modes is analysed in detail on an example of coupled isotropic plates.

4.2 Guided waves mode repulsion

The results presented in this section originated from the joint work of Electrical Measurement Group (EMT) at Paderborn University and the Division of Acoustic and Electromagnetic

Methods at BAM. The experimental investigations were carried out by Sarah Johannesmann from EMT, whereas the numerical modelling was performed by the author of this thesis.

4.2.1 Effect of mode repulsion

Two sets of dispersion curves were calculated in the SBFEM to illustrate mode crossing and repulsion. In the first example, a 1 mm polycarbonate plate is considered, for which the dispersion curves are presented in Figure 4.15. Figure 4.15a demonstrates mode crossing of a A2-S2 mode pair at $f = 1.44$ MHz. This frequency range was chosen because here the first mode crossing appears. Note that mode crossings can be observed for other higher-order modes too when isotropic non-viscoelastic materials are considered. At this frequency the A2 and S2 modes have the same phase velocity, however, as it can be seen in Figure 4.15b, they have different group velocities. Thus, these two modes propagate independently without influencing each other and they are not coupled. Figure 4.16 compares the mode shapes of the A2 and S2 modes at two frequencies of 1.42 MHz and 1.51 MHz - before and after the mode crossing - respectively. The modes keep their behaviour after passing the mode crossing, only the displacement amplitude changes with the frequency, thus the A2 mode is not coupled with the S2 mode.

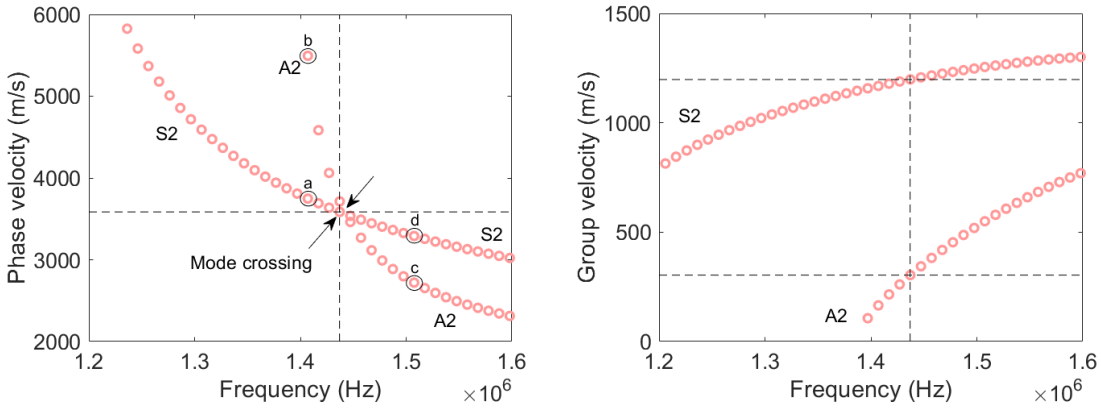

Figure 4.15: Illustration of mode crossing on the example of a A2-S2 mode pair. (a) Phase and (b) group velocity dispersion curves of a 1 mm polycarbonate plate.

In the second example, a 1 mm polycarbonate plate is firmly bonded to a 1 mm aluminium plate. Both materials are isotropic, and continuity of the displacement and stresses is considered at the polycarbonate-aluminium interface. Figure 4.17 present the dispersion curves of the coupled system. Figure 4.17a demonstrates mode repulsion of a A0-S0 mode pair at $f = 422$ kHz. This frequency range was chosen because here the first mode repulsion region appears. Note that as soon as a multi-layered structure is considered consisting of

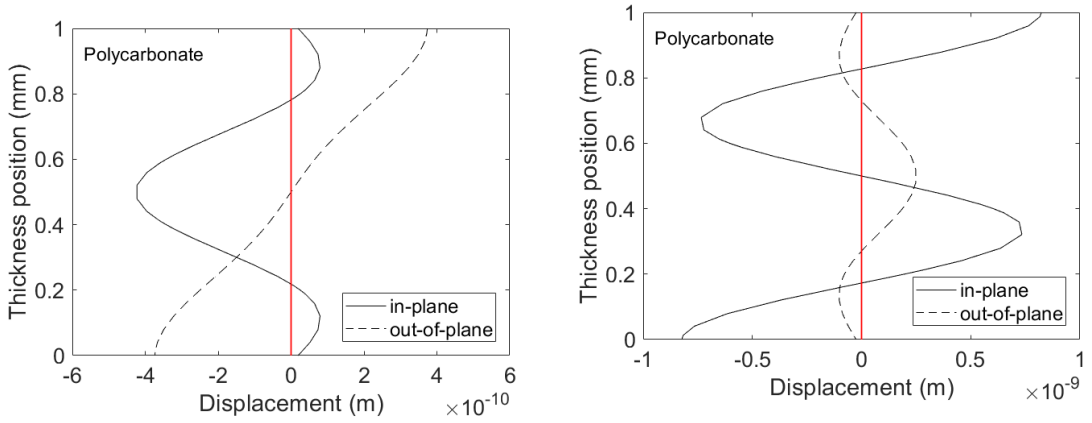

(a) S2 mode, 1.42 MHz

(b) A2 mode, 1.42 MHz

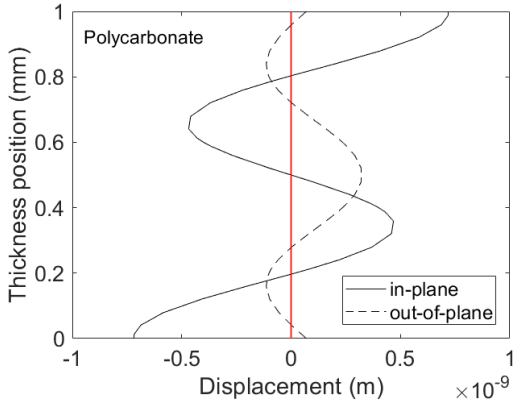

(c) A2 mode, 1.51 MHz

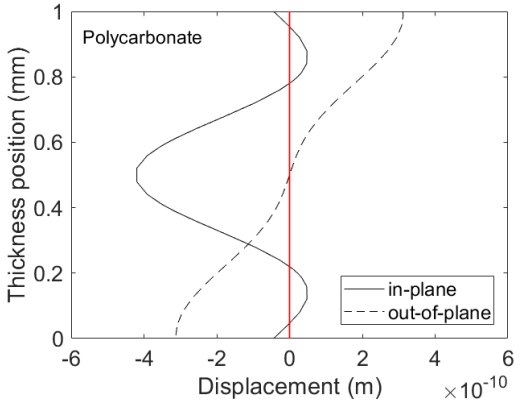

(d) S2 mode, 1.51 MHz

Figure 4.16: Mode shapes in the 1 mm polycarbonate plate for the points (a), (b), (c) and (d) marked in Figure 4.15, respectively.

materials with different acoustic properties, no mode crossings are observable in the phase velocity dispersion curves, but mode repulsions. At this frequency the A0 and S0 modes have different phase velocities, however, as it can be seen in Figure 4.17b, they have the same group velocity meaning that these two modes propagate with the same velocity and therefore they are considered as coupled modes. The modes are named A0 and S0 using the notations for single plates, however it must be noted that the modes in multi-layered structures which are not symmetric with respect to the mid-plane cannot be considered purely symmetric or anti-symmetric. After passing the mode repulsion region the modes exchanged their behaviour, as it can be seen by analysing the mode shapes in Figure 4.18. The A0 mode becomes S0* and the S0 mode becomes A0*. This figure compares the mode shapes of the A0 and S0 modes at two frequencies of 350 kHz and 500 kHz - before and after the mode repulsion - respectively. The modes exchange their behaviour after passing the mode repulsion region, however, for this region it happens only within the polycarbonate layer. The displacement of the A0 mode at $f = 350\,\text{kHz}$ (Fig. 4.18a) becomes almost zero at $f = 500\,\text{kHz}$ (Fig. 4.18c). The same applies to the S0 mode which has almost zero displacement amplitude at $f = 350\,\text{kHz}$ (Fig. 4.18b) and gets the behaviour of the A0 mode after passing the mode repulsion region (Fig. 4.18d).

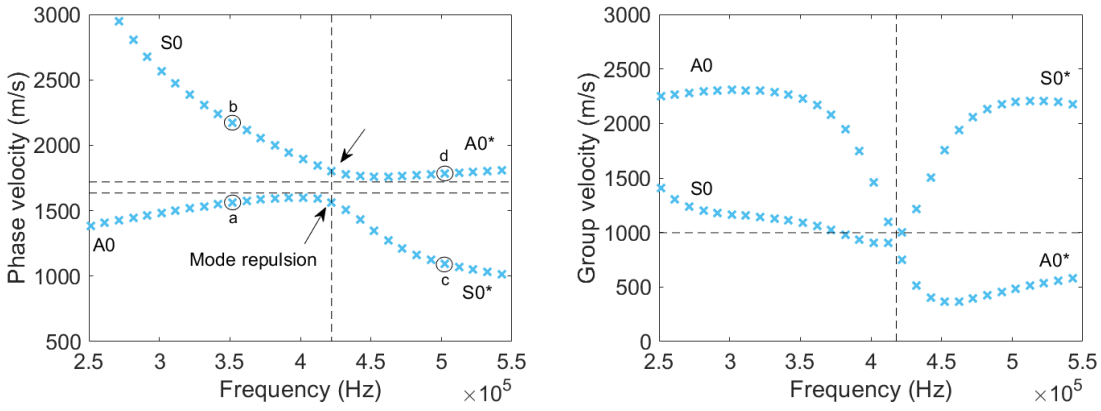

(a) (b)

Figure 4.17: Illustration of mode repulsion on the example of a A0-S0 mode pair. Dispersion curves of (a) phase and (b) group velocities of a 1 mm polycarbonate plate firmly bounded to a 1 mm aluminium plate.

4.2.2 Numerical analysis

Figure 4.19 shows dispersion curves calculated using the SBFEM for two single plates made of aluminium and polycarbonate, respectively. Each respective plate is of a 1 mm thickness and there is no connection between these two. In Figure 4.19 different number of GW modes appear in the aluminium plate compared to the polycarbonate plate for the same

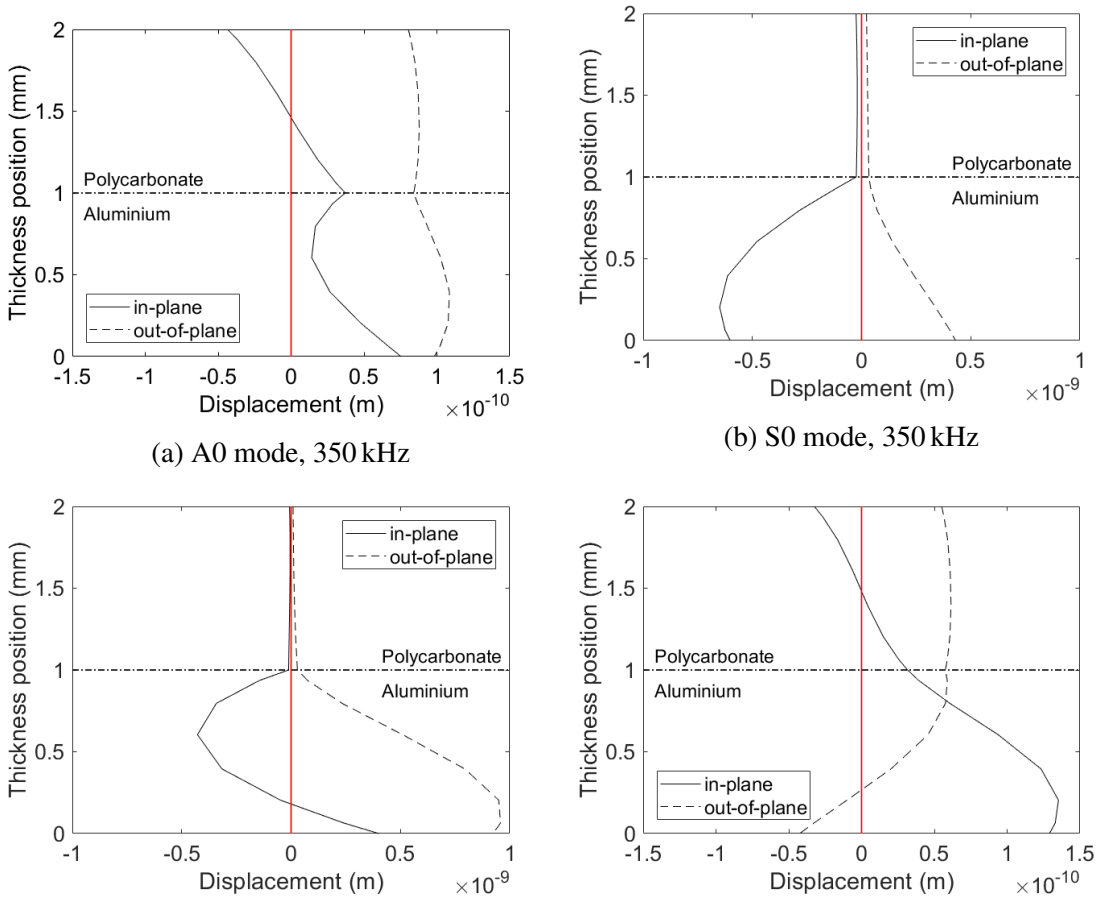

(a) A0 mode, 350 kHz

(b) S0 mode, 350 kHz

(c) S0* mode, 500 kHz

(d) A0* mode, 500 kHz

Figure 4.18: Mode shapes in the bi-layer plate made of a 1 mm polycarbonate plate firmly bounded to a 1 mm aluminium plate for the points (a), (b), (c) and (d) marked in Figure 4.17, respectively.

thickness. This is because of the different elastic properties of both materials. Aluminium as a stiffer (high impedance) material allows to excite the waves with higher velocities, whereas polycarbonate is a polymer, which is softer (low impedance) and therefore it has a smaller density and lower acoustic wave velocities compared to metals.

Now, if both plates considered are firmly bonded together, dispersion curves change and show the combined behaviour as it can be seen in Figure 4.20. The firm bonding means that the stresses and displacements are continuous across the polycarbonate-aluminium interface. It is remarkable that in the coupled system, wave modes do not cross at all but repulse only. Box 1 in Figure 4.20a indicates mode crossing of two modes in the single polycarbonate plate. This region corresponds to an illustration of mode crossing previously shown in Figure 4.15. It should be noted that other regions of mode crossing exist for the polycarbonate plate as well as for the aluminium plate at higher frequencies. Box 2 indicates one out of many mode repulsion regions appearing in the coupled system, this region was shown in detail in Figure 4.17. Moreover, it can be observed that mode repulsion regions appear at the vicinity of the intersection of uncoupled modes of the individual layers.

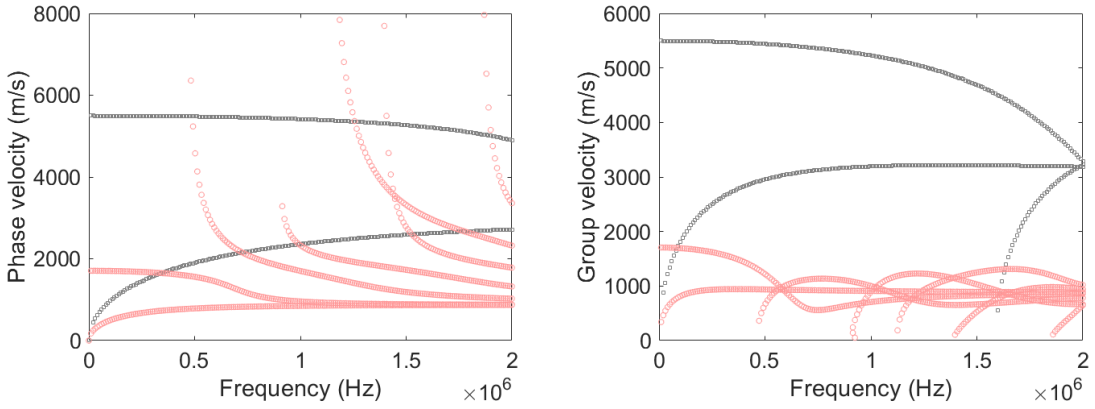

(a) (b)

Figure 4.19: Comparison of the dispersion curves of two single plates: (a) phase and (b) group velocities for a 1 mm aluminium plate (grey squares) and a 1 mm polycarbonate plate (pink circles).

Influence of the coupling strength on mode repulsion To demonstrate the effect of the coupling strength on the mode repulsion the following model is built. The model consists of three layers - 1 mm aluminium, 0.999 mm polycarbonate and an 1 µm interface layer. In this case, the half of the adhesive bond is considered, in which the aluminium plays a role of the substrate and the polycarbonate of the adhesive. This is done so that the influence of one interfacial layer on mode repulsion can be analysed. Note that a thin elastic layer is one of the ways to model different interfacial qualities of the adhesive bonds as it was described

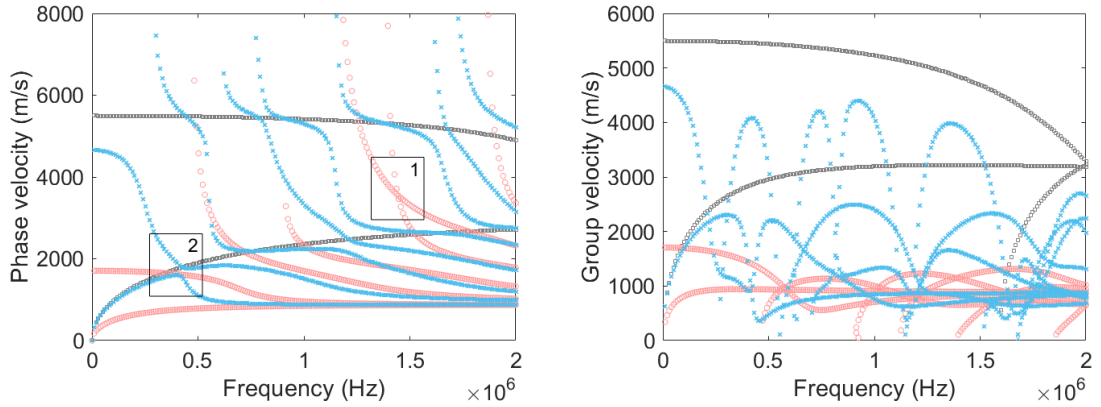

(a) (b)

Figure 4.20: Comparison of the dispersion curves of two single plates to a coupled system consisting of two bonded plates (blue crosses): (a) phase and (b) group velocities for a 1 mm aluminium plate (grey squares) firmly bonded to a 1 mm polycarbonate plate (pink circles). Boxes 1 and 2 indicate the regions of mode crossing and repulsion, respectively. Adapted from own results published in [142].

in section 2.3. Moreover, it was found that the interface thickness of 1 µm has no influence on the modes and mode repulsion in the chosen frequency range.

The elastic constants of the interface layer are varied to model different interfacial coupling states. Three cases were considered - strong, intermediate and weak coupling - corresponding to three states of interface degradation defined by Siryabe *et al.* [93]: nominal, intermediate and highly degraded states, respectively. The nominal state corresponds to the perfect bonding and thus the interface has 100 % of adhesive properties which is the polycarbonate in our case. Based on [93], the intermediate and highly degraded states correspond to an interface having 2 % and 1 % of the initial properties, respectively. The initial material properties of aluminium and polycarbonate (Table 3.4) were obtained by the EMT using the *Laser-induced broadband Lamb wave based measurement system*, which measurement principle was described in subsection 3.4.1. Note that the optimisation of the elastic constants was done for 3 elastic constants instead of 2 assuming that D_{11} is not equal to D_{22}. Table 4.7 list the material properties used for modelling of different interfacial coupling states.

Table 4.7: Properties used to model the interface degradation with $\rho = 1160\,\mathrm{kg/m^3}$.

Coupling state	D_{11} MPa	D_{12}=D_{21} MPa	D_{22} MPa	D_{44} MPa
Strong	5860	3810	5850	993
Intermediate	117.2	76.2	117	19.86
Weak	58.6	38.1	58.5	9.93

The modelling results for three coupling states considered as well as GW modes of the polycarbonate and aluminium plates having no connection between each other are presented

in Figure 4.21. In this figure two examples of mode repulsion regions are taken in the vicinity of polycarbonate modes intersecting with aluminium modes. Figure 4.21a demonstrates the intersection of the S0 mode of the polycarbonate plate with the A0 mode of the aluminium plate compared with the coupled modes of the multi-layered plate. Figure 4.21b shows the intersection of the S1 mode of the polycarbonate plate with the S0 mode of the aluminium plate compared with the coupled modes of the multi-layered plate. For the coupled system the real crossing of two modes (as it was demonstrated in Figure 4.15) is not permitted because one part of the system is in direct contact with another. This results in mode repulsion in regions where uncoupled modes of the individual layers (polycarbonate and aluminium) intersect (Fig. 4.21). In Figure 4.21a the gap in terms of the phase velocity between modes in the coupled system is wider when the coupling between the layers is weaker. The coupled modes are heading towards the intersection of uncoupled modes of the individual layers, namely the S0 mode of polycarbonate and A0 mode of aluminium. Whereas, for another mode repulsion region, shown in Figure 4.21b, the frequency gap between two modes in the mode repulsion region is narrower, the weaker the coupling between the layers is. The coupled modes in this frequency range are also heading towards the intersection of the uncoupled modes of the individual layers, the S1 mode of polycarbonate and S0 mode of aluminium. These results support the hypotheses stated in section 2.7 that the coupling between two layers influences coupled modes in a mode repulsion region.

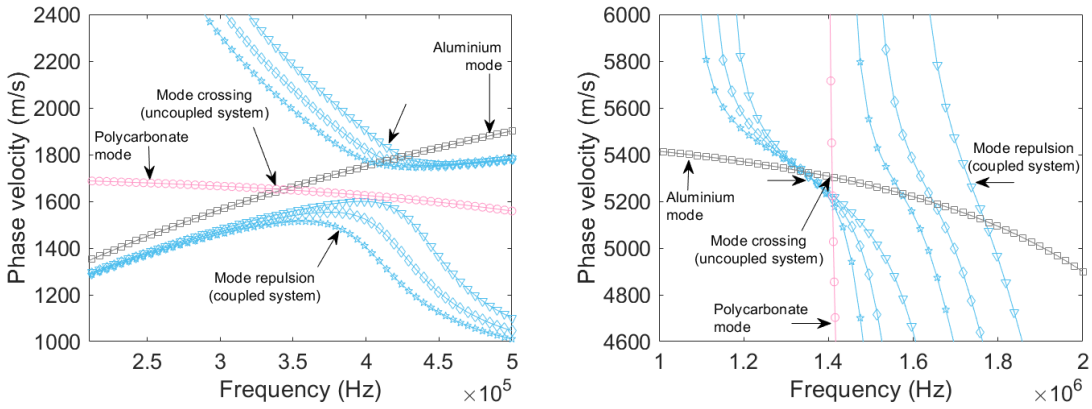

Figure 4.21: Influence of the interfacial coupling on mode repulsion shown together with the uncoupled modes of the individual layers - the 1 mm aluminium plate (grey squares) and 1 mm polycarbonate plate (pink circles). The multi-layered plate is represented by the 1 mm aluminium plate and 0.999 mm polycarbonate plate coupled by the 1 µm interface layer with strong (blue triangles), intermediate (blue diamonds) and weak (blue stars) coupling. Adapted from own results published in [142].

Figure 4.22 demonstrates the same mode repulsion region shown in Figure 4.21a, but now with the frequencies marked at the mode repulsion points. A mode repulsion point is

referred to as a point where the coupled modes have the same group velocity as it can be seen in Figure 4.22b. A decrease in the interfacial coupling shifts the mode repulsion point to a lower frequency. Also, the interfacial coupling influences the distance between the coupled modes in terms of the phase velocity. For this mode repulsion region, the width between the modes increases with the decreasing of the interfacial coupling as it is shown with the arrows in Figure 4.22a.

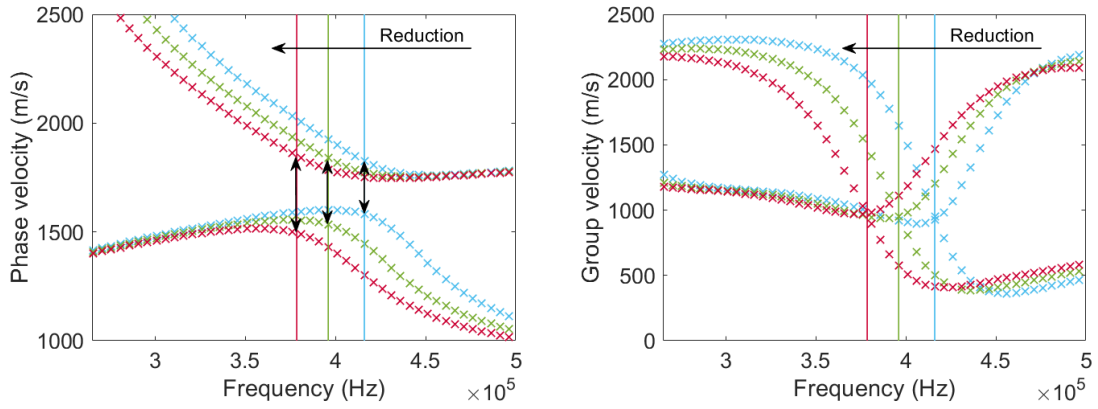

(a) (b)

Figure 4.22: Influence of the interfacial coupling on (a) phase and (b) group velocities considering a low frequency mode repulsion region on an example of the multi-layered plate consisting of the 1 mm aluminium plate and 0.999 mm polycarbonate plate coupled by the 1 µm interface layer. Blue, green and red crosses indicate strong, intermediate and weak coupling, respectively.

The mode repulsion region described previously layers in the low frequency range with phase velocities close to those of the A0 mode of aluminium and the S0 mode of polycarbonate. Therefore, two other regions were taken for further analysis, which are positioned at higher frequencies and their phase velocities are close to the S0 mode of the aluminium plate and higher order modes of the polycarbonate plate. These regions are presented in Figure 4.23. A common thing between these two regions and the one shown in Figure 4.22a is that the frequency of the mode repulsion point shifts to the lower values with the weaker coupling. The gap between the modes becomes wider with the weaker coupling for both high and low frequency mode repulsion regions shown in Figure 4.23a and Figure 4.22a, respectively. However, in the latter case this gap is in terms of the phase velocity and not the frequency. Regarding the second high frequency mode repulsion region shown in Figure 4.23b, the behaviour is opposite to other two examples - the frequency gap between two modes becomes narrower with the weaker coupling.

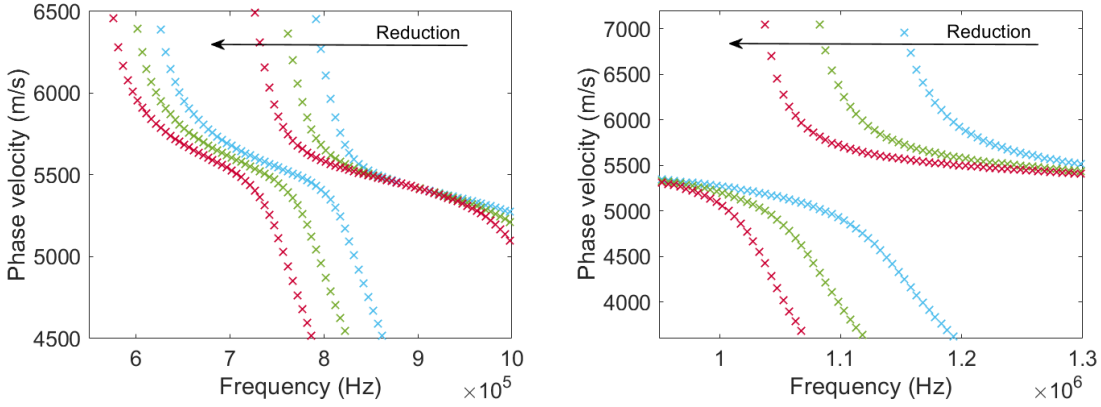

(a) (b)

Figure 4.23: Influence of the interfacial coupling on phase velocity dispersion curves considering two high frequency mode repulsion regions at (a) 0.55-1 MHz and (b) 0.95-1.3 MHz. The multi-layered plate consists of the 1 mm aluminium plate and 0.999 mm polycarbonate plate coupled by the 1 µm interface layer. Blue, green and red crosses mark strong, intermediate and weak coupling, respectively.

Sensitivity of mode repulsion to elastic moduli Further work has been done to investigate the sensitivity of mode repulsion regions to longitudinal and transverse stiffnesses. The aim is to be able to distinguish between these two stiffnesses and by that be able to correlate them with tensile and shear strengths, respectively. The same model is used as described previously with the interface layer considered to have the intermediate coupling state. The elastic moduli D_{22} and D_{44} of the interface layer are further reduced by 50 % each in two separate simulation runs to account for the variation in longitudinal and transverse stiffnesses, respectively.

The results shown in Figure 4.24 reveal that different mode repulsion regions are sensitive to changes in longitudinal and transverse stiffnesses. A region around 1.7 MHz is sensitive to the reduction of the longitudinal stiffness D_{22}, see the mode repulsion region indicated with black arrows in Fig. 4.24a. In the case of the transverse stiffness there is a region around 1.1 MHz sensitive to a change in the shear modulus D_{44}, see the mode repulsion region indicated with black arrows in Fig. 4.24b. Moreover, the vertical branches of the modes around repulsion regions change significantly, *i.e.*, modes 6 and 7 in Fig. 4.24a or modes 5 and 6 in Fig. 4.24b. Possibly these sensitivities of different modes to a change in stiffness can be attributed to wave modes having predominant symmetric or antisymmetric behaviour. According to Rose [13] symmetric modes can be considered as compressional waves and antisymmetric modes as flexural waves, thus one being more sensitive to a change in the Young's modulus (longitudinal stiffness) and another to the shear modulus (transverse stiffness). These changes can be obtained from separate mode repulsion regions and can be used for the development of a non-destructive characterisation method for the adhesive

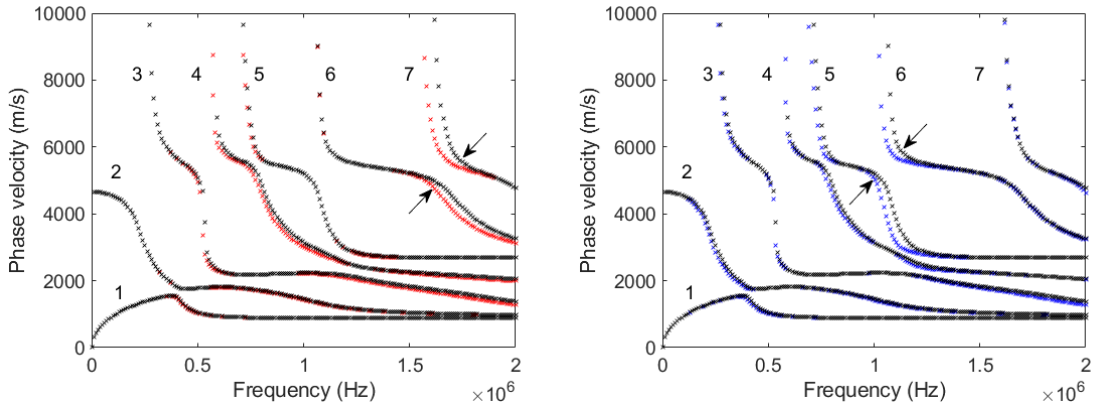

(a) (b)

Figure 4.24: Comparison of phase velocity dispersion curves of a coupled system (black crosses) to curves calculated with: (a) the reduced longitudinal stiffness (red crosses) and (b) reduced transverse stiffness (blue crosses) of the 1 µm interface layer between a 1 mm aluminium plate and a 0.999 mm polycarbonate plate. Black arrows indicate two different mode repulsion regions sensitive to the 50 % reduction of either (a) longitudinal D_{22} or (b) transverse D_{44} elastic moduli.

bonding strength. Additional investigations are necessary to show the correlation between longitudinal and transverse stiffnesses and tensile and shear strengths, respectively.

Sensitivity of mode repulsion to temperature For the investigation of the coupling strength only and its influence on the dispersion curves, other influences on the measurements must be avoided. One omnipresent influence is always temperature. Therefore, the influence of thermal expansion on the plate thickness has been investigated. The thickness changes were determined assuming a thermal expansion of $65 \times 10^{-6}\,\mathrm{K}^{-1}$ [184] for 3 mm thin polycarbonate for the temperature change of ±10 K. The resulting thickness change is ±19.5 µm. Assuming a thermal expansion for 1.5 mm thin aluminium of $23.1 \times 10^{-6}\,\mathrm{K}^{-1}$ [185] for the temperature change of ±10 K, the thickness change is ±3.5 µm. Considering these thickness changes caused by a temperature change of ±10 K and a frequency range of up to 2 MHz the dispersion diagrams lie almost exactly on each other (not shown here for brevity). Hence, the influence of a smaller temperature variation on the thickness change can be neglected.

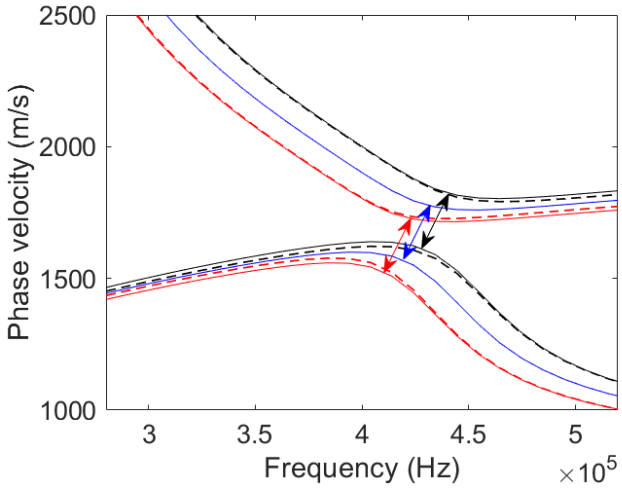

Figure 4.25: Temperature influence on a mode repulsion region modelled by changing the elastic moduli of two plates made of aluminium and polycarbonate with the thickness of 1 mm each. The blue line represents initial elastic moduli, the red line elastic moduli of both materials reduced by 5 %, the black line elastic moduli of both materials increased by 5 %, the red dashed line elastic moduli of polycarbonate and aluminium reduced by 5 % and 1 %, respectively, and the black dashed line elastic moduli of polycarbonate and aluminium increased by 5 % and 1 %, respectively.

A higher influence due to the temperature variation is expected on the elastic moduli [186]. The previous coupled model of the 1 mm aluminium plate firmly bonded with the 1 mm polycarbonate plate was used to investigate this influence on the mode repulsion regions. Two cases were considered: the first case is when elastic moduli of both materials change in the same way, modelled by a ±5 % change, the second case is when the elastic moduli of polycarbonate are influenced more (a ±5 % change) than the elastic moduli of aluminium (a ±1 % change). According to [187], the Young's modulus of aluminium decreases of about 3 % when the temperature increases from 20°C to 80°C. The results are shown in Figure 4.25. The same change in the elastic moduli of both materials leads to a shift of the modes, without influencing the width of the mode repulsion region. Different changes in elastic moduli of the materials lead to a similar shift of the modes with a small influence on the width of the mode repulsion region. Thus, it is necessary to control temperature during the measurements to avoid any influence on the measurement results.

4.2.3 Experimental results

The measurements are performed using a single 1.5 mm aluminium plate to identify the elastic constants of the material. The density and thickness are measured separately and stay constant during the optimisation procedure. The same is done for a 3 mm polycarbonate plate. Then both plates are glued together using a thin layer of epoxy resin. The resulting

multi-layered plate represents the coupled system having strong interfacial coupling which is then used for the investigation of mode repulsion. Weak coupling is realised using coupling gel (typically used in UT) between a 1.45 mm aluminium plate and a 3 mm polycarbonate plate with the material properties measured in advance. The results of measurements for weak and strong interfacial coupling are presented in the following.

Strong Coupling The measured dispersion map of the coupled system is overlapped with the simulation results for the single layers (white for aluminium, red for polycarbonate) in Figure 4.26a and with the simulation results for the coupled system in Figure 4.26b. It appears in Figure 4.26a that the excited modes of the coupled system trace the modes of the single aluminium plate, with the discontinuities at some of the regions where polycarbonate modes cross the aluminium modes. In turn, the measurement result compared to the calculated dispersion diagram of the coupled system in Figure 4.26b, reveals many mode repulsion regions at the positions of the measured discontinuities.

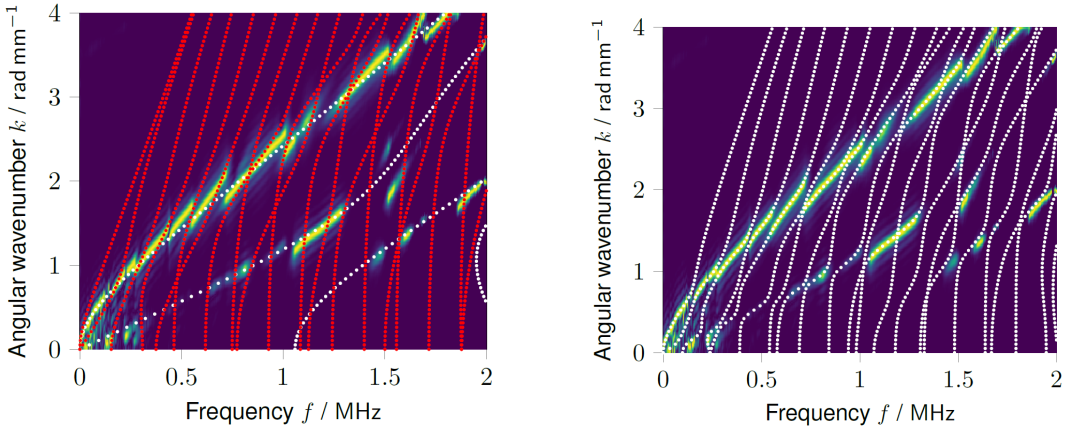

(a) (b)

Figure 4.26: Measurement results for strong coupling (colourful dispersion map) overlapped with simulation-based dispersion curves (shown with dots laid over the colourful dispersion map): (a) dispersion curves of the single layers (red for polycarbonate and white for aluminium), (b) dispersion curves of the coupled system. Adapted from own results published in [142].

Weak Coupling Next to a strong coupling through epoxy resin, a weak coupling between the aluminium and polycarbonate plates realised by a thin layer of coupling gel is considered. Figure 4.27 compares the weak coupling through coupling gel (Figure 4.27a) to the strong coupling using a thin layer of cured epoxy resin (Figure 4.27b). The dispersion maps look like those shown in the previous subsection - the modes of the coupled systems mainly trace the modes of the single aluminium layer, with the discontinuities representing mode repulsion

regions. It can be observed that the discontinuities in the ridges vary in their width depending on the coupling between the layers and mode repulsion region considered. For instance, a mode repulsion region becomes wider with the stronger coupling (cured epoxy resin in this case) at a frequency of $f \approx 0.8\,\text{MHz}$ and an angular wavenumber of $k \approx 2\,\text{rad}\,\text{mm}^{-1}$, confer the regions marked with the white ellipse for the weak (Figure 4.27a) and strong (Figure 4.27b) coupling. This is in accordance with the modelling results presented in Figure 4.21b, where the gap between the modes is wider if the coupling gets stronger. However, there are other mode repulsion regions which become narrower or completely disappear with the stronger coupling. For example, mode repulsion regions completely disappear in the frequency range around 1.25 MHz and angular wavenumbers around $1.5\,\text{rad}\,\text{mm}^{-1}$, confer the regions marked with the red ellipse for the weak (Figure 4.27a) and strong (Figure 4.27b) coupling. This is also in agreement with the modelling results presented in Figure 4.21a, where the gap between the modes becomes narrower if the coupling gets stronger. Overall, the modelling and experimental results strongly support the hypotheses that coupling strength between two layers influences the distance between two coupled modes in mode repulsion regions. It must be noted, that depending on the regions the distance may become wider or narrower with the stronger coupling.

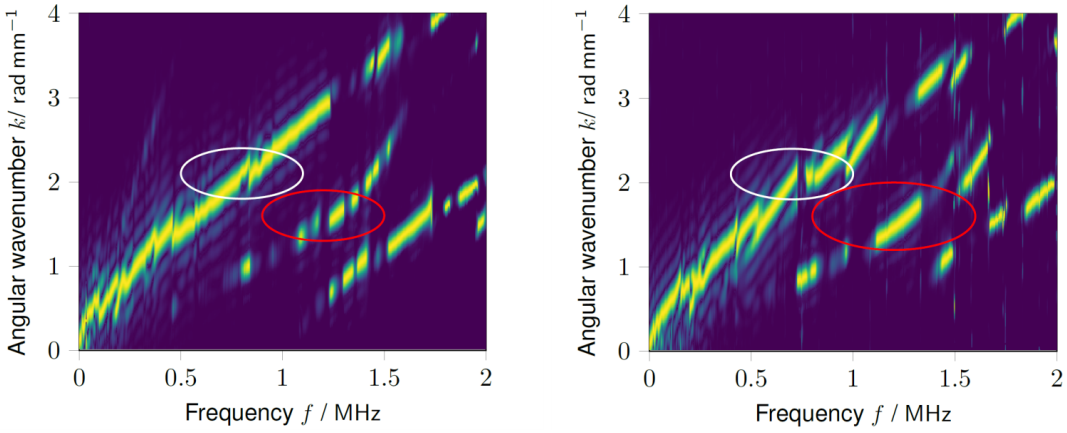

Figure 4.27: Comparison of measurement results for (a) weak and (b) strong coupling. Adapted from own results published in [142].

4.2.4 Summary and key messages

The effect of the mode repulsion occurring in the multi-layered structures was demonstrated and analysed on an example of two coupled isotropic plates having different acoustic properties. Note that this effect is not unique to the isotropic materials and can be also observed for anisotropic and viscoelastic materials or structures subjected to a disturbance, *e.g.*, a voltage

applied to piezoelectric plates or structures loaded with fluid. Therefore, mode repulsion can be considered as a mechanical or electromechanical coupling between two waves. Only the mechanical coupling was investigated in this thesis.

Since the mode repulsion appears in the multi-layered structures, it was assumed that this effect can be used as an indicator of a coupling strength between two or more layers. Consequently, it was shown both numerically and experimentally that two coupled modes in a mode repulsion region are influenced by a change in the coupling between two layers. It was observed that the distance between the coupled modes changes in terms of the phase velocity (wavenumber) or frequency. Moreover, a mode repulsion point shifts to lower frequencies with the weaker coupling between two plates. In addition, different mode repulsion regions sensitive to a change either in the longitudinal or transverse stiffnesses were identified numerically. This result may be used to estimate the tensile and shear strengths, respectively. Further investigations are necessary in which features of mode repulsion regions depending on the coupling state must be correlated to different adhesive bonding strengths.

Overall, the numerical modelling and experimental results strongly support the hypotheses that the coupling strength between two layers influences the distance between two coupled modes in a mode repulsion region. It must be noted that depending on the regions the distance may become wider or narrower with the stronger coupling. Therefore, mode repulsion could be very promising, *e.g.*, in the estimation of the coupling between layers to allow for the non-destructive characterisation of the adhesive bonding strength.

Key messages The outstanding questions posed in section 2.7 and the main finding of this section are as follows.

- *Could mode repulsion be a measure of coupling between two (or more) layers?* Numerical and experimental investigations have demonstrated that the mode repulsion appearing in the multi-layered structures can be used to distinguish between a strong and a weak coupling provided that the substrate properties are known in advance. It was found that the modes are coupled in areas of mode repulsion and change depending on the interfacial coupling state.

- *What features of mode repulsion can be used to characterise the coupling between layers?* The following features can serve as criteria for the characterisation of the coupling strength between two layers: the width with respect to the frequency and phase velocity (wavenumber), the position and the number of mode repulsion regions in a given bandwidth.

- *Are all mode repulsion regions influenced in the same way by a change in the coupling strength?* It was found that depending on the region the distance between modes

may become wider or narrower with the stronger coupling. Therefore, the numerical modelling is necessary to analyse such influence in advance to be able to draw right conclusions about the coupling state from the measurement results.

- *What other influences besides the coupling state affect the modes in a repulsion region?* The main limitation of the approach based on the mode repulsion is that the thickness, density, and elastic constants of constituent plates of the adhesive joint have to be known, since these affect the modes in a mode repulsion region. Only then, mode repulsion can be used to estimate the interfacial coupling state reliably. Moreover, guided waves are sensitive to temperature influence which also affects the modes in a mode repulsion region. Therefore, the temperature must be kept constant so that the coupling strength is the only influencing factor affecting the modes in a mode repulsion region.

- *Is it possible to distinguish between the longitudinal and transverse stiffnesses by means of mode repulsion?* The numerical investigations have shown that different mode repulsion regions exist which are sensitive to either the longitudinal or transverse stiffness. This has a potential for the characterisation of tensile and shear strengths by means of mode repulsion.

Next sections proceed with the numerical and experimental analysis of the mode-damage interaction in a multi-layered plate which combines both isotropic and anisotropic materials.

4.3 Guided waves in laminates

In the previous sections, the GW analysis was done for isotropic and anisotropic single layers, as well as for multi-layered plates combining multiple isotropic materials or the same anisotropic material. This section proceeds with the investigation on a multi-layered plate which combines both isotropic metal and anisotropic CFRP. This structure corresponds to the one of a composite pressure vessel with a load-sharing metal liner used for storing gases in aerospace and automotive industries. The main goal of this study is to demonstrate that the guided waves can detect and distinguish damage in any part of the structure, be it the aluminium liner or the CFRP overwrap. This will allow to bring the GW-based SHM for COPV further in their acceptance as a monitoring technique.

Dispersion curves for the aluminium-CFRP hybrid plate (Fig. 4.28) are presented in Figure 4.29. The modes chosen for the numerical modelling are marked with the circles. These points correspond to the centre excitation frequencies and were selected to have a minimal dispersion (minimal change of group velocity). Moreover, many cycles were used in the excitation signal to limit the frequency bandwidth which also allows to minimise the dispersion

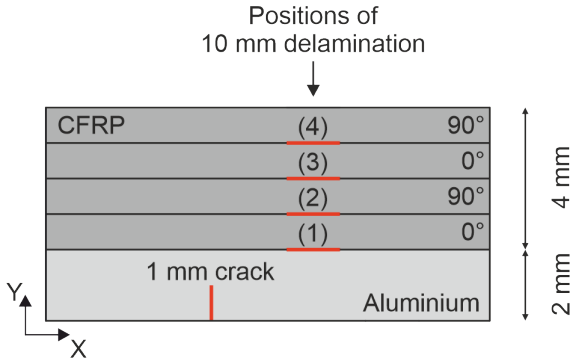

Figure 4.28: A sketch of the aluminium-CFRP composite plate used in the numerical investigations. The wave propagation is along the x-axis.

of modes. All values from the dispersion curves and number of cycles in a tone burst used for modelling are summarised in Table 4.8. The number of cycles was chosen based on the frequency, hence, the higher the frequency was, the more cycles were used in the pulse. This allows the frequency bandwidth to be kept narrow, which reduces the computational time in the SBFEM because the model is solved in the frequency domain.

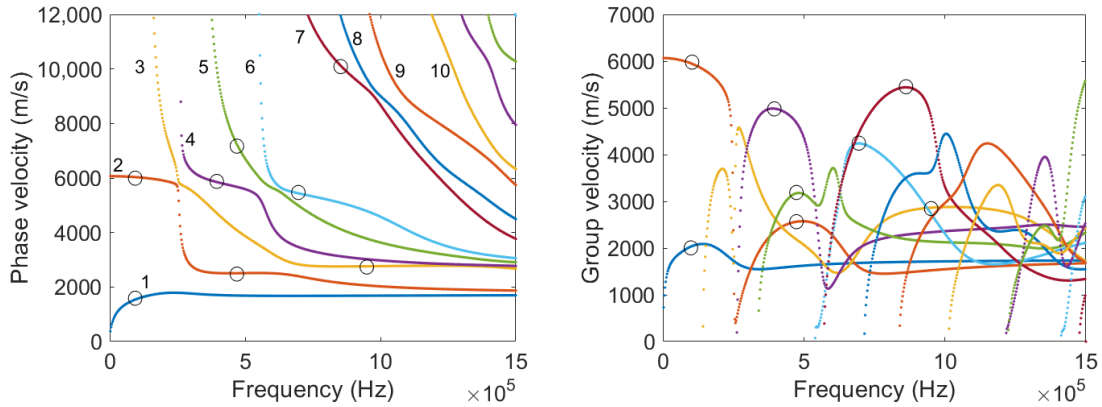

(a) (b)

Figure 4.29: Dispersion curves of (a) phase and (b) group velocities of the aluminium-CFRP plate. The circles mark modes, as chosen for numerical modelling. Own results published in [31].

4.3.1 Fundamental modes in a low frequency range

First, the simplest case of propagation of fundamental wave modes below cut-off frequencies of higher-order modes is considered. The details of the numerical model and excitation are described in section 3.2 ('Wave propagation in a composite laminate'). The mode 1 and mode 2 are excited at the centre excitation frequency of 100 kHz. The operation points are shown with circles in Figure 4.29 and details are listed in Table 4.8.

Table 4.8: Modes used for numerical modelling.

Mode	Frequency kHz	Group velocity $m\,s^{-1}$	Phase velocity $m\,s^{-1}$	Wavelength mm	Number of cycles
1	100	2033	1562	15.6	10
2	100	5953	6029	60.29	10
2	475	2565	2507	5.3	20
3	950	2864	2761	2.9	30
4	400	4981	5839	14.6	20
5	475	3175	7132	15	20
6	700	4238	5431	7.8	20
7	860	5440	10005	11.6	30

Taking a look at mode shapes of these two modes presented in Figure 4.30, it becomes apparent that the modes are not fully antisymmetric or symmetric. Note that antisymmetric or symmetric behaviour is typically considered with respect to the mid-plane of the plate. The shape of the mode 1 shown in Figure 4.30a resembles the behaviour of the A0 mode, which mode shape at the same frequency-thickness product in an aluminium plate can be seen in Figure 4.31a. The same applies to the mode shape of the mode 2 when compared to the S0 mode, confer Figure 4.30b and Figure 4.31b. Nevertheless, the general trend holds: the mode 1 (A0-like) has a dominant out-of-plane displacement component, whereas the mode 2 (S0-like) has a dominant in-plane component. Moreover, at the opposite surfaces of the plate, the in-plane and out-of-plane components are out-of-phase and in-phase for the mode 1, respectively, mimicking the behaviour of the A0 mode. For the mode 2 (S0-like) is the other way around.

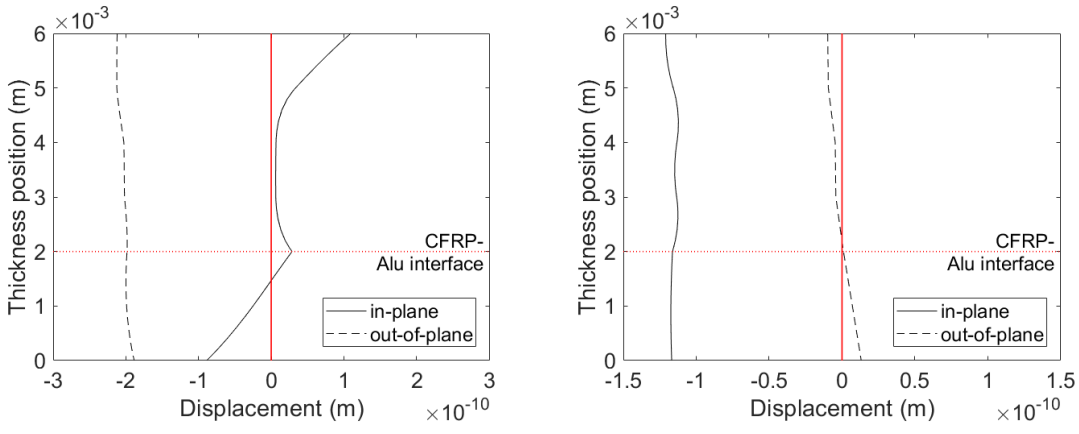

Figure 4.30: Mode shapes of the (a) mode 1 and (b) mode 2 at 100 kHz in the 6 mm aluminium-CFRP plate.

The mode shapes of the mode 1 and 2 were used as excitation and applied at the cross-section of the aluminium-CFRP composite plate as it is schematically shown in Figure 3.5. The signals obtained from the evaluation points, were analysed by means of the 2D FFT. All

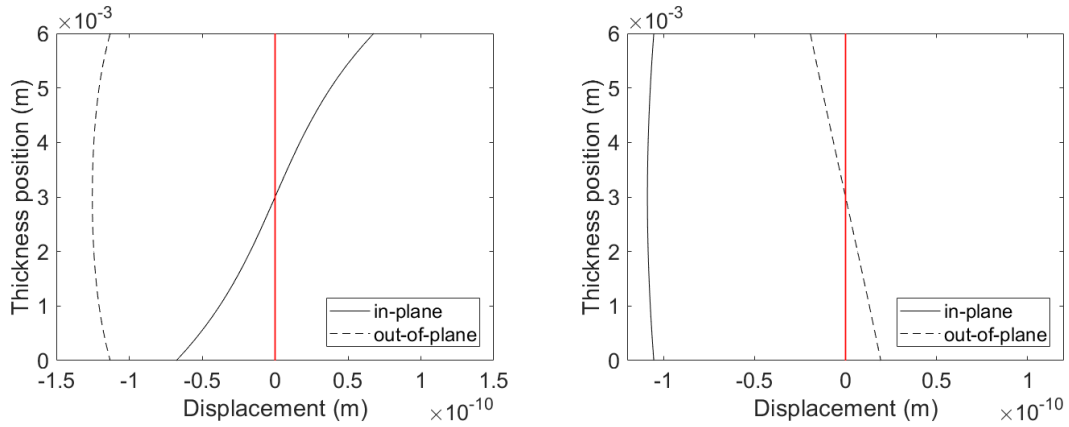

Figure 4.31: Mode shapes of the (a) A0 and (b) S0 modes at 100 kHz in a 6 mm aluminium plate.

examples shown hereinafter are for the evaluation points positioned at the aluminium-CFRP interface.

Figure 4.32 show the resulting frequency-wavenumber spectra which reveal different modes propagating in the plate and reflecting from the crack in the aluminium liner. To be able to identify different modes, the frequency-wavenumber spectra are superimposed with the dispersion curves. The negative and positive wavenumbers stand for the incident and reflected waves, respectively. To highlight the excited modes, the amplitude values around zero are coloured white. The amplitudes of the excited modes are analysed for both in-plane and out-of-plane components.

A crack in the aluminium part When using the mode shape of the mode 1, it is possible to excite the mode 1 only as can be seen at around $-400\,\mathrm{rad\,m^{-1}}$ in Figure 4.32a and Figure 4.32b for the in-plane and out-of-plane components, respectively. While the mode shape of the mode 2 leads to the excitation of both modes, to be seen at around $-400\,\mathrm{rad\,m^{-1}}$ and $-100\,\mathrm{rad\,m^{-1}}$ in Figure 4.32d, respectively. In the case of excitation of the mode 1 (A0-like), this mode reflects from the crack (Fig. 4.32b) and converts to the mode 2 (S0-like) [Fig. 4.32a]. Note that the in-plane component of the mode 1 (A0-like) is very small in comparison with its out-of-plane component at the aluminium-CFRP interface, which is in agreement with the mode shape shown in Figure 4.30a. In the case of the mode 2 excitation, this mode weakly reflects from the crack (Fig. 4.32c) and most of its energy converts to the mode 1 (A0-like) [Fig. 4.32d]. At the aluminium-CFRP interface the mode 2 (S0-like) has very small out-of-plane displacement compared with the in-plane displacement, which is also in agreement with the mode shape shown in Figure 4.30b.

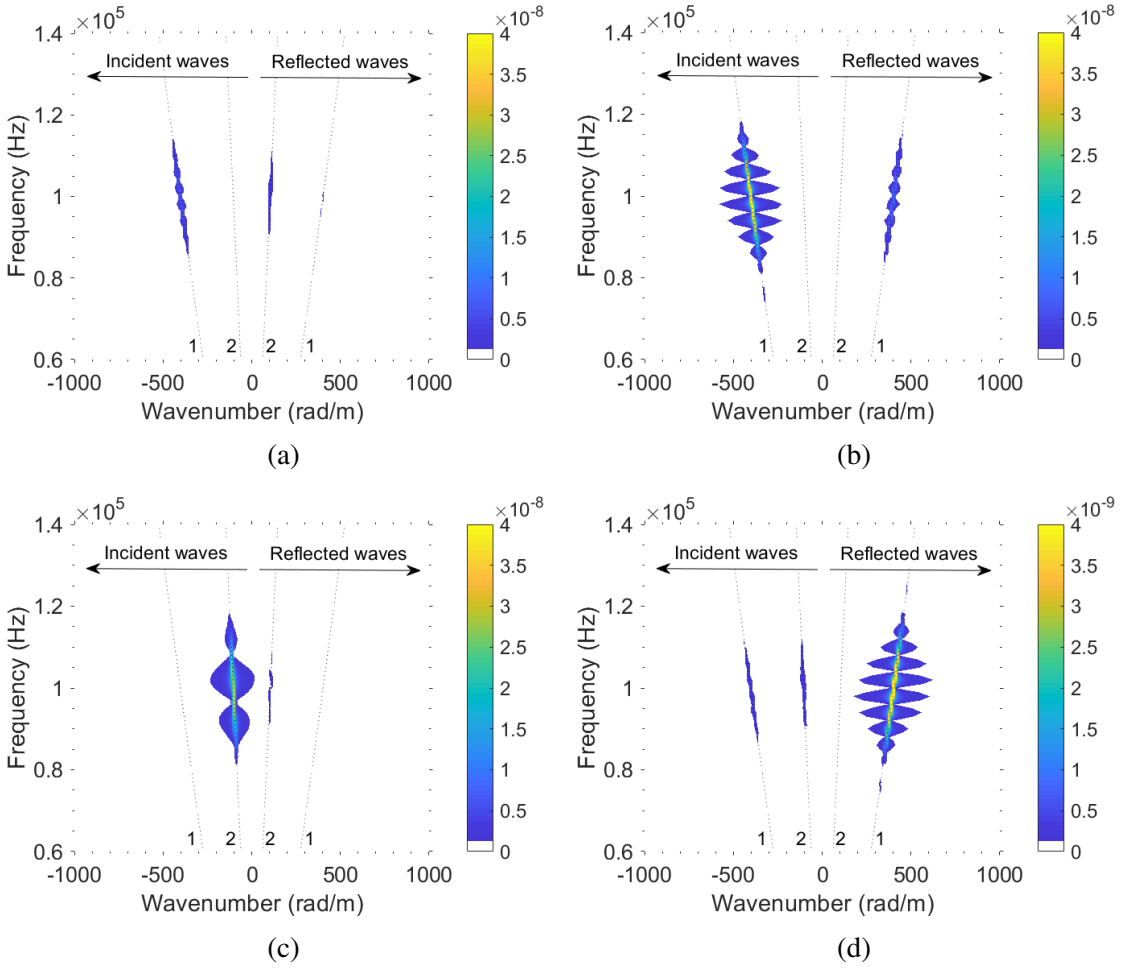

Figure 4.32: Interaction with the crack in the aluminium part of the hybrid plate. Frequency-wavenumber spectra of incident and reflected modes (a) for in-plane and (b) out-of-plane components while exciting the mode 1 (A0-like) at 100 kHz, (c) for in-plane and (d) out-of-plane components while exciting the mode 2 (S0-like) at 100 kHz.

A delamination in the CFRP part Four delamination positions were modelled as shown in Figure 4.28 and the case for the delamination at position (2) is presented in Figure 4.33. Nothing has changed from the excitation point of view from the previous case, thus the mode 1 is purely excited, whereas the excitation using the mode shape of the mode 2 leads to the excitation of both modes, confer Figure 4.32 and Figure 4.33. In the case of the excitation of the mode 1 (A0-like), this mode reflects from the delamination, to be seen for both in-plane and out-of-plane components in Fig. 4.33a and 4.33b, respectively. Also, as it was the case for the crack, there is a small amplitude at around 100 rad m^{-1} showing the conversion to the mode 2 (S0-like). This can be seen only for the in-plane component in Figure 4.33a. In the case of the excitation of the mode 2 (S0-like), this mode does not reflect from the delamination at position (2) (no amplitude is observed in Fig. 4.33c and 4.33d at $k = 100$ rad m^{-1}) and most of its energy converts to the mode 1 (A0-like), see the amplitudes at around $k = 400$ rad m^{-1} in Fig. 4.33d.

The modelling results are summarised in Table 4.9. For the first case, the excitation of the mode 1 (A0-like) leads to both its reflection from modelled damage and conversion to the mode 2 (S0-like) for both the crack and delamination, later being modelled for different positions. For the second case, the mode 2 is excited but it reflects only from the delamination placed at Position (4). Such behaviour of the S0 mode was described by Guo and Cawley [126] and is associated with the presence of the shear stress at the interface. When there is no shear stress across the interface, delamination does not affect the wave propagation, thus there is no reflection of the mode. However, this behaviour could not be observed in this work. The shear stress is not zero (not shown for brevity) at the interfaces at the positions (1)-(3). Moreover, no correlation between the power (energy) flux and damage detection could be found. Nevertheless, an indirect interaction of the mode 2 with damage can be observed, meaning that there is mode conversion to the mode 1 which takes place both at the crack and delamination at every position modelled.

Table 4.9: Comparison of the interaction of the fundamental modes at the centre excitation frequency of 100 kHz with damage. ✓- behaviour is observed, ✗- behaviour is not observed.

Mode	**Behaviour**	**Crack**	**Delamination Position**			
			(1)	(2)	(3)	(4)
Case 1: Excitation of mode 1						
1	Reflection	✓	✓	✓	✓	✓
2	Conversion	✓	✓	✓	✓	✓
Case 2: Excitation of mode 2						
2	Reflection	✗	✗	✗	✗	✓
1	Conversion	✓	✓	✓	✓	✓

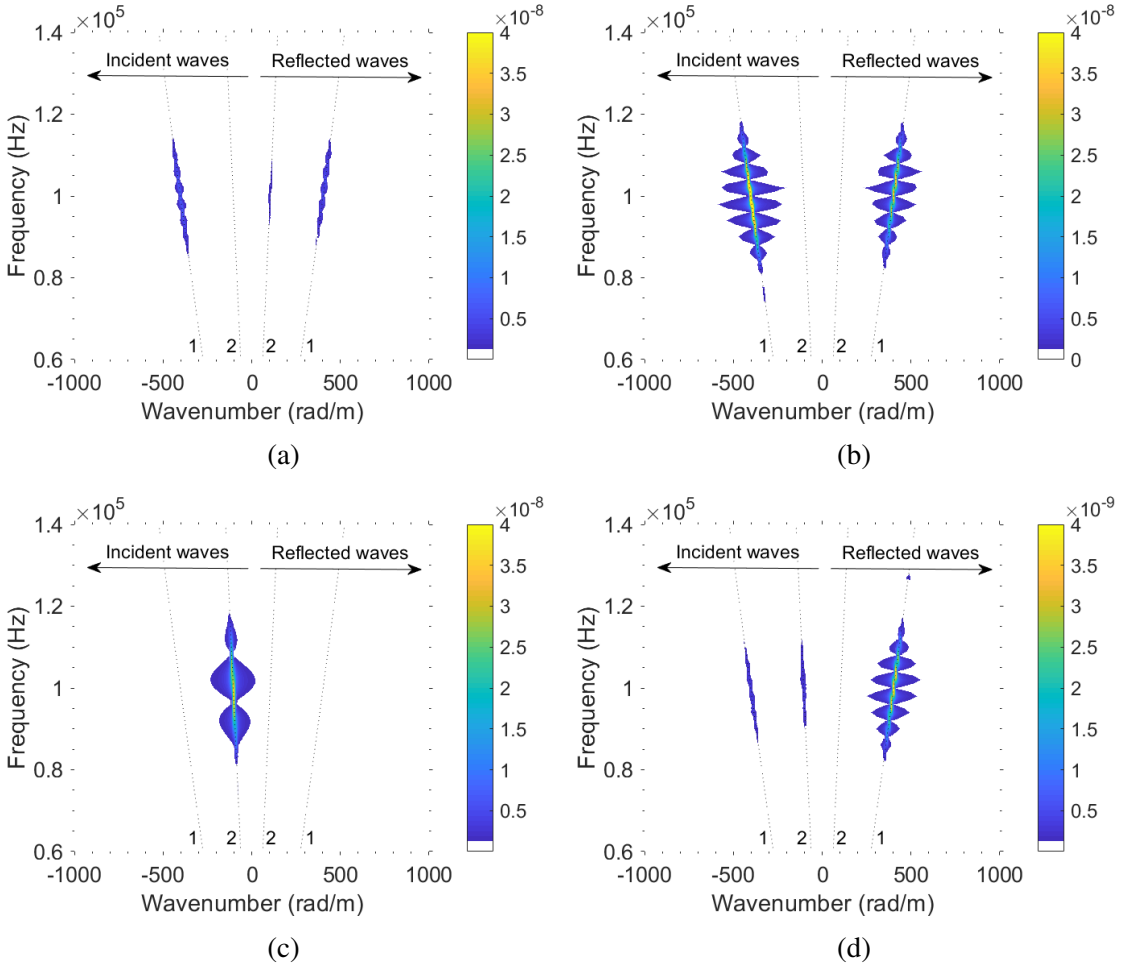

Figure 4.33: Interaction with the delamination at position (2) in the CFRP part of the hybrid plate. Frequency-wavenumber spectra of incident and reflected modes (a) for in-plane and (b) out-of-plane components while exciting the mode 1 at 100 kHz, (c) for in-plane and (d) out-of-plane components while exciting the mode 2 at 100 kHz.

4.3.2 Modes beyond cut-off frequencies

In this subsection the mode-damage interaction is analysed for the modes beyond cut-off frequencies, meaning that 3 or more modes exist simultaneously at each frequency. First, a crack in the aluminium part is considered followed by the analysis of the modes' interaction with a delamination positioned at different locations along the plate's thickness.

A crack in the aluminium part The results are presented in Figure 4.34. Two cases are compared in this figure, for the excitation of the mode 2 at 475 kHz, see Figure 4.34a and Figure 4.34b for the in-plane and out-of-plane components, respectively, and of the mode 5 at 475 kHz, see Figure 4.34c and Figure 4.34d for the in-plane and out-of-plane components, respectively. Despite that the excitation was performed by applying a corresponding mode shape at the central frequency of the desired mode to be excited, other undesired modes were excited too. However, these modes have much smaller displacements (about 10 times smaller). In the case of the mode 2 excitation, the mode 4 is excited too, whereas the excitation of the mode 5 leads to the excitation of the modes 1, 2 and 4, as to be seen in Figure 4.34. Even though, the same excitation frequency and number of cycles in the pulse are used in both cases, different modes are excited due to the different mode shapes used. The results show that regardless of how many modes are excited in the plate in the chosen frequency range, only the mode 2 and mode 4 interact with the crack.

Considering the shapes of the mode 2 and mode 5 shown in Figure 4.35a and Figure 4.35b, respectively, it is observed that the mode 5 has a very small displacement in the aluminium at 475 kHz, when compared to the CFRP part and the mode 2. The displacement of the mode 5 at this frequency is concentrated mainly in the CFRP laminate which might be the reason why this mode does not interact with a crack in the aluminium layer.

The modelling results for the modes beyond the cut-off frequencies are summarised in Table 4.10. Since many different modes are excited and propagating in the plate simultaneously, it is not possible to analyse mode conversion and thus only the reflection is analysed. As regards the crack in the aluminium liner, only the mode 5 and mode 7 do not interact. Considering the mode shapes, the mode 5 has a very small displacement in the aluminium layer compared to the CFRP plies (Fig. 4.35b). The same holds for the mode 7, not shown here for brevity. In contrast, other modes have comparable amplitudes in both aluminium and CFRP parts, see the mode shapes of the mode 2 (Fig. 4.35a), mode 4 (Fig. 4.35c) and mode 6 (Fig. 4.35d). To understand this behaviour, the dispersion curves of the single aluminium plate and single CFRP plate are calculated separately and compared to the dispersion curves of the coupled aluminium-CFRP plate.

In Fig. 4.36a and 4.36b the dispersion curves of the coupled 6 mm aluminium-CFRP plate are compared to the dispersion curves of the single 2 mm aluminium plate and 4 mm

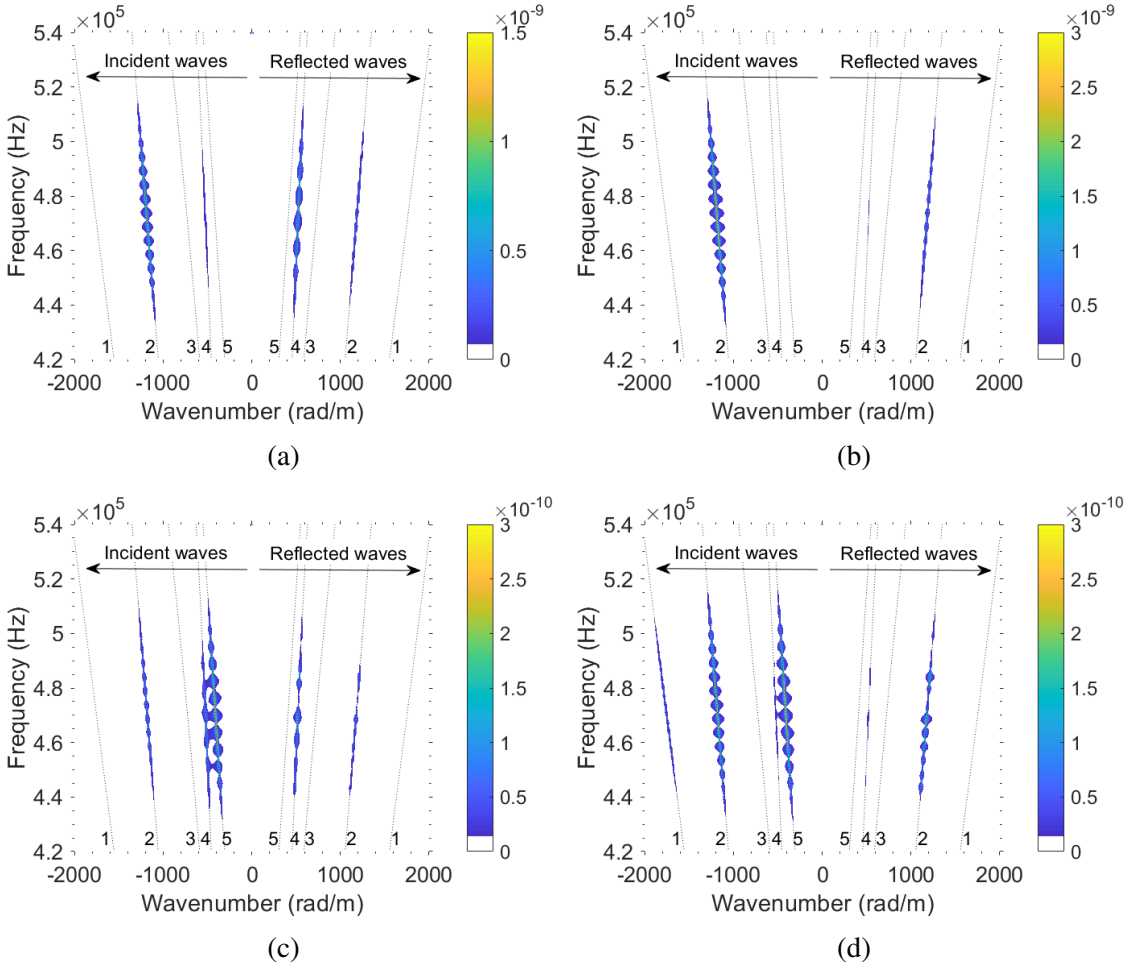

Figure 4.34: Interaction with the crack in the aluminium part of the hybrid plate. Frequency-wavenumber spectra of incident and reflected modes (a) for in-plane and (b) out-of-plane components while exciting the mode 2 at 475 kHz, (c) for in-plane and (d) out-of-plane components while exciting the mode 5 at 475 kHz. Own results published in [31].

Table 4.10: Comparison of the mode-damage interaction for the damage positioned in different parts of the structure. ✓- modes which reflect from the damage, ✗- modes which did not reflect from the damage. Own results partially published in [31].

Mode	**Frequency**	**Wavelength**	**Crack**	**Delamination Position**			
	kHz	mm		(1)	(2)	(3)	(4)
2	475	5.3	✓	✓	✓	✓	✓
3	950	2.9	✓	✓	✓	✓	✓
4	400	14.6	✓	✓	✗	✓	✓
5	475	15	✗	✓	✓	✓	✓
6	700	7.8	✓	✗	✓	✗	✗
7	860	11.6	✗	✓	✗	✓	✓

CFRP laminate, respectively. The dashed lines represent four guided wave modes in the 2 mm aluminium plate. The modes propagating in the CFRP laminate are marked with dashed-dotted lines. The combination of these two structures produces a set of GW modes shown with black lines. Hollow and filled circles mark modes which did not and did interact with a 1 mm crack in the aluminium layer, respectively. In Fig. 4.36a the modes of the combined structure are close to the modes of the single aluminium plate (marked with red dashed lines) which showed characteristic interaction with the crack (marked with filled circles). Note that the mode 2 (S0-like) interacts with the crack indirectly, as it was described in subsection 4.3.1, it does not reflect but converts to the mode 1 (A0-like). For all other modes the reflection is considered only. Modes marked with the hollow circles lay on the CFRP modes and did not reflect from the crack (red dashed-dotted lines in Figure 4.36b). These modes have a very small displacement in the aluminium part, *e.g.*, as can be seen in Figure 4.35b. Thus, modes of the combined structure can have different behaviour, either CFRP or aluminium dominated, or both. The fundamental modes in a low frequency range, for instance demonstrate the combined behaviour meaning that the energy propagates in both CFRP laminate and aluminium layer simultaneously. For the modes beyond cut-off frequencies, it is possible to have modes which displacement is concentrated either in the CFRP plies or in the aluminium layer. Thus, the energy "steering" depending on the mode and frequency can be used to allow for damage detection in different constituent parts of the hybrid plate. This result is supported by the experimental investigations of Kundu *et al.* [23] who showed that it is possible to find a damage positioned at different locations across the thickness of a laminate by changing the excitation frequency and transducer angle combinations (the air-coupled set-up was used in their studies).

A delamination in the CFRP part The same analysis was done for the delamination being modelled at different positions across the thickness of the CFRP laminate (Fig. 4.28). The results are summarised in Table 4.10. The modes 2, 3 and 5 interact with the delamination at every position. The interaction of other modes with the delamination depends on its position across the laminate's thickness. As in the case of the crack in the aluminium part, this can be attributed more to the mode shape than to its wavelength. For instance, the mode 1 (Table 4.9) and mode 5 (Table 4.10) reflect from the delamination even though having longer wavelength than the modes 4, 6 and 7 (Table 4.10). Every mode has comparable or bigger displacement amplitudes between the aluminium and CFRP parts, see example shown for some modes in Fig. 4.35. By analysing the mode shapes, it is hard to say, why some modes interact with the delamination, whereas the others do not. For example, both the mode 2 and mode 5 reflect from the delamination, even though the in-plane displacement of the mode 2 is almost zero at positions (2) to (4) [Fig. 4.35a], whereas for the mode 5, it is the out-of-plane

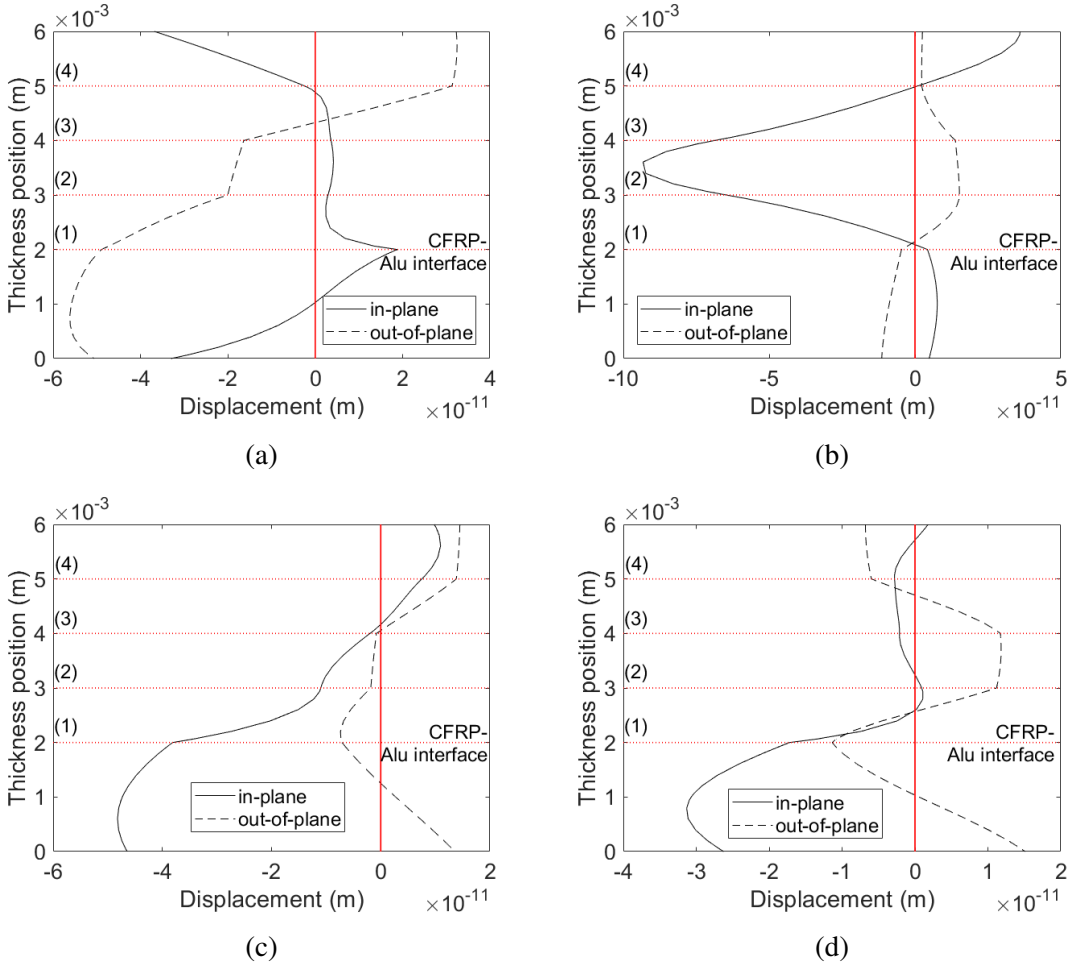

Figure 4.35: Mode shapes of (a) the mode 2 at 475 kHz, (b) the mode 5 at 475 kHz, (c) the mode 4 at 400 kHz and (d) the mode 6 at 700 kHz. Red-dotted lines mark delamination positions. Adapted from own results published in [31].

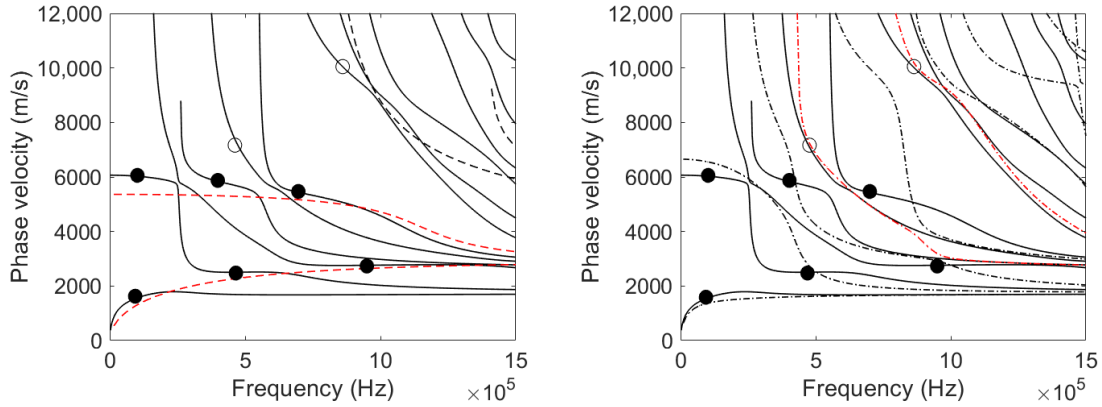

Figure 4.36: Combined phase velocity dispersion curves of (a) the 2 mm aluminium plate (dashed lines) and the 6 mm aluminium-CFRP plate (solid lines); (b) the 4 mm CFRP plate with a [90/0/90/90] layup (dash-dotted lines) and the 6 mm aluminium-CFRP plate (solid lines). The hollow and filled circles mark modes, which did not and did interact with a 1 mm crack in aluminium, respectively. Red dashed and red dash-dotted lines highlight two aluminium modes and two CFRP modes, respectively. Own results published in [31].

displacement which is close to zero at position (1) [Fig. 4.35b]. The mode 4 interacts with the delamination placed at positions (1), (3), (4), but not at the position (2). The out-of-plane displacement is almost equal at positions (1), (2), (3), and the in-plane displacement is equal at positions (2) and (3). The analysis was also done for normal and shear stresses, and for the power flux which is not presented here for brevity since no correlation between damage detection and stress or the power flux could be found.

4.3.3 Summary and key messages

In this section, a plate consisting of an isotropic metal bonded to anisotropic carbon fibre-reinforced layered material was considered. Dispersion curves were calculated to identify less dispersive modes for further numerical analysis of the GW propagation and interaction with different damage types.

Results show that there are modes which are sensitive to damage being located in the composite or the metallic part of the structure. This allows to distinguish between damage in different parts which is in agreement with the results published by Kundu *et al.* [23]. One has to be careful here, in the sense that right modes are used and that a damage in the CFRP laminate will not be mistaken for a damage in the aluminium liner. Which is why, it is important to be able to excite modes in different constituent parts of the component and that chosen modes show characteristic interaction only with the damage in one of the parts.

One solution for the reception as well as the excitation of the desired modes could be

an interdigital transducer (IDT) being specifically "tuned" to the frequency and wavelength sensitive to the respective damage to be monitored [188–194]. Figure 4.37 presents a sketch of such arrangement with the IDT being an additional layer integrated between the CFRP laminate and aluminium plate. The idea is to have two modes, let's call them arbitrarily $mode^N$ and $mode^M$, which ideally have the same wavelength ($\lambda_N = \lambda_M$) at different frequencies, *i.e.*, f_1 and f_2, respectively. Assuming $mode^N$ at f_1 is mainly propagating in the CFRP part and is particularly sensitive to damage in this part of the structure, whereas $mode^M$ at f_2 is mainly propagating in the aluminium part and it is sensitive to damage in this part. Such an arrangement would allow to independently excite two modes by driving the IDT at respective frequencies and by that to find and differentiate damage located in different parts of the structure.

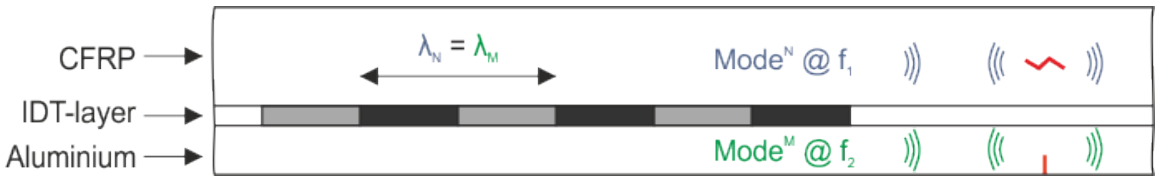

Figure 4.37: A sketch of an arrangement for an interdigital SHM system for composite pressure vessel monitoring. Adapted from own work published in [31].

Key messages

- *Is it possible to distinguish between damage in the metallic part from damage in the CFRP part?* The results showed that different modes exist in the multi-layered plate studied here and that their energy can be frequency steered to allow not only for damage detection but also for its localisation within different layers.

- *Are the fundamental modes in the low frequency range sufficient to distinguish between damage located in different parts of the structure?* The numerical modelling demonstrated that the fundamental modes in the low frequency range reflect and convert from both damage in the aluminium and CFRP part. Thus, it is not possible to tell in which part of the structure damage is present. Nevertheless, it was found that it is possible to distinguish between damage located in different parts of the structure by higher order modes.

In the next section, the same structure having a real impact damage at different locations is investigated experimentally. Two quantitative techniques for damage sizing based on guided wavefield measurements and wavenumber mapping are compared.

4.4 Damage quantification using GW-based wavenumber mapping

This section is dedicated to the damage quantification using the GW-based wavenumber mapping. Two approaches - instantaneous and local wavenumber - are implemented and their comparison on real impact-induced damage is done for the first time. At first, the numerical validation is performed on a simple example of a 'delamination' damage in an aluminium plate. At next, the wavenumber mapping approaches are applied to quantify a real impact-induced damage in the aluminium-CFRP plate.

4.4.1 Numerical validation

Figure 4.38 shows an example of a modelled wavefield at the time instant of 117.36 µs. The numerical set-up is described in section 3.2 ("Wavenumber mapping"). This figure presents the out-of-plane displacement only, thus the expected amplitude of the A0 mode is much larger than of the S0 mode. At this time instant the faster S0 mode has travelled to the right edge of the plate, reflected from it and travels back to the damaged area. In Figure 4.38a the interaction of the slower A0 mode with the damage can be observed.

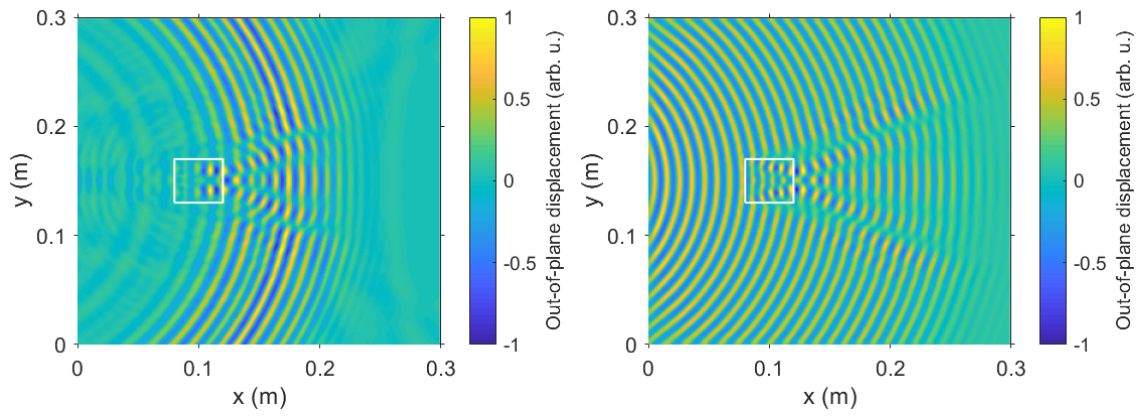

Figure 4.38: (a) A modelled wavefield at a time instant of 117.36 µs of guided waves propagating and interacting with damage in a 2 mm aluminium plate. (b) a single frequency wavefield obtained using a pre-processing workflow shown in Figure 3.13. The delamination is denoted by the white rectangle. Own results published in [166].

As it was discussed in subsection 3.7.2, in order to estimate the depth of a damage, it is advantageous to work with a single frequency and a single mode sensitive to the thickness changes. For this the dispersion relation as a function of effective thickness (ET) must be calculated in advance. Figure 4.39 presents the relation for the S0 and A0 modes at f =

150 kHz for aluminium. At this frequency the A0 mode is especially sensitive to the thickness change between 0.1 mm and 4 mm. Higher wavenumbers correspond to smaller thicknesses, and *vice versa*. From the thickness of 4 mm on, the difference between two respective wavenumbers in relation to the ET decreases. Thus, the estimation of the actual thickness while working in this range becomes harder. Regarding the S0 mode, its wavenumber does not change with the thickness at this frequency and so this mode cannot be used for the ET estimation.

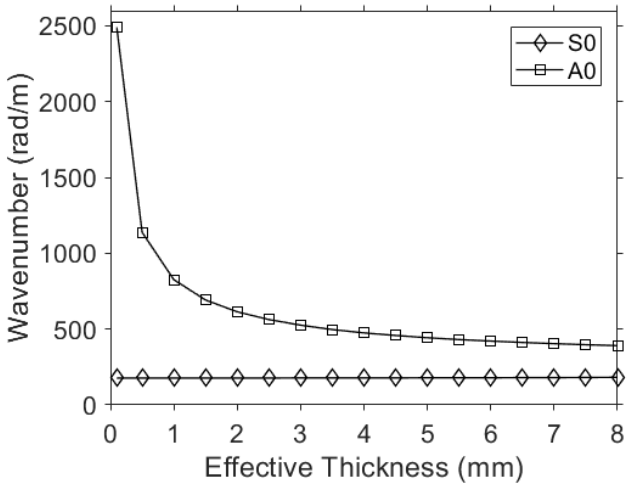

Figure 4.39: Dispersion relation for the A0 and S0 modes at $f = 150$ kHz in aluminium as a function of the effective thickness. Own results published in [166].

Hence, the A0 mode at $f = 150$ kHz is a good choice for the ET estimation. Following the pre-processing steps described in subsection 3.7.2, the S0 mode is filtered out and the 150 kHz frequency wavefield shown in Figure 4.38b is obtained. After the pre-processing steps, the wavefield covers the entire area, as if the plate was excited continuously.

Next, the wavenumber maps using the IW and LW approaches are calculated as described in subsection 3.7.2. Figure 4.40 presents the resulting wavenumber maps. Both maps clearly indicate the actual damage size and its position (highlighted with a white square). This is possible because the A0 mode propagating in the pristine region of the 2 mm plate has a completely different wavenumber than the A0 mode propagating in the delaminated region which is represented by an independent 1 mm plate. The A0 mode has the wavenumbers of 809 rad m^{-1} and 610 rad m^{-1} at the chosen frequency for the 1 mm and 2 mm plates, respectively (see Fig. 4.39). These wavenumbers are clearly identifiable in Figure 4.40: $k = 809$ rad m^{-1} at the delaminated region and $k = 610$ rad m^{-1} at the pristine region. Since the evaluation is performed at the plate's surface, the delamination region visible on the wavenumber maps corresponds to the upper 1 mm plate. Thus, it is not possible to estimate any potential damage underneath the delamination region if it is smaller or in the order of

the delamination size due to the shadowing effect. Moreover, there are diagonal lines in the shadowed region behind the delamination (Fig. 4.40) which come from a phase discontinuity due to the scattering of waves at damage [179]. This artefact is very pronounced in the case of the IW, whereas the LW is less susceptible to it. Finally, an almost vertical artefact is visible on the extreme right side of each wavenumber map which is due to the end of the modelling time before the A0 mode reaches the end of the inspected area (Fig. 4.38b), hence the wavenumber values reach a discontinuity in this area.

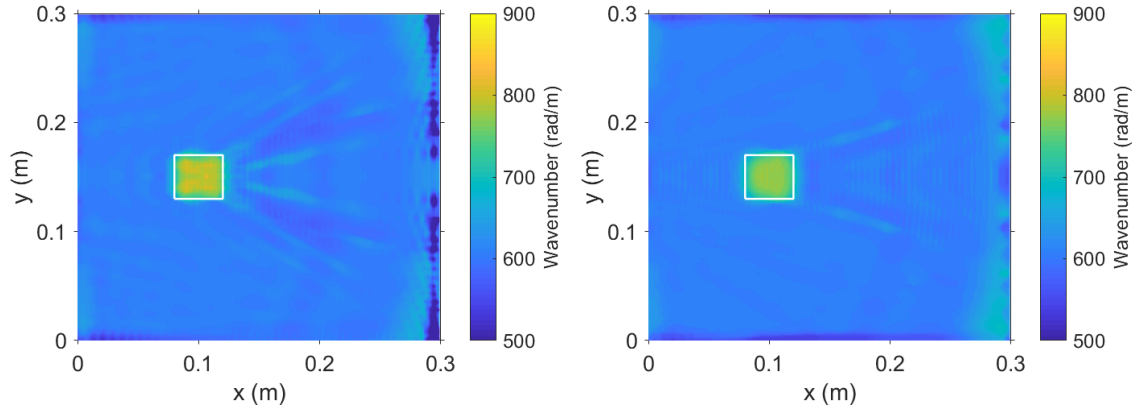

Figure 4.40: Wavenumber maps calculated using the (a) IW and (b) LW approaches for the 2 mm aluminium plate with a $40 \times 40\,\mathrm{mm}^2$ delamination at the depth of 1 mm. Own results published in [166].

Using the dispersion relation in Figure 4.39, the wavenumber maps are converted into the ET maps shown in Figure 4.41. This conversion allows to recover the damage depth with respect to the plate's surface. Both IW and LW approaches closely indicate the actual depth of the delamination while the size is slightly over-estimated in the wave propagation direction.

For the quantitative comparison of the wavenumber mapping approaches, a cross-sectional cut along the x-axis is taken at the middle of the plate with respect to the y-axis, as shown with the red and dashed blue lines in Fig. 4.41a and 4.41b, respectively. The quantitative comparison presented in Figure 4.42 indicates that the LW approach overestimates the damage depth as 1.07 mm instead of 1 mm when compared to the reference and the IW approach. This is due to the window size required for the LW which is chosen to be twice the size of the wavelength expected in the pristine plate. This wavelength is bigger than that of the damaged area leading to the smoothing of the wavenumbers in this area. Therefore, the damage position across the thickness is estimated closer to the surface as it is. Note that none of the methods estimates the ET uniformly. In the edge regions of damage, the ET monotonously decreases from the thickness of the pristine plate to the thickness at which the

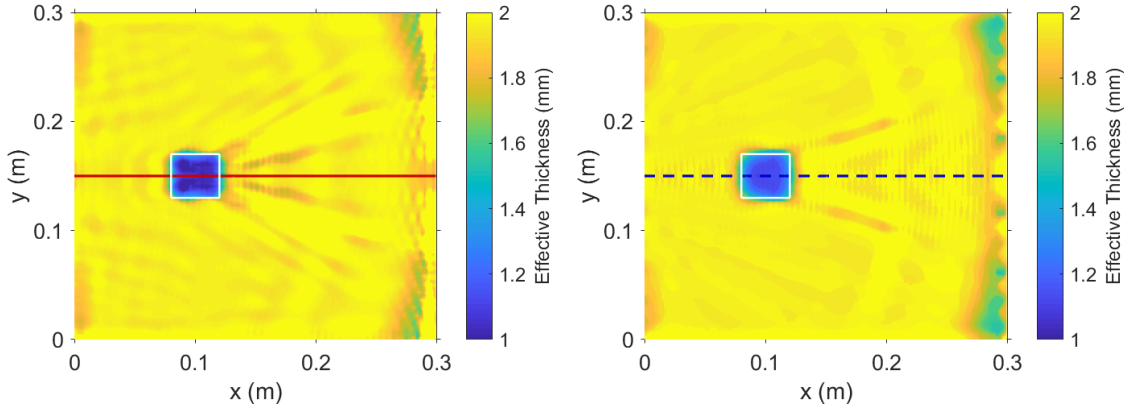

Figure 4.41: Effective thickness maps of the 2 mm aluminium plate with a $40 \times 40\,\mathrm{mm}^2$ delamination at the depth of 1 mm estimated using the dispersion relation from Fig. 4.39 and the (a) IW and (b) LW maps from Fig. 4.40a and 4.40b, respectively. Own results published in [166].

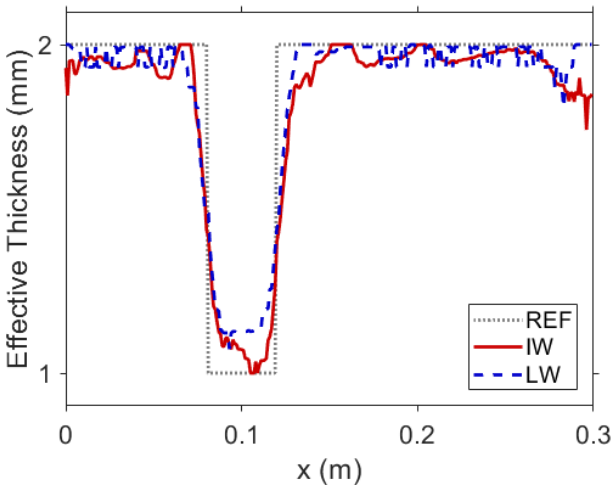

Figure 4.42: Comparison of cross-sectional cuts of wavenumber approaches from Fig. 4.41 to the reference. Own results published in [166].

damage is present resulting in the overestimated in-plane size of the damage.

The calculations were done in MATLAB for a 512 x 512 x 2048 wavefield data set on a 64-bit Windows 10 PC with 16 GB RAM. In terms of computational performance, the IW and LW took 0.1 s and 856 s to compute, respectively. The high computational cost in the case of LW is due to the zero padding inside the window (up to 512 points in both spatial directions).

4.4.2 Experimental validation

Ultrasonic immersion testing As the reference method, high frequency ultrasonic testing in immersion is used, which excites bulk waves in the sample. Figure 4.43 presents a time-of-flight (ToF) image in the aluminium-CFRP plate estimated with respect to the first wall echo (water/CFRP interface). Only two out of three impacts lead to the visible damage in the CFRP laminate. The impact in the left-upper corner did not cause any visible damage, see Fig. 4.43 [top] for reference. The impact damages are framed by a white dashed rectangle and their enlarged view is shown in Fig. 4.43 [bottom]. In this figure in the left-upper corner delaminations across the thickness of the CFRP caused by the impact of 30 J are present. Their size increases with depth. The impact of 10 J caused a smaller damage as can be seen in the right-bottom corner. The biggest delamination is present at interface '6' and it seems that the damage due to the biggest impact of 30 J extends over the two other impacts of 5 J and 10 J. The extent of the delamination at interface '6' is 192 mm and 184.4 mm in the x- and y-directions, respectively.

Taking a closer look at the enlarged view in Figure 4.43 (bottom), a typical pattern of delaminations between the CFRP plies can be observed [195]. This is especially pronounced in the case of the biggest impact of 30 J (see the left-upper corner in Figure 4.43 [bottom]). The size of delaminations increases through the thickness of the plate and are visible at interfaces '1' through '3', as well as '5'. Only the delamination at interface '4' seems not to extend so much over delaminations from the previous interfaces and only tiny areas of it are visible (see green colour in Figure 4.43 [bottom]). The total size of the damage within the CFRP laminate caused by the 30 J impact is 54.4 mm and 32.8 mm in the x- and y-directions, respectively. According to [196], the shape of an impact damage can be approximated to an ellipse. Using this approach the resulting area is estimated as $\approx 1400\,\text{mm}^2$. As for the damage caused by the 10 J impact, which can be seen in the right-bottom corner of the enlarged view in Figure 4.43 (bottom), it is not possible to clearly identify the borders of delaminations at individual CFRP plies due to their small sizes and the scan resolution used. Thus, only the overall extent of this impact damage is estimated. The size is equal to 14.3 mm and 14.9 mm in the x- and y-directions, respectively, resulting in the area of $\approx 167\,\text{mm}^2$.

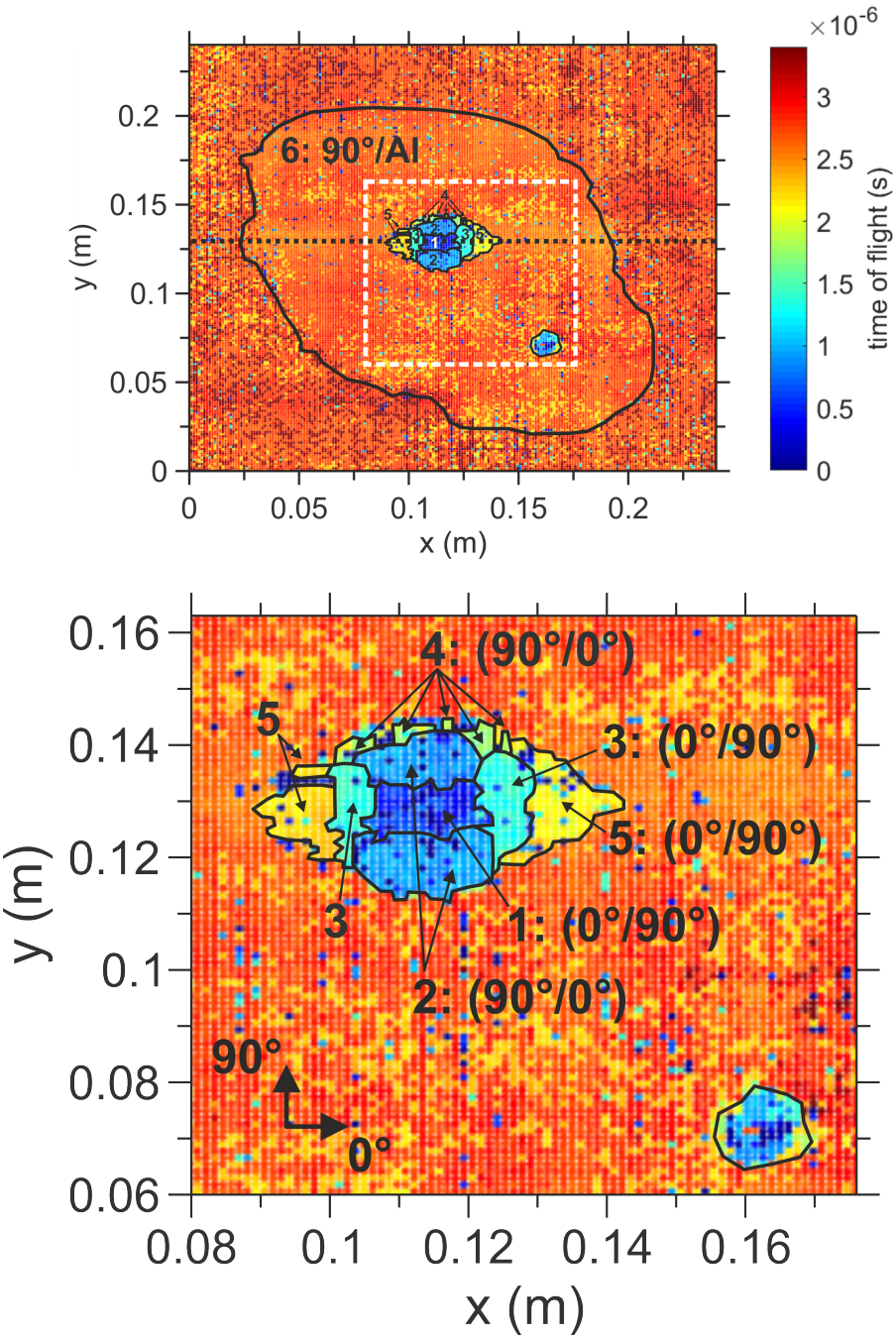

Figure 4.43: A ToF image (top) and its enlarged view (bottom) of the aluminium-CFRP plate obtained using immersion testing. The white dashed rectangle marks the area used for the enlarged view. Black dotted line marks the position of the cross-sectional cut which is presented in Figure 4.51. Black solid lines mark contour of the impact damage. Numbers show the interfaces at which the delamination is present across the sample thickness as can be seen in Figure 4.44. Own results published in [166].

Choice of excitation frequencies for wavenumber mapping To be able to select a centre excitation frequency wisely, dispersion curves for a given structure have to be calculated and analysed in advance. Using the dispersion curves, a trade-off between mode sensitivity to thickness changes and required spatial resolution has to be found. Typically, it is better to avoid higher frequencies because they require finer grid so that the smallest expected wavelength (highest wavenumber) can be appropriately resolved. According to [49, 138, 141] approximately ten spatial steps per wavelength are necessary to be able to resolve the desired wavelength. Moreover, because of the asymmetry of the composite specimen used in this study two sets of dispersion curves have to be considered: one from the Al-side and one from the CFRP-side. Using these relationships, a wavenumber map can be converted to an ET map and thus the delamination depth can be estimated. It is expected that in the pristine region the ET is equal to the total thickness of the aluminium-CFRP composite plate. Whereas, in the delaminated region the value of the ET corresponds to the depth at which the delamination is present and thus it is smaller than the total thickness of the hybrid composite plate. Since a delamination may only appear in-between plies, the ET values are discretised to match the number of interfaces. Figure 4.44 shows the schematic of the wavenumber (wavelength) dependence on the ET with the interfaces marked from '1' to '6' with respect to the CFRP-side (side of the impacts). Based on this figure, seven ETs are considered – six for each interface plus one for the pristine plate. The calculations in the SBFEM were performed for seven composite plates made of a single CFRP ply, two CFRP plies, *etc.* up to the total thickness of the aluminium-CFRP composite plate. The material properties listed in Table 3.1 and 4.11 were used.

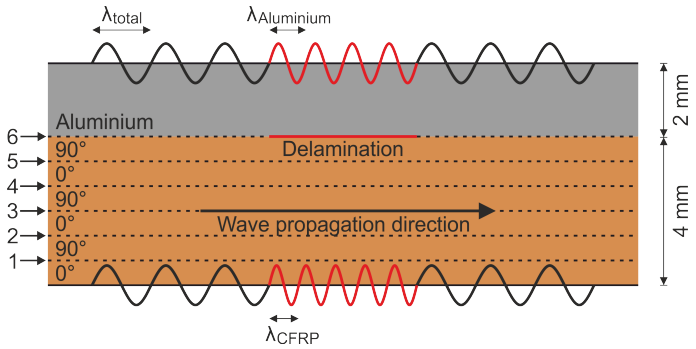

Figure 4.44: Schematic showing dependence of damage depth (effective thickness) on the wavelength of guided waves. Interfaces are numbered from 1 to 6 with respect to the CFRP-side [166].

Since the aluminium-CFRP plate is not symmetric with respect to its middle, the modes cannot be separated into antisymmetric and symmetric. The first two modes only resemble the S0 and A0 modes and therefore, they will be called the S0- and A0-like modes in the following. Figure 4.45 presents the dispersion relation considered with respect to the CFRP-

side as a function of the ET for 100 kHz (Fig. 4.45a), 150 kHz (Fig. 4.45b) and 200 kHz (Fig. 4.45c). All relations are non-monotonous meaning that the ET cannot be estimated uniquely in this case. It is remarkable from Figure 4.45 that the wavenumber increases when a 90° CFRP-layer is added to the plate (wavenumbers marked with arrows), while an addition of a 0° layer and aluminium plate leads to a decrease in the wavenumber. This behaviour is observed also when other frequencies and modes are used (not shown here), which allows to conclude that this non-monotonous relation comes from the plate's layup and its anisotropy. The difference in the material properties and therefore in the behaviour of GW for 0° and 90° layers is so big in the case of CFRP that it leads to the non-monotonous relation between wavenumber and thickness (Figure 4.45). Similar behaviour for a CFRP laminate was observed in [141], which was not the case for a glass fibre-reinforced plastic (GFRP) laminate [140]. This is because glass fibres have a lower strength than carbon fibres and thus the difference in wave velocities in the 0° and 90° directions are less pronounced.

It can be observed from Figure 4.45 that the A0-like mode is sensitive to the thickness variation for all three frequencies. With the frequency increase, the wavenumbers considered with respect to the same thickness increase too. Moreover, the difference between the wavenumbers for one CFRP ply and the aluminium-CFRP plate increases with the frequency, *e.g.*, the wavenumber difference for 100 kHz, 150 kHz and 200 kHz are 300 rad m^{-1}, 374 rad m^{-1} and 423 rad m^{-1}, respectively. These differences were calculated based on the fitted values shown with the dashed lines in Figure 4.45. To eliminate the ambiguity in the wavenumber-thickness relation, a quadratic interpolation of the wavenumbers was used.

It can be concluded that $f = 200$ kHz is very advantageous for the ET estimation, since it has the biggest variation of the wavenumbers, however, it would require a spatial resolution of ≈ 0.6 mm, which is not possible with the current experimental set-up with the 3D LDV system as shown in Figure 3.7a and described in subsection 3.4.1. As for the frequencies of 100 kHz and 150 kHz, the maximum expected wavenumbers are 700 rad m^{-1} and 970 rad m^{-1}, respectively. Thus, the spatial step of 0.81 mm defined by the measurement set-up results in 11 and 8 points per wavelength, respectively. Therefore, the frequency of 100 kHz is chosen to fulfil the requirement of ten spatial steps per wavelength [49, 138, 141]. Moreover, for this complex experimental case, it is assumed that the ET-wavenumber relationship is monotonous. Note that for GFRP laminates which have bijective ET-wavenumber relationships, a discretised set of ET values corresponding to the laminate layup may be used [140].

As for the dispersion relation considered with respect to the Al-side, the behaviour is the same as for the CFRP-side – an decrease or an increase in the wavenumbers can be observed when adding a 0° or a 90° layer. The results are not shown here for brevity. The result from the conventional UT demonstrates that the biggest delamination is at the aluminium-CFRP interface (interface '6' in Figure 4.43 and Figure 4.44). Thus, it is expected that

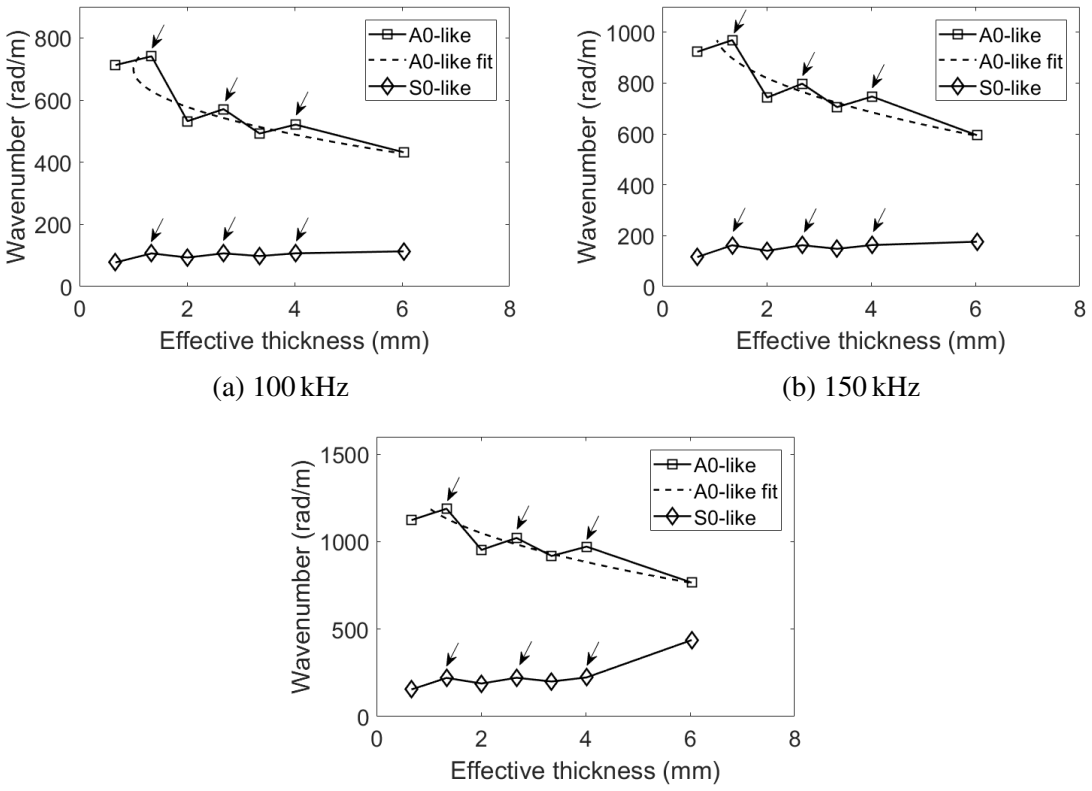

(a) 100 kHz

(b) 150 kHz

(c) 200 kHz

Figure 4.45: Dispersion relations with respect to the CFRP-side of the A0- and S0-like modes at different frequencies as a function of the effective thickness. The arrows mark the wavenumbers resulting from the addition of a 90° CFRP layer. Own result published in [166].

this delamination will hide all other smaller delaminations within the CFRP laminate when measured from the Al-side due to the shadowing effect. Therefore, the dispersion relation is simplified by considering only two ET-wavenumber pairs at one frequency. The biggest difference of 50 rad m^{-1} between two wavenumbers is found to be for $f = 100$ kHz and this frequency is used in the experiment as the centre excitation frequency. The expected wavenumbers are 432 rad m^{-1} for the 6 mm pristine aluminium-CRRP composite plate and 482 rad m^{-1} for the 2 mm aluminium plate, both of which can be resolved with the spatial step of 0.8 mm defined by the measurement set-up.

Table 4.11: Material properties of a single transversely isotropic ply, where the direction '1' is along the fibres.

ρ (kg/m^3)	D_{11} (GPa)	D_{12} (GPa)	D_{23} (GPa)	D_{44} (GPa)	D_{55} (GPa)
1446	98.9	5.8	3.5	2.6	3.6

Energy maps Figure 4.46 presents the energy maps of the measured wavefields calculated using Eq. (3.28). The biggest delamination at interface '6' becomes visible in both measurements, from the aluminium side (Fig. 4.46a) and from the CFRP side (Fig. 4.46b). Additionally, the damaged area at the site of the biggest impact becomes visible in the middle of the scanned area for the measurement performed on the CFRP-side, see red colour in the middle of the scan area in Fig. 4.46b. This high amplitude when compared to the rest of the damaged area is possibly due to the mode trapping between delamination boundaries. The smaller impact damage visible in the reference measurement (Fig. 4.43) could not be observed in the WRMS maps (Fig. 4.46). It is very interesting that the WRMS values increase at the delamination at interface '6' when compared to the values of the pristine plate, confer Fig. 4.46b and 4.46a for the measurement on the CFRP side and the aluminium side, respectively. This is possibly due to the amplitude of the A0 mode being higher in this frequency range in the pure aluminium plate and the CFRP laminate when compared to the amplitude of the A0-like mode propagating in the pristine aluminium-CFRP plate.

Furthermore, the SNR were calculated for both measurements using the following formula: $SNR = 20 \log \frac{S}{N}$, where S and N are the maximum amplitudes of time signal and noise signal, respectively. The noise level was estimated by taking the maximum value at the first 100 µs of the time signal (marked in red in Figure 4.47). Time signals of a middle point along with SNRs for both measurements are shown in Figure 4.47. SNR is the highest for the measurement performed on the Al-side and is equal to 22 dB. The SNR for the measurement on the CFRP side is 18 dB, resulting in the difference between the SNR of two measurements of a factor of 1.8.

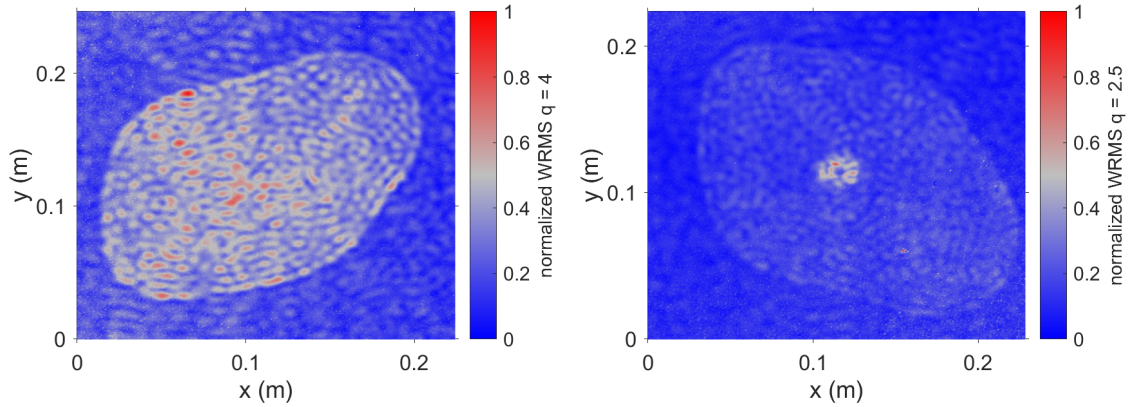

(a) (b)

Figure 4.46: WRMS-maps for the measurement on the (a) aluminium side and (b) CFRP side at the centre excitation frequency of 100 kHz. Own result published in [166].

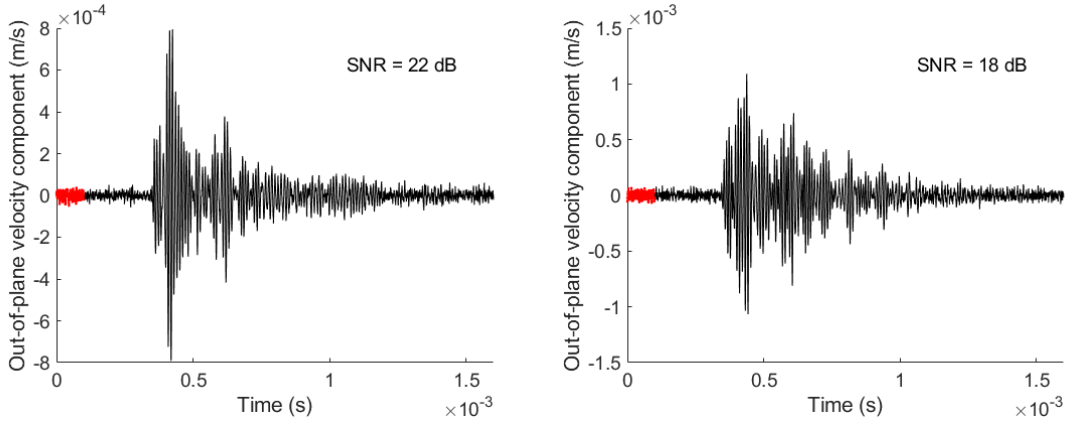

(a) (b)

Figure 4.47: Time signals of a middle point for the measurement on the (a) aluminium side and (b) CFRP side. First 100 µs marked in red were taken to estimate the noise level.

Wavenumber mapping from the CFRP side Figure 4.48a shows the interaction of the S0- and A0-like modes with the impact damage at 366.4 µs for the measurement performed on the CFRP surface. The S0-like mode is faster, has bigger wavelength and lower amplitude when compared to the A0-like mode. At this instant of time the S0-like mode is all over the scanned region, whereas the A0-like mode arrives at the left edge of the delaminated region. The propagation of the S0-like mode over the damaged area leads to its conversion to the A0-like mode. The converted mode scatters in all directions highlighting the delamination contour. Note that the mode and frequency filtering described previously will incorporate the mode contribution from both the incident and converted A0-like mode, since the wavenumber within the delamination is equal for both phenomena.

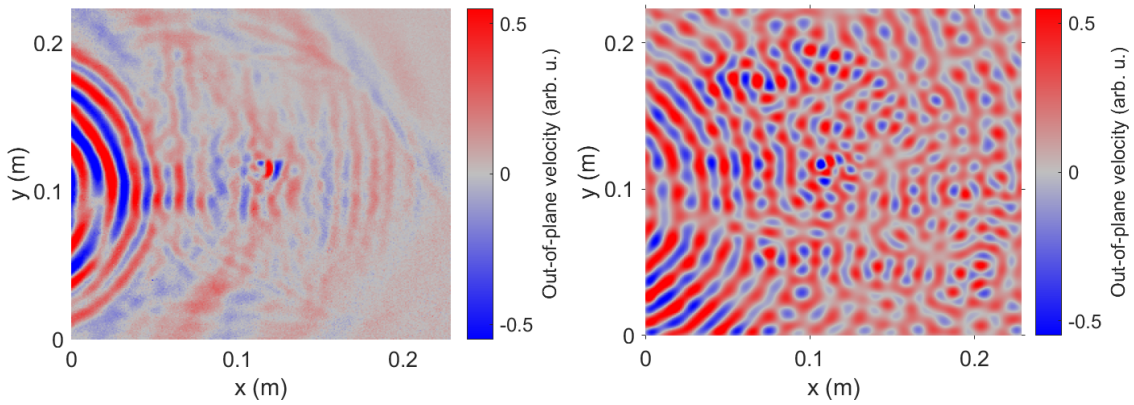

Figure 4.48: Interaction of the excited modes with the impact damage measured from the CFRP side. (a) Original snapshot of the wavefield at 366.4 µs and (b) the 100 kHz frequency A0-like-only wavefield obtained using a pre-processing workflow shown in Figure 3.13. Own result published in [166].

The pre-processing of the data was done in the same way as for the aluminium plate (Fig. 3.13) such that the one-mode-one-frequency wavefield can be obtained. The only difference is that wavenumbers for the A0-like mode were taken for every angular direction to capture the scattering at the delamination which also happens in every direction. To be able to calculate the 3D FFT in MATLAB for a 512 x 512 x 4096 wavefield data set, time signals were cut in the beginning and at the end (where only noise is present), but without reducing the time resolution. The calculations were done on a 64-bit Windows 10 PC with 32 GB RAM. In terms of computational performance, the IW and LW took 0.1 s and 676 s to compute, respectively. The resulting wavefield is shown in Figure 4.48b to which the wavenumber mapping algorithms are then applied.

Figure 4.49 presents the resulting wavenumber maps. While the impact damage is not observable in the single frequency wavefield in Figure 4.48b, every wavenumber map presented in Figure 4.49 highlights the damage size and shape. The most uniform damage

indication is delivered by the LW approach (Fig. 4.49b) due to its insensitivity to the directional information of scattered waves. The estimated wavenumbers of the pristine region are between 380 rad m^{-1} and 419 rad m^{-1}. In the case of the delaminated region (at interface '6') the wavenumbers are spread between 470 rad m^{-1} and 559 rad m^{-1}. In the middle of the scanned area the highest wavenumber of 676 rad m^{-1} is observed, thus, indicating a shallower delamination.

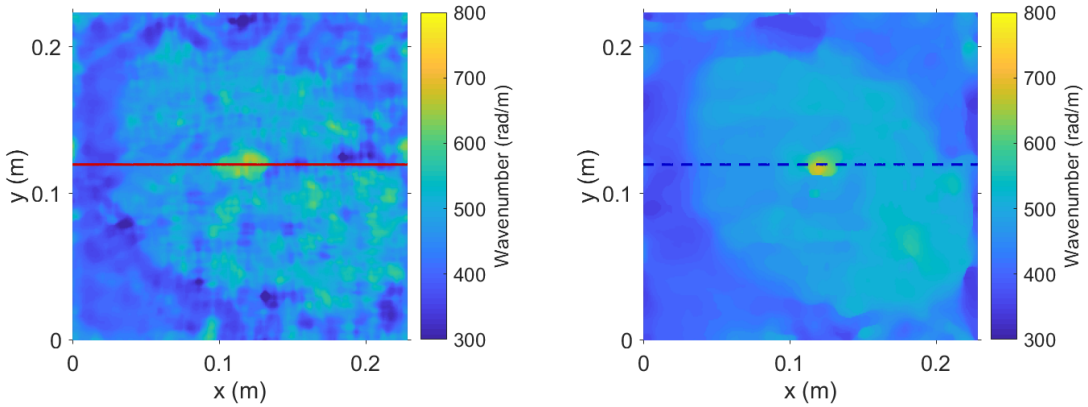

(a) IW (b) LW

Figure 4.49: Comparison of wavenumber estimation results for the aluminium-CFRP plate while scanning on the CFRP-side. Solid red and dashed blue lines mark the position of cross-sectional cut which is presented in Figure 4.51. Own result published in [166].

The fitted dispersion relation (see the dashed-line in Figure 4.45a) is applied to the wavenumber maps to retrieve the ET maps presented in Figure 4.50. The contours of the damage obtained from the conventional UT and WRMS mapping are plotted over the ET maps with black and red dashed lines, respectively. The shape of the damage obtained using wavenumber mapping approaches slightly deviates from the ones using the UT and WRMS mapping, to be seen in Fig. 4.50, Fig. 4.43 and Fig. 4.46b, respectively. The ET maps estimate correctly the total thickness of the plate in most of the pristine region (see yellow colour for the thickness of 6 mm in Figure 4.50). For the whole damaged region, blue, green and orange colours are present, corresponding to the thickness values around 2 mm, 4 mm and 4.5 mm, respectively. The largest delaminated region is at the aluminium-CFRP interface (interface '6' in Figure 4.43), thus the expected value for the ET is 4 mm which correlates with the estimate obtained from the ET maps (see green colour in Figure 4.50). Also, the ET maps indicate the shallower delamination in the middle of the sample (the ET values between 1.1 mm (blue) and 2.94 mm (light blue) in Figure 4.50). However, no clear indication of the multiple delaminations in the CFRP laminate (due to the biggest impact) and their shape can be observed, as it can be done for the reference measurement. Moreover, there is no indication of other impact damage which is expected in the right-bottom area. Note

orange colour visible in the damaged region, corresponding to the ET of ≈ 4.5 mm, which is impossible in this case because the aluminium plate has no damage in it. This is due to the continuous wavenumber-ET relation considered - the wavenumbers between 490 rad m^{-1} and 430 rad m^{-1} get assigned to the thickness values between 4 mm and 6 mm (Fig. 4.45a).

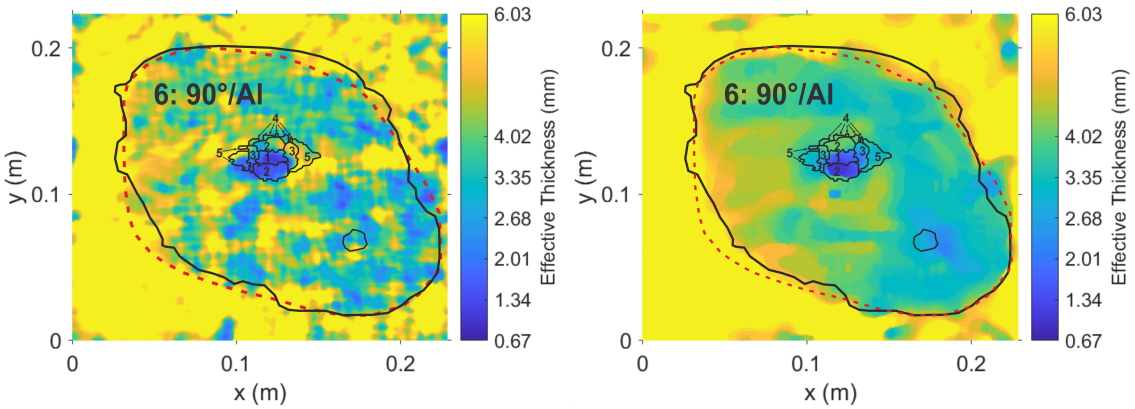

(a) IW (b) LW

Figure 4.50: Comparison of ET estimation results for the aluminium-CFRP plate while scanning on the CFRP-side. Black and red dashed lines show the damage contours extracted from the UT and WRMS-maps shown in Figure 4.43 and 4.46b, respectively. Own result published in [166].

Further, the wavenumber mapping results are analysed quantitatively through a cross-sectional view shown in Figure 4.51. This figure shows the overlap of the wavenumber techniques with the ToF measured by conventional UT. The alignment has been made by hand as the UT and GW measurements do not have the same coordinate system. Note that the y-scale of wavenumber and ToF are not directly comparable because the ToF variation is linear with the depth of the defect, whereas the wavenumber is not (Fig. 4.45a). Nevertheless, the wavenumber techniques succeed to detect the shallower defect at the appropriate location, *i.e.*, shortest ToF (called defect peak in the following), with sensibly similar extreme values. It seems that the x-extent of the damage peak is better captured by the IW approach, however, this result might not be generalisable. On the left-hand side, which is between the wave excitation and the defect peak, the wavenumber estimate is spatially constant and equal for both techniques. This is not the case on the right-hand side of the defect, where the IW result oscillates, while the LW is relatively constant but seems to overestimate the wavenumber. The difference between right and left sides with respect to the damage peak can be either attributed to the scattered waves from the damage peak or to the lower amplitude of the wave due to attenuation. Moreover, the fact that the wavenumbers are equal but slightly over the expected 432 rad m^{-1} value on the left side of the defect peak might indicate the shortcoming of the model described in Figure 4.44 with respect to effective ply thickness and material properties.

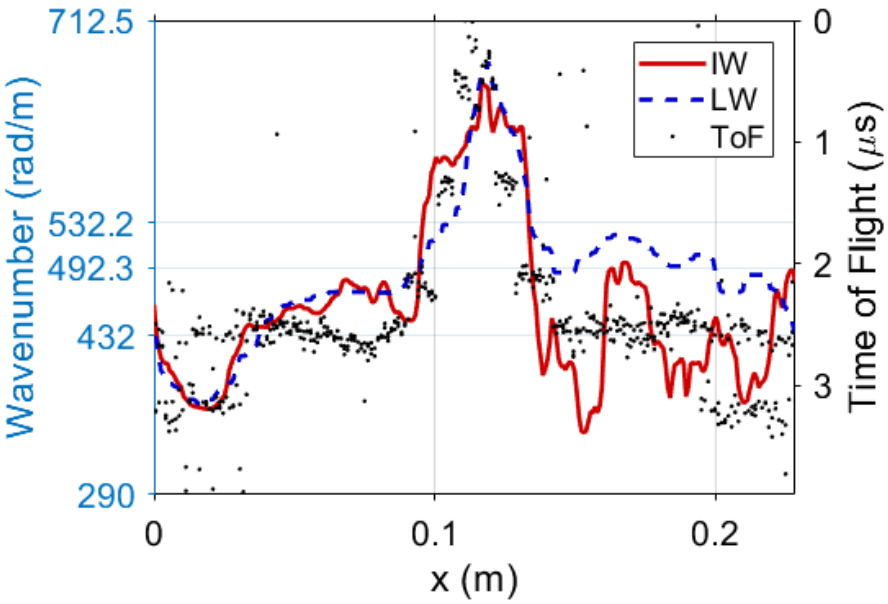

Figure 4.51: Comparison of cross-sectional cuts of three wavenumber approaches shown in Fig. 4.49 and conventional UT from Fig. 4.43. Own result published in [166].

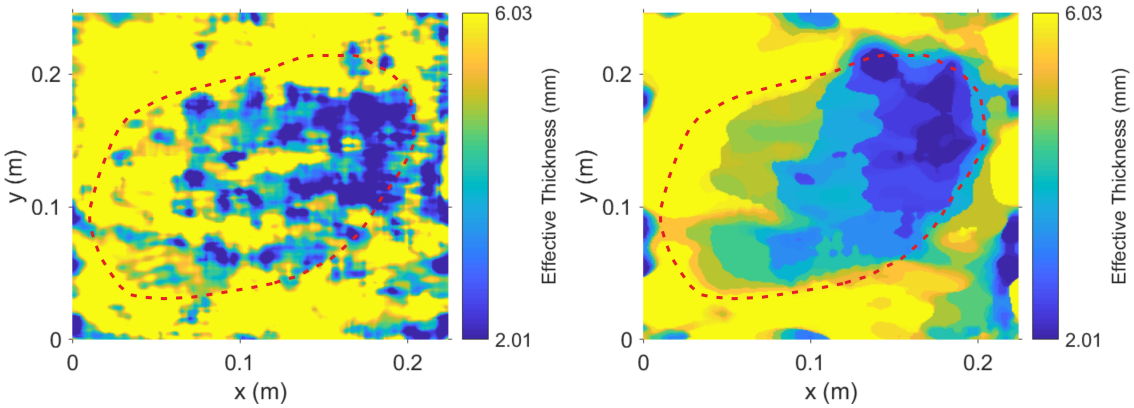

(a) IW (b) LW

Figure 4.52: Comparison of ET estimation results for the aluminium-CFRP plate while scanning on the Al-side. The red dashed line shows the damage contour extracted from the WRMS-map shown in Figure 4.46a. Own result published in [166].

Wavenumber mapping from the aluminium side Figure 4.52 shows the ET maps for the measurement done on the Al-side. It is not possible to clearly identify the shape of the damage from the ET maps as in the case of the analysis performed from the CFRP-side (confer Figure 4.52 and Figure 4.50). The ET maps for the measurement performed on the Al-side are distorted and it seems that aluminium is delaminated from the CFRP in different regions of the area scanned (see blue colour in Figure 4.52). Since the SNR of the measurement performed on the Al-side is higher than the one done on the CFRP-side (Fig. 4.47), the poor result with respect to the Al-side probably comes from the small difference between the wavenumbers for the pristine composite and single aluminium plate of only 50 rad m^{-1} rather than the measurement noise. Note that in the case of the LW (Fig. 4.52b) a similar damage pattern appears as for the ET maps estimated from the CFRP-side (Fig. 4.50), however, it is much harder to recognise without knowing the shape in advance. Finally, the computational costs were 756.3 s (LW) and 0.1 s (IW).

4.4.3 Summary and key messages

In this section, the instantaneous and local wavenumber mapping techniques were compared. First, the techniques were demonstrated on a numerical example of a damaged aluminium plate before their application to an experimental case. For the numerical case, both approaches showed similar performance in terms of quantification of damage size and depths. The in-plane size of the damage was slightly overestimated in the direction of the incidence wave for all approaches. For the experimental case, an aluminium-CFRP composite plate with real impact damage was measured and analysed. This structure corresponds to composite pressure vessels with a load-sharing metal liner used for storing gases in aerospace and automotive industries. Due to asymmetry of the plate, two cases were considered - for the measurements performed from the CFRP- and Al-sides.

The energy maps for both measurements revealed the biggest delamination present between aluminium and CFRP parts. As for the wavenumber mapping for the measurement from the CFRP-side, it has also revealed the biggest delamination between aluminium and CFRP parts and delivered an indication of impact damage in the CFRP part. In general, the damage quantification results from the wavenumber mapping techniques are in a good agreement with the results from conventional ultrasonic testing. All techniques delivered similar estimations of the in-plane size and depth of the biggest delamination present between aluminium plate and CFRP part. The main limitation of the wavenumber mapping approaches presented here is that it was not possible to quantify every delamination between CFRP plies caused by the impact as it is the case for conventional UT. Only some parts of the impact damage were visible in the wavenumber and thickness maps. Another limitation is that the relation between wavenumber and effective thickness is non-monotonous. This comes from

the complexity of the laminate lay-up used in the experiments and its anisotropy. In this work, a quadratic interpolation of the wavenumbers was used to eliminate this ambiguity.

Key messages The key messages of this section are as follows:

- Even though both wavenumber mapping approaches show similar performance in damage quantification, the local wavenumber mapping approach is less prone to artefacts related to the wave scattering from the damage.
- Both mapping approaches are limited in the characterisation of damage depth in the cross-ply laminates made of CFRP due to the strong anisotropy leading to the non-monotonous relation between the wavenumbers and effective thicknesses.

CHAPTER 5

Concluding remarks

Guided waves (GW) for damage detection in multi-layered plates were investigated both numerically and experimentally in this thesis with the focus on higher order modes. For the numerical modelling, a semi-analytical approach, the Scaled Boundary Finite Element Method, was used. In the experimental work, a laser-vibrometer-based sensing system and a laser-based excitation system were used for guided waves measurements, and ultrasonic immersion testing for the reference measurement of the impact-induced damage.

It was shown that the elastic properties of isotropic and anisotropic materials can be inferred from the GW modes since different modes are affected by a change in the properties in a unique way. The sensitivity study was performed to demonstrate this influence and to identify the modes sensitive to various elastic properties. One of the existing GW-based optimisation procedures was modified in terms of the experimental set-up and forward model and validated on isotropic materials first before its application to anisotropic materials. It was demonstrated that the optimisation algorithm converges to the actual material properties in the case of isotropic materials when the initial guess lays within ±20 %. Regarding the transversely isotropic materials, in two cases considered, the UD and the cross-ply laminate, both wave propagation directions, 0° and 90° should be used in the optimisation, however, due to different reasons. For the UD laminate, the reason is that dispersion curves differ, whereas for the cross-ply laminate, both directions have the same dispersion curves, but different modes are excited depending on the direction considered. Speaking of an advantage of the GW-based optimisation procedure over existing methods is that it does not require special sample preparation, thus, ageing of real structures can be analysed non-destructively. Further, the availability of accurate effective material properties allows to improve numerical models necessary, *e.g.*, for the model-assisted quality assessment of SHM systems.

Knowing the material properties, the characteristic dispersion curves were calculated to

perform further analysis and develop the concepts for the damage detection, localisation, and quantification for NDT and SHM of multi-layered structures. Two cases were addressed in this thesis, an adhesive bond made of isotropic materials and a composite over-wrapped pressure vessel made of isotropic metal and an anisotropic fibre-reinforced polymer. These are widely used in automotive and aerospace industries and are still challenging to inspect in a non-destructive manner.

In the first example, an interesting phenomenon, called mode repulsion, was investigated in detail. Mode repulsion was observed in some literature; however, it was neither extensively studied nor thought to be used for the characterisation of coupling between layers. Thus, the mode repulsion was investigated numerically and experimentally with respect to weak and strong adhesive bonds for the first time. The results show that the coupling strength between two layers influences the distance between coupled modes in a mode repulsion region in terms of frequency or phase velocity (wavenumber). Therefore, mode repulsion can be used for the characterisation of the adhesive bond's quality. To enable this, characteristic quantities related to mode repulsion have to be correlated with reference values from mechanical tests performed on weak and strong adhesive joints. To obtain the characteristic quantities, a local or a global approach can be used. For the local approach, one mode repulsion region especially sensitive to the coupling state of the adhesive bond needs to be chosen and the distance between the modes within this repulsion region has to be quantified. This distance either in terms of frequency or wavenumber will change with the coupling and thus the information about the quality of the adhesive bond can be gained from it. Furthermore, it was found that there are high frequency mode repulsion regions which are sensitive to either the longitudinal stiffness or transverse stiffness. Thus, by using the local approach one can investigate two characteristic regions each sensitive to either the longitudinal or transverse stiffnesses and potentially characterise tensile or shear strengths, respectively. Regarding the global approach, a certain frequency-wavenumber range which contains many mode repulsion regions needs to be chosen. The number of mode repulsion regions will change in the fixed range – more regions may appear, or some may disappear – depending on the coupling state. To quantify many mode repulsion regions simultaneously, a global indicator should be introduced. All in all, it was demonstrated that mode repulsion is a very interesting feature of GW in multi-layered structures, whose characteristics have a lot of potential for NDT of such structures.

At next, the analysis of the GW propagation was carried out for the hybrid structure as of a composite over-wrapped pressure vessel (COPV) with a load-sharing liner. The cylinder consisting of an aluminium liner and a carbon fibre-reinforced polymer (CFRP) over-wrap was approximated to a plate for this investigation. Dispersion curves and mode shapes were calculated for the aluminium-CFRP composite plate, based on which the appropriate modes

were identified, and their propagation and interaction with damage were studied. Two damage cases were considered – a crack in the metal layer and delamination between the CFRP plies. These damage cases are linked to two failure modes of COPV: the fatigue failure of the metallic liner and the failure of the composite over-wrap due to the impact damage. The GW analysis showed that most of the wave energy can be concentrated in a certain layer depending on the mode and frequency used, thus, allowing not only damage detection but also its localisation within the different layers. The energy steering is possible only if the modes beyond cut-off frequencies are used. In the case of the fundamental modes in the low frequency range, they interrogate the whole thickness of the aluminium-CFRP composite plate and thus are sensitive to damage located in both parts of the plate. Based on the results, a concept for an SHM system for COPV monitoring was proposed.

Further investigations were carried out experimentally on a similar hybrid composite plate with an impact-induced damage. The goal was to localise and quantify the damage in three dimensions using the wavenumber mapping. The technique allows estimating wavenumbers locally which can then be transformed into an effective thickness (ET) based on the dispersion relation. The resulting ET map provides a three-dimensional representation of the impact-induced damage in terms of the in-plane size and depth. Two well-known wavenumber mapping techniques were implemented in this thesis and their comparison on real impact damage was done for the first time. Both techniques delivered similar values of the in-plane size and depth of the biggest delamination present at the aluminium-CFRP interface. However, only an indication of the damage within CFRP plies could be observed using the wavenumber mapping approaches without a clear separation of every delamination between the plies as it was the case for high frequency ultrasonic testing in immersion. Another limitation comes from the non-monotonous relation between wavenumbers and their respective thicknesses. The relation is due to the strong anisotropy of the CFRP which was not the case for weak anisotropy found in glass fibre-reinforced laminates [140]. To eliminate this ambiguity, a quadratic interpolation of the wavenumber was used.

Outlook One of the areas for further investigations can be the improvement of the GW-based optimisation procedure by including a weighting factor based on the sensitivity information. Meaning that unique areas of modes which are most sensitive to a certain material parameter will get a weighting factor and thus will have a higher influence on the cost function. This may improve the reconstructed properties when amplitude of modes sensitive to a certain parameter is not so high as the amplitude of modes sensitive to other parameters.

Another definition of the sensitivity may be useful too which estimates not only the mode shift at one frequency but considers the relation of frequencies to each other and the characteristic shapes of the modes. Moreover, the GW-based optimisation procedure

can be extended to account for damping (viscoelastic) behaviour of the material. The benchmark of the procedure can be then performed based on the reference measurements in the ultrasonic frequency range, *i.e.*, using the procedures developed by Castaings *et al.* [66] and Martens *et al.* [197].

More effort can be put into the correlation of features of mode repulsion with weak and strong adhesive joints using the reference strength values from the mechanical testing.

Further, the experimental validation of energy steering in multi-layered plates is important. For this, the integration of IDTs between the layers may be necessary.

Bibliography

[1] Millar, S. *et al.* Chlorine determination in cement-bound materials with laser-induced breakdown spectroscopy (LIBS) – a review and validation. *Spectrochimica Acta Part B: Atomic Spectroscopy* **147**, 1–8 (2018). → p. 1

[2] Doroshtnasir, M., Worzewski, T., Krankenhagen, R. & Röllig, M. On-site inspection of potential defects in wind turbine rotor blades with thermography. *Wind Energy* **19**, 1407–1422 (2016). → p. 1

[3] Heckel, T., Thomas, H.-M. & Hanspach, G. Advantage of a combined ultrasonic and eddy current examination for railway inspection trains. In *Proceedings of ECNDT 2006 (Berlin, Germany)* (2006). → p. 1

[4] Papaelias, M. P., Roberts, C. & Davis, C. L. A review on non-destructive evaluation of rails: State-of-the-art and future development. *Proceedings of the Institution of Mechanical Engineers, Part F: Journal of Rail and Rapid Transit* **222**, 367–384 (2008). → p. 1

[5] Cawley, P. Structural health monitoring: Closing the gap between research and industrial deployment. *Structural Health Monitoring* **17**, 1225–1244 (2018). → p. 2

[6] Boller, C., Chang, F.-K. & Fujino, Y. (eds.) *Encyclopedia of Structural Health Monitoring* (John Wiley & Sons, Ltd, 2009). → p. 2, 13

[7] Balageas, D., Fritzen, C. & Güemes, A. (eds.) *Structural Health Monitoring* (John Wiley & Sons, Ltd, 2006). → p. 2

[8] Farrar, C. R. & Worden, K. An introduction to structural health monitoring. *Philosophical Transactions of the Royal Society A: Mathematical, Physical and Engineering Sciences* **365**, 303–315 (2007). → p. 2

[9] Farrar, C. R. & Worden, K. *Structural Health Monitoring* (John Wiley & Sons, Ltd, 2012). → p. 2

[10] Viktorov, I. A. *Rayleigh and Lamb waves* (Springer US, 1967). → p. 2

[11] Graff, K. F. *Wave motion in elastic solids* (Ohio State University Press, 1975). → p. 2

[12] Achenbach, J. D. *Wave Propagation in Elastic Solids* (North Holland: Elsevier, 1987). → p. 2

[13] Rose, J. L. *Ultrasonic Guided Waves in Solid Media* (Cambridge University Press, 2014). → p. 2, 5, 8, 9, 80

[14] Lowe, M., Alleyne, D. & Cawley, P. Defect detection in pipes using guided waves. *Ultrasonics* **36**, 147–154 (1998). Ultrasonics International 1997. → p. 2

[15] Chimenti, D. E. Guided waves in plates and their use in materials characterization. *Applied Mechanics Reviews* **50**, 247–284 (1997). → p. 2

[16] Mitra, M. & Gopalakrishnan, S. Guided wave based structural health monitoring: A review. *Smart Materials and Structures* **25**, 053001 (2016). → p. 2

[17] Guan, R., Lu, Y., Duan, W. & Wang, X. Guided waves for damage identification in pipeline structures: A review. *Structural Control and Health Monitoring* **24**, e2007 (2017). → p. 2

[18] Non-destructive testing. guided wave testing. general guidance and principles. Standard BS 9690-1:2011, British Standards Institution, London, United Kingdom (2011). → p. 2

[19] Non-destructive testing. guided wave testing. basic requirements for guided wave testing of pipes,

pipelines and structural tubulars. Standard BS 9690-2:2011, British Standards Institution, London, United Kingdom (2011). → p. 2

[20] Standard practice for guided wave testing of above ground steel piping with magnetostrictive transduction. Standard ASTME 2929-13, ASTM International, West Conshohocken, PA (2013). → p. 2

[21] Standard practice for guided wave testing of above ground steel pipework using piezoelectric effect transduction. Standard ASTME 2775-16, ASTM International, West Conshohocken, PA (2016). → p. 2

[22] Yang, W. & Kundu, T. Guided waves in multilayered plates for internal defect detection. *Journal of Engineering Mechanics* **124**, 311–318 (1998). → p. 3

[23] Kundu, T., Maslov, K., Karpur, P., Matikas, T. & Nicolaou, P. A Lamb wave scanning approach for the mapping of defects in [0/90] titanium matrix composites. *Ultrasonics* **34**, 43–49 (1996). → p. 3, 95, 97

[24] Castaings, M. & Hosten, B. Guided waves propagating in sandwich structures made of anisotropic, viscoelastic, composite materials. *The Journal of the Acoustical Society of America* **113**, 2622–2634 (2003). → p. 3

[25] Gao, H. *Ultrasonic guided wave mechanics for composite material structural health monitoring*. Dissertation, Pennsylvania State University (2007). → p. 3

[26] Yu, X., Fan, Z., Castaings, M. & Biateau, C. Feature guided wave inspection of bond line defects between a stiffener and a composite plate. *NDT & E International* **89**, 44–55 (2017). → p. 3

[27] Castaings, M. & Hosten, B. Ultrasonic guided waves for health monitoring of high-pressure composite tanks. *NDT & E International* **41**, 648–655 (2008). → p. 3, 19

[28] Sause, M. G., Hamstad, M. A. & Horn, S. Finite element modeling of Lamb wave propagation in anisotropic hybrid materials. *Composites Part B: Engineering* **53**, 249 – 257 (2013). → p. 3, 9

[29] Fromme, P., Reymondin, J.-P. & Masserey, B. High frequency guided waves for disbond detection in multi-layered structures. *Acta Acustica United With Acustica* **103**, 932–940 (2017). → p. 3

[30] Lugovtsova, Y. & Prager, J. Structural health monitoring of composite pressure vessels using guided ultrasonic waves. *Insight - Non-Destructive Testing and Condition Monitoring* **60**, 139–144 (2018). → p. 3, 9, 17

[31] Lugovtsova, Y., Bulling, J., Boller, C. & Prager, J. Analysis of guided wave propagation in a multi-layered structure in view of structural health monitoring. *Applied Sciences* **9**, 4600 (2019). → p. 3, 9, 35, 87, 94, 96, 97, 98

[32] Lamb, H. On waves in an elastic plate. *Proceedings of the Royal Society of London. Series A, Containing Papers of a Mathematical and Physical Character* **93**, 114–128 (1917). → p. 5

[33] Thomson, W. Transmission of elastic waves through a stratified solid medium. *Journal of applied Physics* **21**, 89–93 (1950). → p. 9

[34] Haskell, N. The dispersion of surface waves on multilayered media. *Bulletin of the seismological Society of America* **43**, 17–34 (1953). → p. 9

[35] Knopoff, L. A matrix method for elastic wave problems. *Bulletin of the Seismological Society of America* **54**, 431–438 (1964). → p. 9

[36] Kausel, E. Thin-layer method: Formulation in the time domain. *International journal for numerical methods in engineering* **37**, 927–941 (1994). → p. 9

[37] Adamou, A. & Craster, R. Spectral methods for modelling guided waves in elastic media. *The Journal of the Acoustical Society of America* **116**, 1524–1535 (2004). → p. 9

[38] Hayashi, T., Song, W. & Rose, J. Guided wave dispersion curves for a bar with an arbitrary cross-section, a rod and rail example. *Ultrasonics* **41**, 175–183 (2003). → p. 9

[39] Marzani, A., Viola, E., Bartoli, I., Di Scalea, F. & Rizzo, P. A semi-analytical finite element formulation for modeling stress wave propagation in axisymmetric damped waveguides. *Journal of Sound and*

Vibration **318**, 488–505 (2008). → p. 9

[40] Finnveden, S. & Fraggstedt, M. Waveguide finite elements for curved structures. *Journal of Sound and Vibration* **312**, 644–671 (2008). → p. 9

[41] Gravenkamp, H., Song, C. & Prager, J. A numerical approach for the computation of dispersion relations for plate structures using the scaled boundary finite element method. *Journal of Sound and Vibration* **331**, 2543–2557 (2012). → p. 9, 12, 25, 26, 27, 43

[42] Dong, S. B. & Nelson, R. B. On natural vibrations and waves in laminated orthotropic plates. *Journal of Applied Mechanics* **39**, 739–745 (1972). → p. 9

[43] Dong, S. B. & Huang, K. H. Edge vibrations in laminated composite plates. *Journal of Applied Mechanics* **52**, 433–438 (1985). → p. 9

[44] Nelson, R., Dong, S. & Kalra, R. Vibrations and waves in laminated orthotropic circular cylinders. *Journal of Sound and Vibration* **18**, 429–444 (1971). → p. 9

[45] Aalami, B. Waves in prismatic guides of arbitrary cross section. - (1973). → p. 9

[46] Xu, K., Ta, D., Su, Z. & Wang, W. Transmission analysis of ultrasonic Lamb mode conversion in a plate with partial-thickness notch. *Ultrasonics* **54**, 395–401 (2014). → p. 9

[47] Fellinger, P., Marklein, R., Langenberg, K. & Klaholz, S. Numerical modeling of elastic wave propagation and scattering with EFIT — elastodynamic finite integration technique. *Wave Motion* **21**, 47–66 (1995). → p. 9

[48] Schubert, F., Peiffer, A., Köhler, B. & Sanderson, T. The elastodynamic finite integration technique for waves in cylindrical geometries. *The Journal of the Acoustical Society of America* **104**, 2604–2614 (1998). → p. 9

[49] Leckey, C. A., Rogge, M. D., Miller, C. A. & Hinders, M. K. Multiple-mode lamb wave scattering simulations using 3D elastodynamic finite integration technique. *Ultrasonics* **52**, 193–207 (2012). → p. 9, 105, 106

[50] Luchinsky, D. G. *et al.* Modeling wave propagation and scattering from impact damage for structural health monitoring of composite sandwich plates. *Structural Health Monitoring* **12**, 296–308 (2013). → p. 9

[51] Willberg, C., Duczek, S., Vivar-Perez, J. M. & Ahmad, Z. A. B. Simulation methods for guided wave-based structural health monitoring: A review. *Applied Mechanics Reviews* **67** (2015). → p. 9

[52] Gravenkamp, H., Prager, J., Saputra, A. A. & Song, C. The simulation of Lamb waves in a cracked plate using the scaled boundary finite element method. *The Journal of the Acoustical Society of America* **132**, 1358–1367 (2012). → p. 12, 25

[53] Gravenkamp, H. Efficient simulation of elastic guided waves interacting with notches, adhesive joints, delaminations and inclined edges in plate structures. *Ultrasonics* **82**, 101–113 (2018). → p. 12, 25, 28, 29

[54] Lugovtsova, Y., Bulling, J., Prager, J. & Boller, C. Efficient modelling of guided ultrasonic waves using the scaled boundary FEM towards SHM of composite pressure vessels. In *Proceedings of the 9th European Workshop on Structural Health Monitoring* (2018). → p. 12

[55] Bochud, N., Laurent, J., Bruno, F., Royer, D. & Prada, C. Towards real-time assessment of anisotropic plate properties using elastic guided waves. *The Journal of the Acoustical Society of America* **143**, 1138–1147 (2018). → p. 12, 13

[56] Webersen, M., Johannesmann, S., Düchting, J., Claes, L. & Henning, B. Guided ultrasonic waves for determining effective orthotropic material parameters of continuous-fiber reinforced thermoplastic plates. *Ultrasonics* **84**, 53–62 (2018). → p. 12, 13, 21, 39, 40, 41, 69

[57] Karim, M. R., Mal, A. K. & Bar-Cohen, Y. Inversion of leaky Lamb wave data by simplex algorithm. *The Journal of the Acoustical Society of America* **88**, 482–491 (1990). → p. 12, 13

[58] Rogers, W. P. Elastic property measurement using Rayleigh-Lamb waves. *Research in Nondestructive Evaluation* **6**, 185–208 (1995). → p. 12, 13

[59] Hosten, B., Castaings, M., Tretout, H. & Voillaume, H. Identification of composite materials elastic moduli from Lamb wave velocities measured with single sided, contactless ultrasonic method. *AIP Conference Proceedings* **557**, 1023–1030 (2001). → p. 12, 13

[60] Bulling, J., Franosch, G., Lugovtsova, Y. & Prager, J. Sensitivity of ultrasonic guided waves to elastic constants: A numerical study. In Rizzo, P. & Milazzo, A. (eds.) *European Workshop on Structural Health Monitoring*, 759–768 (Springer International Publishing, Cham, 2021). → p. 12, 13, 21, 43

[61] Markham, M. Measurement of elastic constants by the ultrasonic pulse method. *British Journal of Applied Physics* **8**, S56–S63 (1957). → p. 12

[62] Markham, M. Measurement of the elastic constants of fibre composites by ultrasonics. *Composites* **1**, 145–149 (1969). → p. 12

[63] Hosten, B. Stiffness matrix invariants to validate the characterization of composite materials with ultrasonic methods. *Ultrasonics* **30**, 365–370 (1992). → p. 12

[64] Hosten, B., Deschamps, M. & Tittmann, B. R. Inhomogeneous wave generation and propagation in lossy anisotropic solids. application to the characterization of viscoelastic composite materials. *The Journal of the Acoustical Society of America* **82**, 1763–1770 (1987). → p. 12

[65] Baudouin, S. & Hosten, B. Immersion ultrasonic method to measure elastic constants and anisotropic attenuation in polymer-matrix and fiber-reinforced composite materials. *Ultrasonics* **34**, 379–382 (1996). Proceedings of Ultrasonics International 1995. → p. 12

[66] Castaings, M., Hosten, B. & Kundu, T. Inversion of ultrasonic, plane-wave transmission data in composite plates to infer viscoelastic material properties. *NDT & E International* **33**, 377–392 (2000). → p. 13, 120

[67] Claes, L., Meyer, T., Bause, F., Rautenberg, J. & Henning, B. Determination of the material properties of polymers using laser-generated broadband ultrasound. *Journal of Sensors and Sensor Systems* **5**, 187–196 (2016). → p. 13, 21, 39, 40, 69

[68] Gao, W., Glorieux, C. & Thoen, J. Laser ultrasonic study of Lamb waves: determination of the thickness and velocities of a thin plate. *International Journal of Engineering Science* **41**, 219–228 (2003). → p. 13

[69] Yeh, C.-H. & Yang, C.-H. Characterization of mechanical and geometrical properties of a tube with axial and circumferential guided waves. *Ultrasonics* **51**, 472–479 (2011). → p. 13

[70] Eremin, A., Glushkov, E., Glushkova, N. & Lammering, R. Evaluation of effective elastic properties of layered composite fiber-reinforced plastic plates by piezoelectrically induced guided waves and laser Doppler vibrometry. *Composite Structures* **125**, 449–458 (2015). → p. 13

[71] Thierry, V., Mesnil, O. & Chronopoulos, D. Experimental and numerical determination of the wave dispersion characteristics of complex 3D woven composites. *Ultrasonics* **103**, 106068 (2020). → p. 13

[72] Kudela, P., Radzienski, M., Fiborek, P. & Wandowski, T. Elastic constants identification of fibre-reinforced composites by using guided wave dispersion curves and genetic algorithm for improved simulations. *Composite Structures* **272**, 114178 (2021). → p. 13

[73] Marzani, A. & De Marchi, L. Characterization of the elastic moduli in composite plates via dispersive guided waves data and genetic algorithms. *Journal of Intelligent Material Systems and Structures* **24**, 2135–2147 (2013). → p. 13

[74] Webersen, M., Johannesmann, S., Claes, L. & Henning, B. Characterization of continuous-fiber reinforced thermoplastics using thermoacoustically excited ultrasonic Lamb waves. In *2016 IEEE IUS Proceedings* (2016). → p. 13, 39

[75] Johannesmann, S., Claes, L., Webersen, M. & Henning, B. Inverser Ansatz zur akustischen Charakterisierung plattenförmiger Materialproben. In *Deutsche Gesellschaft für Akustik e.V. 2017– Fortschritte der Akustik*, 999–1002 (2017). → p. 13, 21, 39, 40

[76] Johannesmann, S., Düchting, J., Webersen, M., Claes, L. & Henning, B. An acoustic waveguide-based approach to the complete characterisation of linear elastic, orthotropic material behaviour. *tm - Technisches Messen* **2018**, 478–486 (2018). → p. 13, 21, 40

[77] Rautela, M., Gopalakrishnan, S., Gopalakrishnan, K. & Deng, Y. Ultrasonic guided waves based identification of elastic properties using 1D-convolutional neural networks. In *2020 IEEE International Conference on Prognostics and Health Management (ICPHM)*, 1–7 (2020). → p. 13

[78] Gopalakrishnan, K., Rautela, M. & Deng, Y. Deep learning based identification of elastic properties using ultrasonic guided waves. In Rizzo, P. & Milazzo, A. (eds.) *European Workshop on Structural Health Monitoring*, 77–90 (Springer International Publishing, Cham, 2021). → p. 13

[79] Held, M. *et al.* Inverse determination of elastic material parameters from ultrasonic guided waves dispersion measurements using convolutional neuronal networks. In *Proceedings SMSI 2021*, vol. SMSI 2021 - Measurement Science, 239 – 240 (2021). → p. 13

[80] Bause, F. *et al.* Ultrasonic transmission measurements in the characterization of viscoelasticity utilizing polymeric waveguides. *Measurement Science and Technology* **27**, 105601 (2016). → p. 13, 56, 70

[81] Mallick, P. Joining for lightweight vehicles. In Mallick, P. (ed.) *Materials, Design and Manufacturing for Lightweight Vehicles*, chap. 8, 275–308 (Woodhead Publishing, 2010). → p. 14

[82] Ehrhart, B., Valeske, B. & Bockenheimer, C. Non-destructive evaluation (NDE) of aerospace composites: methods for testing adhesively bonded composites. In Karbhari, V. M. (ed.) *Non-Destructive Evaluation (NDE) of Polymer Matrix Composites*, chap. 8, 220–237 (Woodhead Publishing, 2013). → p. 14

[83] Standard test method for tensile properties of adhesive bonds. Standard ASTM D897-08(2016), ASTM International, West Conshohocken, PA (2016). → p. 14

[84] Pilarski, A. & Rose, J. L. A transverse-wave ultrasonic oblique-incidence technique for interfacial weakness detection in adhesive bonds. *Journal of Applied Physics* **63**, 300–307 (1988). → p. 14

[85] Baltazar, A., Wang, L., Xie, B. & Rokhlin, S. Inverse ultrasonic determination of imperfect interfaces and bulk properties of a layer between two solids. *The Journal of the Acoustical Society of America* **114**, 1424–1434 (2003). → p. 14

[86] Drinkwater, B. W., Castaings, M. & Hosten, B. The measurement of A0 and S0 Lamb wave attenuation to determine the normal and shear stiffnesses of a compressively loaded interface. *The Journal of the Acoustical Society of America* **113**, 3161–3170 (2003). → p. 14

[87] Hosten, B. & Castaings, M. Finite elements methods for modeling the guided waves propagation in structures with weak interfaces. *The Journal of the Acoustical Society of America* **117**, 1108–1113 (2005). → p. 14

[88] Mezil, S., Laurent, J., Royer, D. & Prada, C. Non contact probing of interfacial stiffnesses between two plates by zero-group velocity Lamb modes. *Applied Physics Letters* **105**, 021605 (2014). → p. 14

[89] Castaings, M. SH ultrasonic guided waves for the evaluation of interfacial adhesion. *Ultrasonics* **54**, 1760–1775 (2014). → p. 14, 15

[90] Rokhlin, S. I., Lavrentyev, A. I. & Li, B. Ultrasonic evaluation of environmental durability of adhesive joints. *Research in Nondestructive Evaluation* **5**, 95–109 (1993). → p. 14

[91] Budzik, M., Mascaro, B., Jumel, J., Castaings, M. & Shanahan, M. Monitoring of crosslinking of a dgeba-pamam adhesive in composite/aluminium bonded joint using mechanical and ultra-sound techniques. *International Journal of Adhesion and Adhesives* **35**, 120–128 (2012). → p. 14, 15

[92] Mezil, S. *et al.* Investigation of interfacial stiffnesses of a tri-layer using zero-group velocity Lamb modes. *The Journal of the Acoustical Society of America* **138**, 3202–3209 (2015). → p. 14

[93] Siryabe, E., Rénier, M., Meziane, A., Galy, J. & Castaings, M. Apparent anisotropy of adhesive bonds with weak adhesion and non-destructive evaluation of interfacial properties. *Ultrasonics* **79**, 34–51 (2017). → p. 14, 15, 77

[94] Hosten, B. & Castaings, M. Surface impedance matrices to model the propagation in multilayered media.

Ultrasonics **41**, 501—507 (2003). → p. 14

[95] Wang, W. & Rokhlin, S. Evaluation of interfacial properties in adhesive joints of aluminum alloys using angle-beam ultrasonic spectroscopy. *Journal of Adhesion Science and Technology* **5**, 647–666 (1991). → p. 14

[96] Lévesque, D. & Piché, L. A robust transfer matrix formulation for the ultrasonic response of multilayered absorbing media. *The Journal of the Acoustical Society of America* **92**, 452–467 (1992). → p. 14

[97] Lévesque, D., Legros, A., Michel, A. & Piché, L. High resolution ultrasonic interferometry for quantitative nondestructive characterization of interfacial adhesion in multilayer (metal/polymer/metal) composites. *Journal of Adhesion Science and Technology* **7**, 719–741 (1993). → p. 14

[98] Lavrentyev, A. I. & Rokhlin, S. I. Ultrasonic spectroscopy of imperfect contact interfaces between a layer and two solids. *The Journal of the Acoustical Society of America* **103**, 657–664 (1998). → p. 14

[99] Vlasie, V., de Barros, S., Rousseau, M. & Champaney, L. Ultrasonic rheological model of cohesive and adhesive zones in aluminum joints: validation by mechanical tests. *Archive of Applied Mechanics* **75**, 220–234 (2006). → p. 14, 15

[100] Ismaili, N. A. *et al.* Determination of epoxy film parameters in a three-layer metal/adhesive/metal structure. *IEEE Transactions on Ultrasonics, Ferroelectrics, and Frequency Control* **56**, 1955–1959 (2009). → p. 14, 15

[101] Guran, A. & Inman, D. J. *Wave Motion, Intelligent Structures and Nonlinear Mechanics* (WORLD SCIENTIFIC, 1995). → p. 15

[102] Meijer, P. H. E. & Bauer, E. *Group theory. The application to quantum mechanics* (North-Holland Publishing Company, 1962). → p. 16

[103] Deschamps, M., Hosten, B., Gérard, A. & Überall, H. Repulsion of phase-velocity dispersion curves and the nature of plate vibrations. *The Journal of the Acoustical Society of America* **96**, 908–917 (1994). → p. 16

[104] Maze, G., Léon, F., Ripoche, J. & Überall, H. Repulsion phenomena in the phase-velocity dispersion curves of circumferential waves on elastic cylindrical shells. *The Journal of the Acoustical Society of America* **105**, 1695–1701 (1999). → p. 16

[105] Simonetti, F. Lamb wave propagation in elastic plates coated with viscoelastic materials. *The Journal of the Acoustical Society of America* **115**, 2041–2053 (2004). → p. 16

[106] Zaitsev, B. D., Kuznetsova, I. E. & Joshi, S. G. Hybrid acoustic waves in thin potassium niobate plates. *Journal of Applied Physics* **90**, 3648–3649 (2001). → p. 16

[107] Kuznetsova, I. E., Zaitsev, B. D., Teplykh, A. A. & Borodina, I. A. Hybridization of acoustic waves in piezoelectric plates. *Acoustical Physics* **53**, 64–69 (2007). → p. 16

[108] Tucker, J. W. & Rampton, V. W. *Microwave ultrasonics in solid state physics* (North-Holland Publishing Company, 1972). → p. 17

[109] Legault, M. Pressure vessel tank types. URL https://www.compositesworld.com/articles/pressure-vessel-tank-types. Online; accessed 12-June-2020. → p. 17

[110] McLaughlan, P. B., Forth, S. C. & Grimes-Ledesma, L. R. Composite overwrapped pressure vessels, a primer. Tech. Rep., NASA Johnson Space Center; Houston, TX, United States (2011). → p. 17, 22

[111] Mair, G. W., Scherer, F. & Duffner, E. Concept of interactive determination of safe service life for composite cylinders by destructive tests parallel to operation. *International Journal of Pressure Vessels and Piping* **120-121**, 36–46 (2014). → p. 18

[112] Bunsell, A. R. Composite pressure vessels supply an answer to transport problems. *Reinforced Plastics* **50**, 38 – 41 (2006). → p. 18

[113] Fisher, M. E. *Burst Pressure Prediction of Filament Wound Composite Pressure Vessels Using Acoustic Emission*. Ph.D. thesis, Embry-Riddle Aeronautical University - Daytona Beach (1996). → p. 18

[114] Chou, H., Mouritz, A., Bannister, M. & Bunsell, A. Acoustic emission analysis of composite pressure vessels under constant and cyclic pressure. *Composites Part A: Applied Science and Manufacturing* **70**, 111–120 (2015). → p. 18

[115] Foedinger, R. C. *et al.* Embedded fiber optic sensor arrays for structural health monitoring of filament wound composite pressure vessels. In *Smart Structures and Materials 1999: Sensory Phenomena and Measurement Instrumentation for Smart Structures and Materials*, vol. 3670, 289 – 301. International Society for Optics and Photonics (SPIE, 1999). → p. 18, 19

[116] Degrieck, J., Waele, W. D. & Verleysen, P. Monitoring of fibre reinforced composites with embedded optical fibre Bragg sensors, with application to filament wound pressure vessels. *NDT & E International* **34**, 289–296 (2001). → p. 18, 19

[117] Kang, D., Kim, C. & Kim, C. The embedment of fiber bragg grating sensors into filament wound pressure tanks considering multiplexing. *NDT & E International* **39**, 109–116 (2006). → p. 18, 19

[118] Gąsior, P. *et al.* Application of complementary optical methods for strain investigation in composite high pressure vessel. *Composite Structures* **203**, 718–724 (2018). → p. 18, 19

[119] Saeter, E., Lasn, K., Nony, F. & Echtermeyer, A. T. Embedded optical fibres for monitoring pressurization and impact of filament wound cylinders. *Composite Structures* **210**, 608–617 (2019). → p. 18, 19

[120] Duncan, R. G. *et al.* OFDR-based distributed sensing and fault detection for single-and multi-mode avionics fiber-optics (2009). → p. 19

[121] Maurin, L., Ferdinand, P., Nony, F. & Villalonga, S. OFDR distributed strain measurements for SHM of hydrostatic stressed structures : an application to high pressure H2 storage type iv composite vessels – H2E project. In *Proceedings of the 7th European Workshop on Structural Health Monitoring*, 930–937 (2014). → p. 19

[122] Xiao, B. *et al.* In-situ monitoring of a filament wound pressure vessel by the MWCNT sensor under hydraulic fatigue cycling and pressurization. *Sensors* **19** (2019). → p. 19

[123] Bulletti, A., Giannelli, P., Calzolai, M. & Capineri, L. An integrated acousto/ultrasonic structural health monitoring system for composite pressure vessels. *IEEE Transactions on Ultrasonics, Ferroelectrics, and Frequency Control* **63**, 864–873 (2016). → p. 19

[124] Yaacoubi, S., McKeon, P., Ke, W., Declercq, N. & Dahmene, F. Towards an ultrasonic guided wave procedure for health monitoring of composite vessels: Application to hydrogen-powered aircraft. *Materials* **10** (2017). → p. 19, 20

[125] Yang, B. *et al.* Damage localization in hydrogen storage vessel by guided waves based on a real-time monitoring system. *International Journal of Hydrogen Energy* (2019). → p. 19

[126] Guo, N. & Cawley, P. The interaction of Lamb waves with delaminations in composite laminates. *The Journal of the Acoustical Society of America* **94**, 2240–2246 (1993). → p. 20, 91

[127] Glushkov, E., Glushkova, N., Golub, M. V., Moll, J. & Fritzen, C.-P. Wave energy trapping and localization in a plate with a delamination. *Smart Materials and Structures* **21**, 125001 (2012). → p. 20

[128] Żak, A., Radzieński, M., Krawczuk, M. & Ostachowicz, W. Damage detection strategies based on propagation of guided elastic waves. *Smart Materials and Structures* **21**, 035024 (2012). → p. 20

[129] Yu, L. & Leckey, C. A. Lamb wave–based quantitative crack detection using a focusing array algorithm. *Journal of Intelligent Material Systems and Structures* **24**, 1138–1152 (2013). → p. 20

[130] Ren, B. & Lissenden, C. J. Ultrasonic guided wave inspection of adhesive bonds between composite laminates. *International Journal of Adhesion and Adhesives* **45**, 59 – 68 (2013). → p. 20

[131] He, S. & Ng, C.-T. Guided wave-based identification of multiple cracks in beams using a Bayesian approach. *Mechanical Systems and Signal Processing* **84**, 324 – 345 (2017). → p. 20

[132] Ruzzene, M. Frequency–wavenumber domain filtering for improved damage visualization. *Smart Materials and Structures* **16**, 2116–2129 (2007). → p. 20, 44, 45

[133] Sohn, H. *et al.* Delamination detection in composites through guided wave field image processing. *Composites Science and Technology* **71**, 1250 – 1256 (2011). → p. 20

[134] Sohn, H. *et al.* Automated detection of delamination and disbond from wavefield images obtained using a scanning laser vibrometer. *Smart Materials and Structures* **20**, 045017 (2011). → p. 20

[135] Michaels, T. E., Michaels, J. E. & Ruzzene, M. Frequency–wavenumber domain analysis of guided wavefields. *Ultrasonics* **51**, 452 – 466 (2011). → p. 20

[136] Yu, L., Leckey, C. A. C. & Tian, Z. Study on crack scattering in aluminum plates with Lamb wave frequency–wavenumber analysis. *Smart Materials and Structures* **22**, 065019 (2013). → p. 20

[137] Flynn, E. B., Chong, S. Y., Jarmer, G. J. & Lee, J.-R. Structural imaging through local wavenumber estimation of guided waves. *NDT & E International* **59**, 1 – 10 (2013). → p. 20, 23, 45

[138] Rogge, M. D. & Leckey, C. A. Characterization of impact damage in composite laminates using guided wavefield imaging and local wavenumber domain analysis. *Ultrasonics* **53**, 1217–1226 (2013). → p. 20, 21, 23, 45, 47, 105, 106

[139] Tian, Z., Yu, L. & Leckey, C. Delamination detection and quantification on laminated composite structures with Lamb waves and wavenumber analysis. *Journal of Intelligent Material Systems and Structures* **26**, 1723–1738 (2015). → p. 20, 23

[140] Mesnil, O., Leckey, C. A. & Ruzzene, M. Instantaneous and local wavenumber estimations for damage quantification in composites. *Structural Health Monitoring* **14**, 193–204 (2015). → p. 20, 23, 45, 46, 47, 106, 119

[141] Juarez, P. D. & Leckey, C. A. Multi-frequency local wavenumber analysis and ply correlation of delamination damage. *Ultrasonics* **62**, 56 – 65 (2015). → p. 20, 21, 23, 47, 105, 106

[142] Lugovtsova, Y., Johannesmann, S., Henning, B. & Prager, J. Analysis of lamb wave mode repulsion and its implications to the characterisation of adhesive bonding strength. *Proceedings of Meetings on Acoustics* **38**, 030005 (2019). → p. 22, 77, 78, 83, 84

[143] Lugovtsova, Y., Mesnil, O., Bulling, J., Prager, J. & Boller, C. Damage quantification in aluminium-CFRP composite structures using guided wave wavenumber mapping. In *AeroNDT 2019 Conference Proceedings*, 050018 (2020). 11th International Symposium on NDT in Aerospace, Nov 2019, Paris-Saclay, France. → p. 23

[144] Song, C. & Wolf, J. P. The scaled boundary finite-element method—alias consistent infinitesimal finite-element cell method—for elastodynamics. *Computer Methods in Applied Mechanics and Engineering* **147**, 329–355 (1997). → p. 25

[145] Song, C. A matrix function solution for the scaled boundary finite-element equation in statics. *Computer Methods in Applied Mechanics and Engineering* **193**, 2325–2356 (2004). → p. 25

[146] Man, H., Song, C., Gao, W. & Tin-Loi, F. A unified 3D-based technique for plate bending analysis using scaled boundary finite element method. *International Journal for Numerical Methods in Engineering* **91**, 491–515 (2012). → p. 25

[147] Song, C. Dynamic analysis of unbounded domains by a reduced set of base functions. *Computer Methods in Applied Mechanics and Engineering* **195**, 4075 – 4094 (2006). → p. 25

[148] Song, C. & Bazyar, M. H. Development of a fundamental-solution-less boundary element method for exterior wave problems. *Communications in Numerical Methods in Engineering* **24**, 257–279 (2008). → p. 25

[149] Song, C. The scaled boundary finite element method in structural dynamics. *International Journal for Numerical Methods in Engineering* **77**, 1139–1171 (2009). → p. 25

[150] Gravenkamp, H., Man, H., Song, C. & Prager, J. The computation of dispersion relations for three-dimensional elastic waveguides using the scaled boundary finite element method. *Journal of Sound and Vibration* **332**, 3756–3771 (2013). → p. 25, 28, 43

[151] Gravenkamp, H., Birk, C. & Song, C. The computation of dispersion relations for axisymmetric

waveguides using the scaled boundary finite element method. *Ultrasonics* **54**, 1373 – 1385 (2014). → p. 25

[152] Gravenkamp, H., Bause, F. & Song, C. On the computation of dispersion curves for axisymmetric elastic waveguides using the scaled boundary finite element method. *Computers & Structures* **131**, 46 – 55 (2014). → p. 25

[153] Gravenkamp, H., Birk, C. & Song, C. Computation of dispersion curves for embedded waveguides using a dashpot boundary condition. *The Journal of the Acoustical Society of America* **135**, 1127–1138 (2014). → p. 25

[154] Gravenkamp, H., Bause, F. & Song, C. On the computation of dispersion curves for axisymmetric elastic waveguides using the scaled boundary finite element method. *Computers & Structures* **131**, 46–55 (2014). → p. 25

[155] Gravenkamp, H., Birk, C. & Song, C. Simulation of elastic guided waves interacting with defects in arbitrarily long structures using the scaled boundary finite element method. *Journal of Computational Physics* **295**, 438–455 (2015). → p. 25

[156] Song, C. & Vrcelj, Z. Evaluation of dynamic stress intensity factors and T-stress using the scaled boundary finite-element method. *Engineering Fracture Mechanics* **75**, 1960 – 1980 (2008). → p. 25

[157] Song, C., Tin-Loi, F. & Gao, W. A definition and evaluation procedure of generalized stress intensity factors at cracks and multi-material wedges. *Engineering Fracture Mechanics* **77**, 2316 – 2336 (2010). → p. 25

[158] Song, C., Tin-Loi, F. & Gao, W. Transient dynamic analysis of interface cracks in anisotropic bimaterials by the scaled boundary finite-element method. *International Journal of Solids and Structures* **47**, 978 – 989 (2010). → p. 25

[159] Ooi, E. T., Song, C., Tin-Loi, F. & Yang, Z. Polygon scaled boundary finite elements for crack propagation modelling. *International Journal for Numerical Methods in Engineering* **91**, 319–342 (2012). → p. 25

[160] Bause, F., Gravenkamp, H., Rautenberg, J. & Henning, B. Transient modeling of ultrasonic guided waves in circular viscoelastic waveguides for inverse material characterization. *Measurement Science and Technology* **26**, 095602 (2015). → p. 25

[161] Bulling, J., Jurgelucks, B., Prager, J. & Walther, A. Defect reconstruction in a 2d semi-analytical waveguide model via derivative-based optimization. Tech. Rep., ArXiv (2021). http://arxiv.org/abs/2108.00770. → p. 25

[162] Rokhlin, S., Chimenti, D. & Nagy, P. *Physical Ultrasonics of Composites* (Oxford University Press, Oxford, 2011). → p. 30, 31

[163] Mesnil, O., Imperiale, A., Demaldent, E. & Chapuis, B. Validation of spectral finite element simulation tools dedicated to guided wave based structure health monitoring. *AIP Conference Proceedings* **2102**, 050018 (2019). → p. 33

[164] Imperiale, A., Leymarie, N. & Demaldent, E. Numerical modeling of wave propagation in anisotropic viscoelastic laminated materials in transient regime: Application to modeling ultrasonic testing of composite structures. *International Journal for Numerical Methods in Engineering* **n/a** (2020). → p. 33

[165] Mesnil, O. *et al.* Experimental Validation of Transient Spectral Finite Element Simulation Tools Dedicated to Guided Wave-Based Structural Health Monitoring. *Journal of Nondestructive Evaluation, Diagnostics and Prognostics of Engineering Systems* **4** (2021). 041003. → p. 33

[166] Lugovtsova, Y. *et al.* Damage quantification in an aluminium-CFRP composite structure using guided wave wavenumber mapping: Comparison of instantaneous and local wavenumber analyses. *NDT & E International* **122**, 102472 (2021). → p. 34, 37, 38, 46, 47, 99, 100, 101, 102, 104, 105, 107, 109, 110, 111, 112, 113

[167] Wilcox, P. D. *Lamb wave inspection of large structures using permanently attached transducers*. Dissertation, Imperial College London (1998). → p. 34

[168] AlfaLam software of Darmstadt Technical University. https://www.klub.tu-darmstadt.de/forschung_klub/downloads_3/downloads_klub.de.jsp. Online; accessed 12-February-2018. → p. 36

[169] Bell, A. G. Upon the production and reproduction of sound by light. *Journal of the Society of Telegraph Engineers* **9**, 404–426 (1880). → p. 39

[170] Alleyne, D. & Cawley, P. A two-dimensional fourier transform method for the measurement of propagating multimode signals. *The Journal of the Acoustical Society of America* **89**, 1159–1168 (1991). → p. 39, 41, 44

[171] Maraschini, M., Ernst, F., Foti, S. & Socco, L. V. A new misfit function for multimodal inversion of surface waves. *GEOPHYSICS* **75**, G31–G43 (2010). → p. 41

[172] Yan, L. *et al.* Elastic properties inversion of an isotropic plate by hybrid particle swarm-based-simulated annealing optimization technique from leaky Lamb wave measurements using acoustic microscopy. *Journal of Nondestructive Evaluation* **33**, 651–662 (2014). → p. 41

[173] Claes, L., Bause, F., Rautenberg, J. & Henning, B. Detection of ultrasonic plate waves using ceramic strip transducers. In *Proceedings SENSOR*, vol. P3, 775–779 (2015). → p. 41

[174] Lagarias, J., Reeds, J., Wright, M. & Wright, P. Convergence properties of the Nelder–Mead simplex method in low dimensions. *SIAM Journal on Optimization* **9**, 112–147 (1998). → p. 42

[175] Krome, F. & Gravenkamp, H. Analyzing modal behavior of guided waves using high order eigenvalue derivatives. *Ultrasonics* **71**, 75–85 (2016). → p. 43

[176] Radzieński, M., Doliński, Ł., Krawczuk, M., Żak, A. & Ostachowicz, W. Application of RMS for damage detection by guided elastic waves. *Journal of Physics: Conference Series* **305**, 012085 (2011). → p. 44

[177] Segers, J., Hedayatrasa, S., Poelman, G., Van Paepegem, W. & Kersemans, M. Robust and baseline-free full-field defect detection in complex composite parts through weighted broadband energy mapping of mode-removed guided waves. *Mechanical Systems and Signal Processing* **151**, 107360 (2021). → p. 44

[178] Kudela, P., Radzienski, M. & Ostachowicz, W. Impact induced damage assessment by means of Lamb wave image processing. *Mechanical Systems and Signal Processing* **102**, 23–36 (2018). → p. 44

[179] Mesnil, O., Yan, H., Ruzzene, M., Paynabar, K. & Shi, J. Fast wavenumber measurement for accurate and automatic location and quantification of defect in composite. *Structural Health Monitoring* **15**, 223–234 (2016). → p. 46, 101

[180] Mesnil, O. *Sparse reconstruction and analysis of guided wavefields for damage detection and quantification*. Dissertation, Georgia Institute of Technology (2016). → p. 46

[181] Richter, F. Die physikalischen Eigenschaften der Stähle – Das 100-Stähle-Programm, Teil I: Tafeln und Bilder. http://portal.tugraz.at/portal/page/portal/Files/i5110/files/Forschung/Thermophysik/Staehle-Richter.pdf. Online; accessed 01-February-2021. → p. 56

[182] Tschöke, K. *et al.* Feasibility of model-assisted probability of detection principles for structural health monitoring systems based on guided waves for fibre-reinforced composites. *IEEE Transactions on Ultrasonics, Ferroelectrics, and Frequency Control* 1–1 (2021). → p. 70

[183] Gianneo, A., Carboni, M. & Giglio, M. Feasibility study of a multi-parameter probability of detection formulation for a Lamb waves–based structural health monitoring approach to light alloy aeronautical plates. *Structural Health Monitoring* **16**, 225–249 (2017). → p. 70

[184] Kern. https://www.kern.de/de/technisches-datenblatt/polycarbonat-pc?n=2301_1. Online; accessed 18-August-2021. → p. 81

[185] Rumble, J. *CRC HANDBOOK OF CHEMISTRY AND PHYSICS* (CRC Press, BOCA RATON, 2018), 99th ed. edn. → p. 81

[186] Jardret, V. & Morel, P. Viscoelastic effects on the scratch resistance of polymers: relationship between mechanical properties and scratch properties at various temperatures. *Progress in Organic Coatings* **48**,

322–331 (2003). → p. 82

[187] Ostiguy, P.-C., Duff, A. L., Quaegebeur, N., Brault, L.-P. & Masson, P. In situ characterization technique to increase robustness of imaging approaches in structural health monitoring using guided waves. *Structural Health Monitoring* **13**, 525–536 (2014). → p. 82

[188] Monkhouse, R., Wilcox, P. & Cawley, P. Flexible interdigital PVDF transducers for the generation of Lamb waves in structures. *Ultrasonics* **35**, 489–498 (1997). → p. 98

[189] Ueberschlag, P. PVDF piezoelectric polymer. *Sensor Review* **21**, 118–126 (2001). → p. 98

[190] Seminara, L. *et al.* Piezoelectric polymer transducer arrays for flexible tactile sensors. *IEEE Sensors Journal* **13**, 4022–4029 (2013). → p. 98

[191] Bulletti, A. & Capineri, L. Interdigital piezopolymer transducers for time of flight measurements with ultrasonic Lamb waves on carbon-epoxy composites under pure bending stress. *Journal of Sensors* (2015). → p. 98

[192] Ren, B. & Lissenden, C. J. PVDF multielement Lamb wave sensor for structural health monitoring. *IEEE Transactions on Ultrasonics, Ferroelectrics, and Frequency Control* **63**, 178–185 (2016). → p. 98

[193] Giannelli, P., Bulletti, A. & Capineri, L. Charge-mode interfacing of piezoelectric interdigital Lamb wave transducers. *Electronics Letters* **52**, 894–896 (2016). → p. 98

[194] Lugovtsova, Y., Bulletti, A., Giannelli, P., Capineri, L. & Prager, J. Characterization of a flexible piezopolymer-based interdigital transducer for selective excitation of ultrasonic guided waves. In *2020 IEEE International Ultrasonics Symposium (IUS)*, 1–4 (2020). → p. 98

[195] Bouvet, C., Castanié, B., Bizeul, M. & Barrau, J.-J. Low velocity impact modelling in laminate composite panels with discrete interface elements. *International Journal of Solids and Structures* **46**, 2809 – 2821 (2009). → p. 103

[196] Moll, J. *et al.* Guided waves for damage detection in complex composite structures: The influence of omega stringer and different reference damage size. *Applied Sciences* **10** (2020). → p. 103

[197] Martens, Arvid and Daemen, Jannes and Kersemans, Mathias and Delrue, Steven and Verboven, Erik and Van Paepegem, Wim and Van Den Abeele, Koen. Characterization of the full viscoelastic tensor of anisotropic multilayered material plates by means of the Ultrasonic Polar Scan. In *International Congress on Ultrasonics* (2019). → p. 120